MICROCOPY RESOLUTION TEST CHART

NATIONAL BUREAU OF STANDARDS-1963-A

POSITIVE

REPORT DOCUMENTATION PAGE	READ INSTRUCTIONS BEFORE COMPLETING FORM

1. REPORT NUMBER	2. GOVT ACCESSION NO.	3. RECIPIENT'S CATALOG NUMBER
TR-RH-83-4	AD.A136515	

4. TITLE (and Subtitle)	5. TYPE OF REPORT & PERIOD COVERED
TRANSVERSE MODE FORMATION IN POSITIVE BRANCH UNSTABLE RESONATORS	Technical Report
	6. PERFORMING ORG. REPORT NUMBER

7. AUTHOR(s)	8. CONTRACT OR GRANT NUMBER(s)
R. William Jones	

9. PERFORMING ORGANIZATION NAME AND ADDRESS	10. PROGRAM ELEMENT, PROJECT, TASK AREA & WORK UNIT NUMBERS
Commander, US Army Missile Command ATTN: DRSMI-RH Redstone Arsenal, AL 35898	

11. CONTROLLING OFFICE NAME AND ADDRESS	12. REPORT DATE
Commander, US Army Missile Command ATTN: DRSMI-RPT Redstone Arsenal, AL 35898	Aug 83
	13. NUMBER OF PAGES

14. MONITORING AGENCY NAME & ADDRESS(if different from Controlling Office)	15. SECURITY CLASS. (of this report)
	UNCLASSIFIED
	15a. DECLASSIFICATION/DOWNGRADING SCHEDULE

16. DISTRIBUTION STATEMENT (of this Report)

Approved for public release; distribution unlimited.

17. DISTRIBUTION STATEMENT (of the abstract entered in Block 20, if different from Report)

18. SUPPLEMENTARY NOTES

19. KEY WORDS (Continue on reverse side if necessary and identify by block number)

lasers, unstable resonators, wave optics codes, resonator codes, optics, transverse mode formation, laser resonators, CO_2 lasers

20. ABSTRACT (Continue on reverse side if necessary and identify by block number)

The dynamics of transverse mode formation in positive branch unstable resonators with moderate magnification ($1.32 < M < 2.7$) and typical Fresnel numbers ($279 < N_T < 10,800$) used in high energy lasers has been investigated. The objective was to observe the far-field intensity distribution from the onset of pumping to the steady-state diffraction limited pattern.

The research consisted of experimental and numerical analyses. The experimental measurements of mode formation time were performed using a pulsed CO_2

DD FORM 1473 EDITION OF 1 NOV 65 IS OBSOLETE

20. (Continued)

laser and a pulsed XeF laser. Mode formation was deduced from observation of the far-field. The analytical effort consisted of a fast Fourier transform (FFT) wave optics computation which modeled the far-field pattern evolution.

Results agree with the temporal mode formation geometrical theory of Anan'ev when laser saturation is achieved at the predicted mode formation time in a CO_2 laser. Rapid saturation at one-third this time results in significantly earlier mode formation compared to the geometrical theory for a XeF laser.

CONTENTS

1

I. INTRODUCTION AND HISTORICAL DEVELOPMENT

A. Background of Laser Transverse Mode Formation

The evolution of an ideal laser beam from the onset of spontaneous emission to the production of steady state transverse resonator modes characteristic of a diffraction limited output depends upon resonator geometry and possibly upon saturable gain. This phenomenon is a particular interest in the discussion of short pulse high gain lasers. In these lasers a sizeable amount of energy is often lost during formation of the lowest order transverse mode, leading to poor far-field focusing.

Historically, this problem devolves from two kinds of laser resonators, the stable and the unstable. The first kind of resonator to be used, the conditionally stable resonator, was developed as an extension of the Fabry-Perot, or planar mirror resonator. Later, the concave-planar configuration, now in widespread use, was developed. Many lasers at that time had features which conformed to the following parameters: continuous wave (CW) operation, relatively small beam diameter (millimeters), and low power (tens of milli-watts) applications. The difficulty in the use of stable resonators with large apertures and high power will become apparent in the discussions in later sections of this report.

The second type of resonator has become extremely useful as seen for the lasers of interest in this text. This is called the unstable resonator and was originally proposed by Siegman [1]. These resonators offer many advantages for large aperture, high power CW and pulsed applications.

The development of pulsed lasers leads one to use the positive branch unstable confocal resonator. Mode formation time is not of interest in the CW laser case, since the transverse modes will sort themselves out in a short time compared to the time of laser operation. However, with the pulsed laser, which generates power over a relatively short interval (0.01 to 50 x 10^{-6} seconds), the situation is different. In this case it became apparent that the far-field "focused" energy pattern frequently does not represent the quasi-steady-state distribution as calculated from the transverse modes of the CW case.

The pioneer paper of Zemskov, et al. [2], describes the experimental result of using conditionally stable (plane parallel) versus unstable resonators in a short pulse copper vapor laser. In this and subsequent papers [3,4] it was determined that, aside from other difficulties, the stable resonator takes an unacceptably large number of resonator round trips for the radiation to sort itself out into the transverse modes characteristic of a diffraction limited laser. A further result was that to obtain minimum beam divergence it is necessary to use an unstable "telescopic" resonator with convergence properties based upon the Fresnel number and magnification of the resonator. From using geometric analysis of the resonator it was discovered and experimentally verified that a very large magnification (M ~ 250) is required to insure near diffraction limited performance of a laser with a pulse length in tens of nanoseconds.

The modeling of the unstable resonator, described by Zemskov as well as a subsequent refinement by Anan'ev [5], uses this geometric approach to

3

analyze transverse mode formation. In the Anan'ev work, the angular extent
of the radiation from the spontaneous source field is decreased to a diffrac-
tion limited output by successive passes between convex and concave resonator
mirrors--a transient angular "pinching down" of laser light to produce a
collimated beam. The equation he derives for the number of round trips re-
quired to produce a quasi-stable transverse mode in a confocal unstable
resonator is given by

$$n = \frac{\ln\left(\frac{a^2}{\lambda f_1}\right)}{\ln(M)} \qquad (1.1)$$

where a is the length of the side of a square active medium; λ, the laser
wavelength; $-f_1$, the secondary mirror focal length; and M, the resonator
magnification. The mode formation time is then given as

$$\tau = \frac{2nL}{c} = \frac{2L}{c} \frac{\ln\left(\frac{a^2}{\lambda f_1}\right)}{\ln M} \qquad (1.2)$$

where L is the resonator mirror separation, and a, the speed of light.
This basic formula, with minor modifications and adaptations to other
resonators, has been the cornerstone of transverse mode formation time theory
in unstable confocal resonators and defines the minimum number of round trips
to produce steady-state mode operation.

This geometrical modeling may be simply illustrated in Figure 1. A
typical positive branch unstable resonator is shown with a concave primary
mirror, m_2, of half dimension a/2, and a convex secondary, or
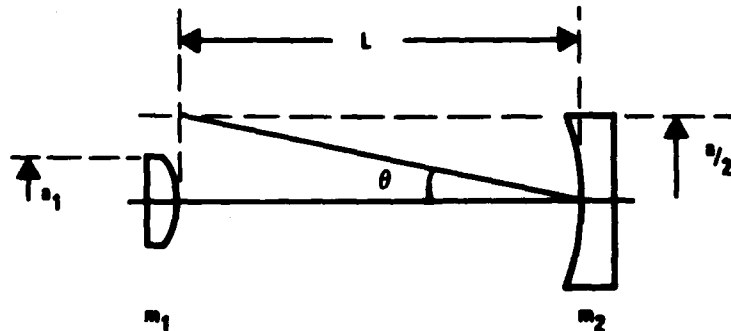

Figure 1. Geometry of transverse mode formation.

feedback mirror, m_1, of half dimension a_1. The separation of the two mirrors
is L. This analogy is valid in the regime of moderate magnification (1.32 <
M < 3) and large ratios of mirror separation to beam diameter. After each
round trip the angular distribution of the radiation is decreased by the
resonator magnification, i.e.,

4

$$\theta_0 = \frac{(a/2)}{L} \ , \ L \gg \frac{a}{2} \tag{1.3}$$

$$\theta_1 = \frac{(a/2)}{M \ L} \tag{1.4}$$

$$\theta_2 = \frac{(a/2)}{M^2 \ L} \tag{1.5}$$

$$\theta_3 = \frac{(a/2)}{M^3 \ L} \tag{1.6}$$

$$\theta_{n'} = \frac{(a/2)}{M^{n'} \ L} \tag{1.7}$$

where the resonator magnification is given by

$$M = \frac{f_2}{f_1} = \frac{R_2}{R_1} \tag{1.8}$$

with f_2, $- f_1$ being the respective primary and secondary mirror focal lengths, and

$$R_n = 2f_n \quad . \tag{1.9}$$

A criterion for the minimum far-field spot size occurs when $\theta_{n'}$ becomes equal to a diffraction angle, i.e.,

$$\theta_{n'} = \frac{\lambda}{(a/2)} \tag{1.10}$$

where λ is the laser wavelength. This, combined with equation (1.7), gives the approximate number of round trips n', required for the unstable resonator to reach the diffraction limit, i.e.,

$$\frac{\lambda}{(a/2)} = \frac{(a/2)}{M^{n'} \ L} \tag{1.11}$$

or,

$$M^{n'} = \frac{(a/2)^2}{\lambda \ L} \tag{1.12}$$

$$n' = \left[\frac{\ln \frac{(a/2)^2}{L}}{\ln M} \right] \tag{1.13}$$

which gives the same approximate number of round trips necessary for convergence as compared to the Anan'ev formula.

B. Stead-State Transverse Modes in Resonators

1. Stable Resonators

The first lasers proposed were constructed with stable resonator cavities [6,7,8,9] and as a result, the theory of stable resonator modes has been well established. An excellent example of this development is given in the case of the symmetric confocal resonator [10,11]. The empty cavity transverse modes for this resonator may be obtained in closed form as

$$U_{m\ell}(x,y) = H_m \left[\left(\frac{2\pi}{L\lambda}\right)^{\frac{1}{2}} x \right] H_\ell \left[\left(\frac{2\pi}{L\lambda}\right)^{\frac{1}{2}} y \right] \exp \left[- \left(\frac{\pi}{L\lambda}\right) (x^2 + y^2) \right] \tag{1.14}$$

where $U_{m\ell}(x,y)$ is the amplitude eigenfunction solution of the transverse electromagnetic (TEM) modes of the resonator; H_m and H_ℓ are Hermite polynomials of order m and ℓ; L and λ have been defined previously. All modes are power orthogonal and may be expressed as Hermite-Gauss functions for resonators with rectangular symmetry. Figure 2 is a schematic of the symmetric confocal resonator with a few of the lower order modes illustrated in Figure 3.

Stable resonators are suitable for lower power applications; inherent difficulties exist in their high power (high energy) use. Ideally, we desire to have all the energy contained within the lowest loss transverse mode, with the mode filling the cavity active media. This would insure beam propagation to the far field with maximum fluence and minimum angular divergence and far field spot size. Stable resonators do not have these characteristics. In high power practical applications the lowest-order (usually Gaussian) mode is small compared to the transverse active media dimensions, with most of the energy partitioned into higher order modes with increasingly larger divergence. As an example [12] the lowest-order mode of the symmetric confocal resonator has a spot size 2W given by

$$2W = 2F (g_1, g_2)\left(\frac{L\lambda}{\pi}\right)^{\frac{1}{2}} \tag{1.15}$$

with $2W_o \equiv 2 \frac{L\lambda}{\pi}^{\frac{1}{2}}$. $F(g_1, g_2)$ is a number which depends upon resonator parameters and is on the order of unity or slightly larger for stable resonators. For a typical high energy CO_2 laser, L = 200 cm and the lowest order mode diameter, $2W_o$, is 0.52 cm. This may be compared to a desired beam of 10 cm size. One could consider using stable resonator mirrors having large radii of curvature to fill the mode volume of a typical high energy laser resonator. However, mechanical stability of the resonator alignment becomes a limiting practical problem. The mirror stability for nearly flat mirrors in the resonator has been shown by Siegman [12] to be
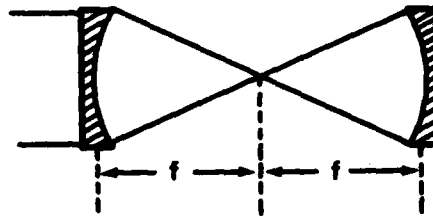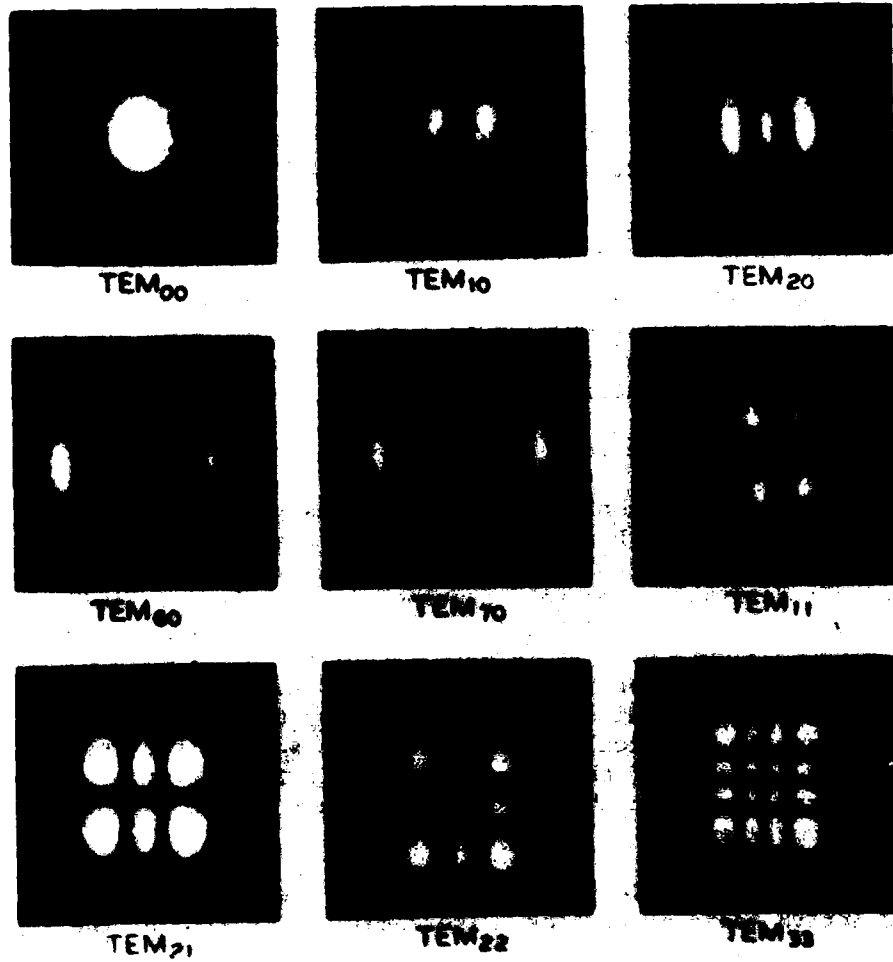
Figure 2. Symmetric confocal resonator.

TEM$_{00}$ TEM$_{10}$ TEM$_{20}$

TEM$_{60}$ TEM$_{70}$ TEM$_{11}$

TEM$_{21}$ TEM$_{22}$ TEM$_{33}$

Figure 3. Symmetric confocal resonator transverse modes [9].

7

(1.16)

ı determined from mirror separation, L, and
ıe g value of each mirror is given as _____

(1.17)

(1.18)

determine whether or not a reasonator is de-
rdingly, for a stable resonator,

(1.19)

(1.20)

round trips of a planar resonator (Fabry-
ıce to a steady-state solution has been
ırge, even for a small Fresnel number where
ı expected [6].

l resonator does not have the problems noted
ctive coupling results in large mode volume
hat" near-field fluence distribution with
tion properties in the far-field. We will
ive branch confocal unstable resonator [1,14]
resonator consists of a small convex
ncave 'primary" mirror set at a common focus.
is determined by the active media cross
ometry. Figure 4 shows the resonator and
eometric axis in the center of the two
xis in the corner of the feedback mirror

this resonator are predetermined by cavity
s. The focal length (f_1) of the feedback

(1.21)

ined previously. The geometric outcoupling
or magnification, M, as

(1.22)

GEOMETRIC
BEAM PROFILE

GEOMETRIC
BEAM PROFILE
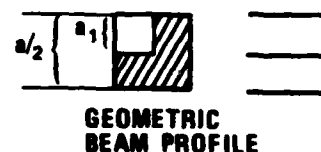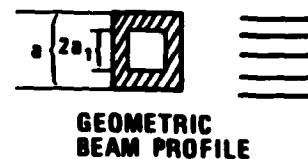
COMPLI

Figure 4. Geometry of the

The transverse modes of such
orthogonal. The higher order
not lend themselves to a stra
resonators.

The eigenvalue equation

$$\lambda_m U_m(x,y) = \iint K(x,y,$$

where λ_m is the complex eiger
that propagates the complex c
in the resonator. The eigen1
equation are the transverse ı
$U_o(x,y)$ is the predominant mı
fractional power loss per roı
number of passes, higher losı
provided inside the resonato
higher loss modes can mainta
important difference between

.s that the orthogonality relations over the cross sections are of the form

$$\iint U_n U_m \, dxdy \propto \delta_{nm} \tag{1.24}$$

rather than

$$\iint U_n^* U_m \, dxdy \propto \delta_{nm} \tag{1.25}$$

where δ_{nm} is the Kronecker delta, and the total power cannot be expressed as the sum of the powers carried by the individual modes U_n, U_m.

For mirrors having rectangular symmetry as illustrated above, the eigenfunctions are separable in x and y and are in the form $U_n(x) \, U_m(y)$. Figure 5 shows a calculation of amplitude and phase of $U_0(x)$ across a single transverse dimension [17]. The diffractive rippling of the near-field as seen in the intensity $|U_0(x)|^2$ gives the two-dimensional near-field burn pattern of Figure 6 as a characteristic "plaid" appearance which increases in fine structure with increasing Fresnel number. Figure 7 shows the far-field pattern for the near-field distribution of Figure 6.

Higher order modes of rectangular unstable resonators have been calculated by numerical techniques [17,18,19] and analytic techniques involving asymptotic expansion of the integral equation [20,21]. An interesting result is seen when one plots the power losses $\{1-|\lambda_n|^2\}$ for an unstable resonator. Figure 8 [18] shows the four lowest loss modes versus equivalent Fresnel number,

$$F_{eq} = \frac{M-1}{2M^2} N_T \tag{1.26}$$

where M is the resonator magnification and N_T is defined as the tube Fresnel number,

$$N_T = \frac{(a/2)^2}{\lambda L} . \tag{1.27}$$

It is interesting to note that at low equivalent Fresnel number the modes are entwined in a characteristic oscillating pattern with the lowest loss mode (δ) eventually separating from the rest at higher Fresnel numbers.

In the region of low equivalent Fresnel number ($F_{eq} < 100$), the most interesting results derived from detailed theoretical studies [16] are:

(1) the lowest loss mode is always symmetric;

(2) the greatest mode loss separation occurs at F_{eq} = integer + .5;
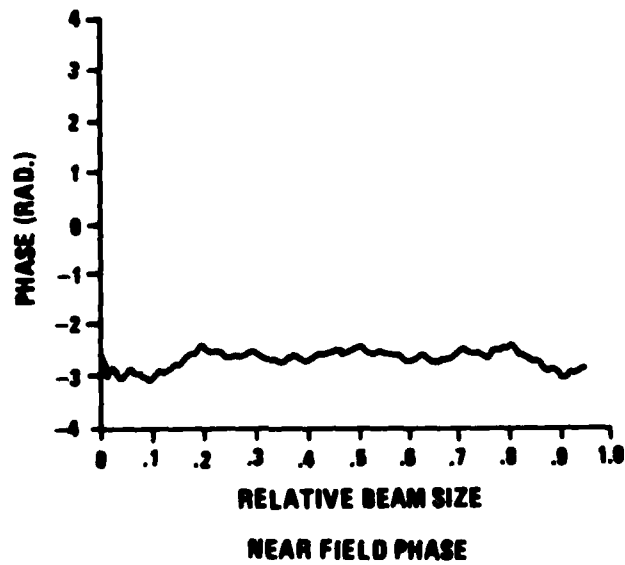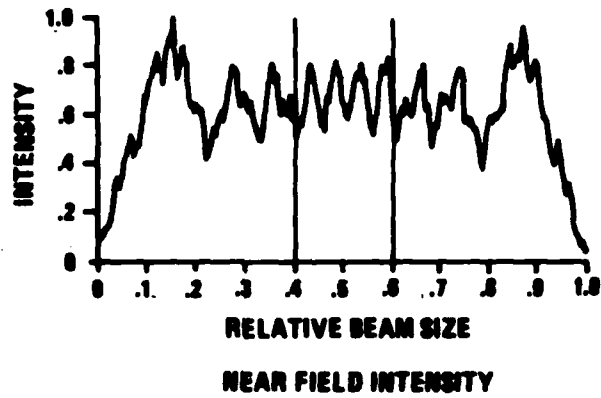
Figure 5.   Lowest loss mode for an unstable confocal strip
            resonator, M = 5.   The vertical lines are the
            geometric outline of the feedback mirror [17].

Figure 6. Near-field burn pattern, M = 1.32, N_T = 279. Vertical gaps are caused by the feedback mirror holding struts. The pattern is actual size.

Figure 7. Far-field pattern of Figure 6 at 136 meters. Actual size pattern.
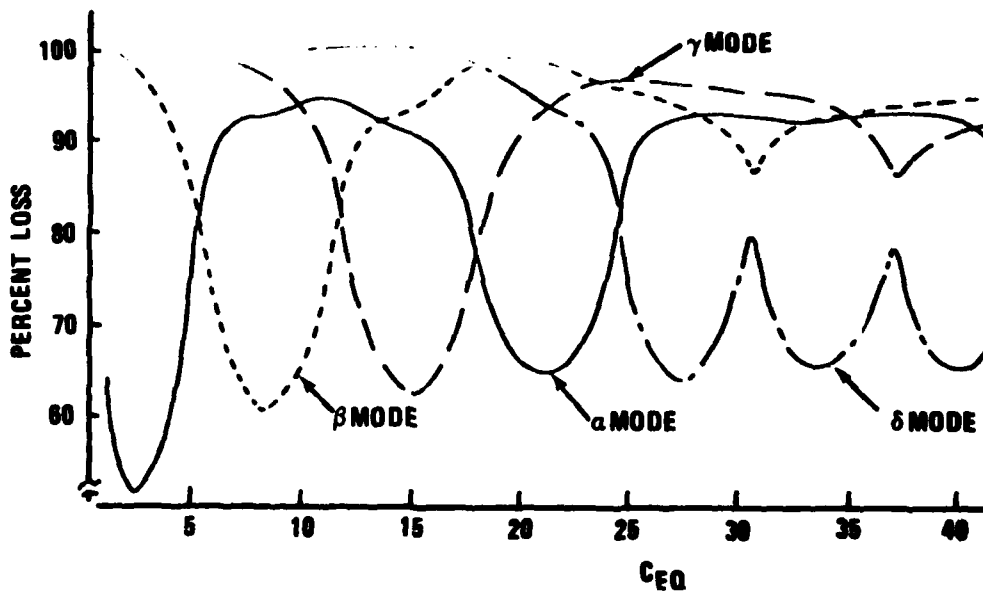
Figure 8. Calculation of the four lowest loss transverse symmetric Modes, $M = 3.3^{18}$ ($C_{eq} = 2\pi\ F_{eq}$).

13

(3) equal mode loss for two modes occur at mode crossing points of F_{eq} = integer + .875. Although $|\lambda_m|$ is equal for the two modes, the phase is distinct and different for each mode;

(4) antisymmetric modes are possible.

The lowest loss and higher loss modes may be obtained by a numerical technique using Fourier transform methods to simulate wavefront propagation within the resonator [22,23]. This kind of calculation utilizes a self-consistent approach in which the wavefront of the n+1 round trip resembles the wavefront of the nth round trip to an arbitrarily small difference. These techniques have been modified to obtain a theoretical basis for the transverse mode formation work described in this text. A description of steady-state mode calculations in unstable resonators by the Fourier transform approach follows: the lowest order mode is calculated from the wave equation, which is a differential equation analog of the integral eigenequation (1.23) with the appropriate boundary conditions of the unstable resonator. The wave equation may be obtained directly from Maxwell's equations in a homogeneous media [24]:

$$\nabla \times \overline{E} = -\frac{\partial \overline{B}}{\partial t} \tag{1.28}$$

$$\nabla \times \overline{H} = \overline{J} + \frac{\partial \overline{D}}{\partial t} \tag{1.29}$$

$$\overline{D} = \epsilon \overline{E} \tag{1.30}$$

$$\overline{B} = \mu \overline{H} \tag{1.31}$$

where $\widetilde{E}$ is the electric field, $\overline{H}$ is the magnetic field, $\overline{B}$ is the magnetic induction, $\overline{D}$ is the electric displacement and $\overline{J}$ is the current density, ϵ and μ, the electric permittivity and magnetic permeability of the medium, respectively.

The customary paraxial assumptions of light propagation in a homogeneous, isotropic medium are made, i.e.,

$$\nabla (\nabla \cdot \overline{E}) = 0 \tag{1.32}$$

$$\left|\frac{\partial^2 \psi}{\partial Z^2}\right| << k \left|\frac{\partial \psi}{\partial Z}\right| \tag{1.33}$$

with $\frac{\partial^2 \psi}{\partial Z^2}$ and $\frac{\partial \psi}{\partial Z}$ the propagation components of the wave equation along the Z-axis and k, the propagation number. It has been shown that these approximations are valid to zero order derivation of Maxwell's equations for inhomogeneous media with focusing, diffraction, and gain, e.g., active lasting media [25].

To derive the wave equation, we begin with the vector identity

14

$$\nabla \times \nabla \times \overline{E} = \nabla (\nabla \cdot \overline{E}) - \nabla^2 \overline{E} \quad . \tag{1.34}$$

Using Equation (1.32) this further reduces to

$$\nabla \times \nabla \times \overline{E} = -\nabla^2 \overline{E} \tag{1.35}$$

Incorporating Equations (1.28) and (1.31) into (1.35):

$$\nabla \times \nabla \times \overline{E} = - \frac{\partial (\nabla \times \overline{B})}{\partial t} = \frac{-\mu \partial (\nabla \times \overline{H})}{\partial t} \quad . \tag{1.36}$$

Now, Equation (1.29) is substituted into Equation (1.36) with the assumption that no electrical currents are flowing in the media, i.e., $\overline{J} = 0$. This gives

$$-\mu \frac{\partial (\nabla \times \overline{H})}{\partial t} = -\mu \frac{\partial^2 \overline{D}}{\partial t^2} \quad . \tag{1.37}$$

Finally, using the relation of Equation (1.30), we have

$$-\mu \frac{\partial^2 \overline{D}}{\partial t^2} = -\mu\varepsilon \frac{\partial^2 \overline{E}}{\partial t^2} \tag{1.38}$$

and therefore, since $\mu\varepsilon = \frac{1}{c^2}$

$$\nabla^2 \overline{E} = \frac{1}{c^2} \frac{\partial^2 \overline{E}}{\partial t^2} \quad . \tag{1.39}$$

The vector equation may be simplified by assuming a plane polarized wave-front

$$\overline{E} (x,y,z) = U(x,y,z) \hat{E}^{i\omega t} \quad . \tag{1.40}$$

Substituting $\overline{E}$ into Equation (1.39) removes the temporal and vector dependence to give the Helmholtz Equation

$$\nabla^2 U = - \frac{\omega^2}{c^2} U \tag{1.41}$$

with

$$k^2 = \frac{\omega^2}{c^2} \quad . \tag{1.42}$$

Considering the paraxial movement of light through the medium, U may be decomposed into a slowly varying component multiplied times the characteristic plane wave propagation at a single frequency:

15

$$U(x,y,z) = \psi(x,y,z) \ e^{ikz} \quad . \tag{1.43}$$

Substituting this assumption for U into Equation (1.41) we obtain

$$\nabla^2 U + k^2 U = \frac{\partial^2 \psi}{\partial x^2} + \frac{\partial^2 \psi}{\partial y^2} + \frac{\partial^2 \psi}{\partial z^2} + 2 \ ik \ \frac{\partial \psi}{\partial z} = 0 \qquad , \tag{1.44}$$

and applying the paraxial approximation

$$\left| \frac{\partial^2 \psi}{\partial z^2} \right| \ << \ k \ \left| \frac{\partial \psi}{\partial z} \right| \tag{1.33}$$

we obtain the wave equation of propagation

$$\frac{\partial^2 \psi}{\partial x^2} + \frac{\partial^2 \psi}{\partial y^2} + 2 \ ik \ \frac{\partial \psi}{\partial z} = 0 \quad . \tag{1.45}$$

The Fourier transform lends itself readily to the solution of Equation (1.45). To se this, we examine a basic property of these transforms. The Fourier transform of ψ in the x dimension is given as

$$T_x \ (\psi) = \tilde{\psi} = \int_{-\infty}^{\infty} e^{-ipx} \ \psi(x) \ dx \tag{1.46}$$

then,

$$T_x\left(\frac{d\psi}{dx}\right) = \int_{-\infty}^{\infty} e^{-ipx} \ \frac{d\psi}{dx} \ dx \quad . \tag{1.47}$$

Integrating by parts we get

$$T_x\left(\frac{d\psi}{dx}\right) = \left. \right|_{-\infty}^{\infty} e^{-ipx} \ \psi + ip \int_{-\infty}^{\infty} e^{-ipx} \psi dx \ . \tag{1.48}$$

Since $\psi \ (x,y,z)$ vanishes at infinity we get

$$T_x \ \frac{d\psi}{dx} \ = i \ p \ T_x(\psi) = ip\tilde{\psi} \quad , \tag{1.49}$$

by a similar procedure

$$T_x\left(\frac{d^2\psi}{dx^2}\right) = -p^2 \ \tilde{\psi} \qquad . \tag{1.50}$$

Taking the Fourier transform of x and y in Equation (1.45) we have

$$-(p^2 + q^2)\ \tilde{\psi} + 2\ ik\ \frac{d\tilde{\psi}}{dz} = 0 \quad . \tag{1.51}$$

The transformed wavefront $\tilde{\psi}$ may be readily propagated from z_o to z_1 by solution of Equation (1.51):

$$\frac{d\tilde{\psi}}{\tilde{\psi}} = \frac{(p^2 + q^2)}{2\ ik}\ dz \tag{1.52}$$

$$\ln \tilde{\psi}\ (p,q,z_1) - \ln \tilde{\psi}\ (p,q,z_o) = \frac{p^2 + q^2}{2\ ik}\ (z - z_o) \quad . \tag{1.53}$$

Therefore, by the property of logarithms,

$$\tilde{\psi}(,q,z_1) = \tilde{\psi}\ (p,q,z_o)\ e^{\frac{-i(p^2 + q^2)}{2k}\ (z_1 - z_o)} \quad . \tag{1.54}$$

The propagated complex amplitude may then be readily obtained as

$$(x,y,z_1) = T_{x,y}^{-1}[\tilde{\psi}(p,q,z_1)] \quad . \quad \pm \tag{1.55}$$

Thus, an arbitrary wavefront may be launched within the confines of an unstable resonator by using this method. The direct and inverse Fourier transforms are calculated numerically as is described in a later chapter.

Far-field calculations and experiments show that the Fraunhofer diffraction pattern from the unstable resonator is essentially the far-field pattern obtained from a constant phase-constant amplitude wavefront illuminating the geometric aperture [21,26,27,28]. The far-field pattern of this case has been calculated for centered as well as completely decentered obscurations for the empty cavity case. Calculations using gain appear to give similar results [29,30].

C. Discussion of Relevance of the Problem

The goal of this research was to examine the temporal evolution of transverse modes in moderate magnification ($1.32 \leq M \leq 2.70$), positive branch confocal unstable high energy laser resonators. Toward this end, the far-field irradiance (fluence) distribution has been observed in arbitrary time slices during and following the period of mode formation. The geometrical theory of Anan'ev was compared to experimental results and statistical analytical modeling in this work.

The phenomenon of mode formation is illustrated schematically in Figure 9. A resonator cavity is shown with active media on the left with a resultant far-field irradiance distribution on the right. At threshold ($t - o$), radiation

(a) t = 0

(b) t = 200 ns

(c) t = 1000 ns.
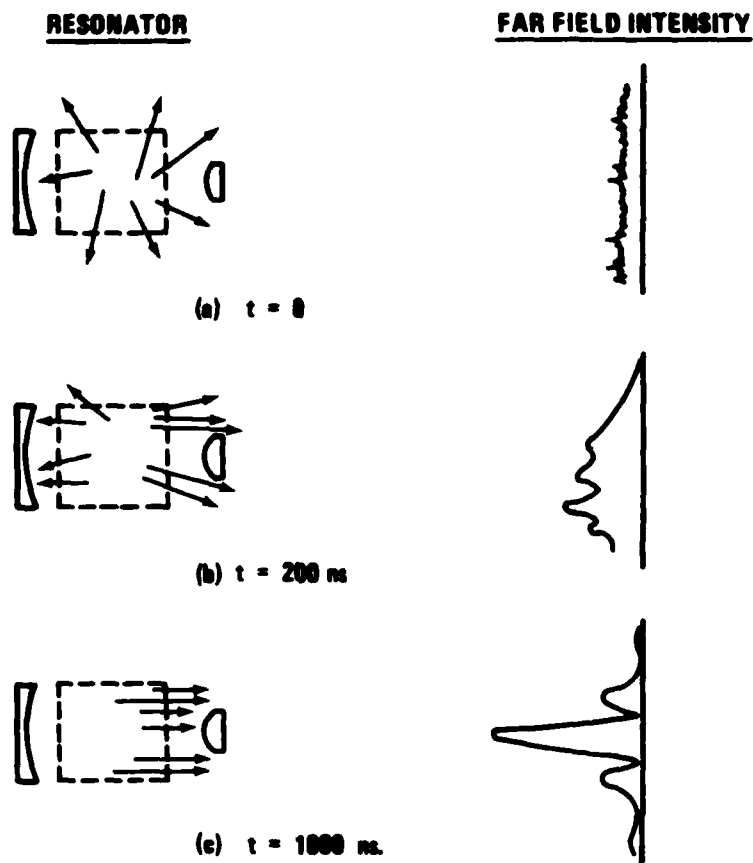
Figure 9. Mode formation observed in the far-field.

is emitted spontaneously in all directions, the far-field irradiance being
exemplified by low level noise. At a later time during mode formation
(t - 200 nsec), a far-field pattern is beginning to form, represented by
skewed and displaced peaks. Finally, at a time longer than that of mode
formation (t - 1000 nsec), a far-field irradiance distribution has stabilized
to form the distribution characteristic of steady-state mode generation.

A situation can readily exist in which the spontaneous emission and gain
in the resonator are high at threshold. In this case a large initial intensity
builds up and saturation of flux can occur during the period of predicted mode
formation. If this is indeed the case, a sizeable percentage of the total
energy output from a pulsed laser may be lost by mode formation effects from
the central lobe of far-field pattern.

Notable high energy pulsed lasers which have short start-up times and fall
under the category described above, are rare gas halide (excimer) lasers,
metal vapor lasers, and chemical lasers. Some work has been done on mode
formation and beam quality for copper vapor and excimer lasers utilizing un-
stable resonators [2,4,31]. These experiments examined resonators with
magnifications which were relatively large ($\geq$ 8) and thus had mode formation
times of the order of tens of nanoseconds. Several authors have derived

estimates of mode formation time based upon the geometric theory approach [2, 4,5,31,32], but experimental data is lacking in the lowermagnification region of interest for high energy excimer and chemical lasers ($1 < M < 3$). Resonators in this regime are predicted to have mode formation times in the hundreds of nanoseconds.

The prospect of mode formation times of a few hundred nanoseconds does not bode well for high energy excimer and chemical lasers. Near-field power turn-on in excimer systems has been observed in the 50 to 200 nanosecond regime [33]. This has been confirmed independently by the author and J. Oldenettel in unpublished work. Pulsed chemical lasers are seen to have 10 to 40 lines, which turn on during a 3 microsecond pulse; each line being active for one to a few hundred nanoseconds [34]. Thus, mode formation can create a serious problem for these lasers with delivery of a divergent beam to the far-field in the initial portion of the pulse.

The problem may be succinctly stated as follows: certain common lasers used in pulsed high energy laser systems may be inefficient in delivery of far-field energy because of finite mode formation time. A confirmation of the geometrically predicted limit has been attempted in this treatise through experimental investigation and statistical computational modeling.

II. EXPERIMENTAL RESULTS

A. Description of Lasers Used in This Work

1. Types of Lasers

It is desirable to validate transverse mode formation time defined by Equation (1.2) over the range of values of variables encountered in practical high energy lasers. As discussed in Section 1, this phenomenon may be of critical importance in the design and implementation of a high energy laser system. To experimentally measure mode formation an ideal laser would have the following characteristics:

a. high initial spontaneous emission

b. high gain

c. good active medium quality

d. variable magnification

e. variable Fresnel number

Characteristics a, b, and c refer to the lasing medium. It would be desirable for the laser to "turn on" quickly after threshold and saturate so that near-field output power is nominally constant and far-field measurements reflect mode formation properties. In addition, the active medium must not contribute time varying phase distortions which would confuse far-field measurements. Parts d and e relate directly to Equation (1.2) through the resonator geometry. In regions of low magnification, M becomes the predominant factor in the denominator. Fresnel number may vary over a large range but is not as important as M because of the logarithmic relationship.

19

Practical considerations dictate the types of lasers to be utilized in these measurements. Two high energy lasers were chosen: a pulsed CO_2 laser located at Redstone Arsenal, AL; [35,36] and a pulsed XeF laser at Maxwell Laboratories, Inc., in San Diego, CA [37,38]. These lasers are very similar both in design and application. Figure 10 represents the combined features of each laser. Table I contains the electrical and geometrical parameters of these lasers.
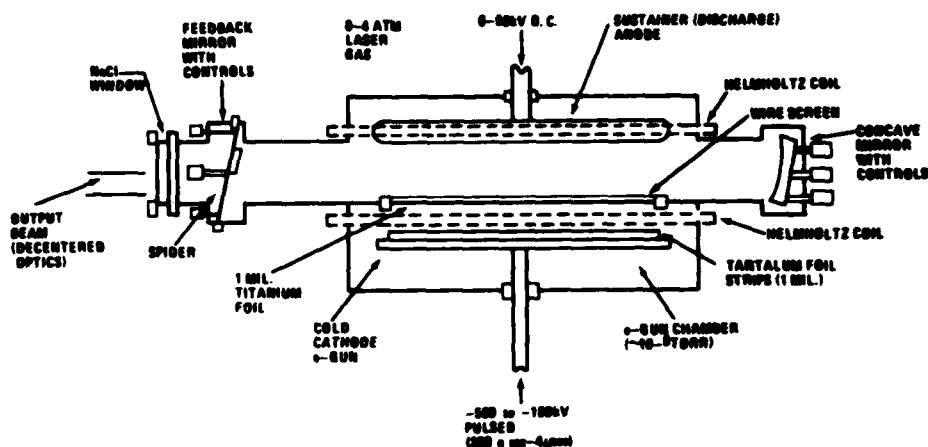
Figure 10. Pulsed high energy laser schematic.

The CO_2 laser consisted of three basic units: the electron beam (e-beam) supply which ionized the laser gas, the resonator cavity containing the active laser media with unstable confocal resonator optics, and the discharge supply—a DC source which maintained a constant voltage across the laser cavity and determines the gain in the active lasing medium. The e-beam was a cold cathode emitter type; electrons were emitted from the edges of .001 in. thick tantalum foil strips on the cathode assembly. The e-beam pulse length was variably controlled up to 4 microseconds with a nominal voltage of 180 kV. The e-beam gun chamber was held at low pressure ($\sim 1 \times 10^{-6}$ Torr) and was separated from the laser cavity by a .001 in. thickness titanium foil. The current density of the e-beam on the cavity side of the foil was approximately 0.5 amperes/cm^2 for a beam dimension of 10 x 100 centimeters. The laser cavity had an active volume of 10 x 10 x 100 centimeters separated on the longitudinal axis by unstable confocal positive branch resonator mirrors. For these experiments, the resonator mirror pair had a magnification, M, of 1.32 at a confocal spacing of 289 cm. The convex mirror (feedback mirror), which is 7.5 cm in diameter, gave an output beam of 9.9 cm through a NaCl output window. The concave reflector (primary mirror) was oversized at 16 cm diameter. The mirrors were separated by L - 337.5 cm to give focusing at 136 meters, the nominal position for far-field analysis of the laser beam. In terms of resonator g parameters defined by Equation (1.17), focusing in terms of units of mirror separation, L, as per Siegman [12] is given as

$$F' = \left| [(\sqrt{g_1 g_2 (g_1 g_2 - 1)} + g_1 g_2 - g_1]^{-1} g_1 \right| \tag{2.1}$$

TABLE I. LASER SYSTEM PARAMETERS

Parameter	CO_2 Laser	XeF Laser
Laser Wavelength	10.6 μ	0.3532 μ
Pulse Length (In Experiments)	0.02–1.0 μsec	0.2–0.8 μsec
Pulse Energy (In Experiments)	30 J	35 J
Laser Gas Mix (In Experiments)	1:1 CO_2:He	1:3:1140 NF_3:X_e:N_e
Cavity Pressure (In Experiments)	456 Torr	1520–3040 Torr
Active Media Dimensions	10x10x100 cm	10x20x200 cm
Resonator Magnification	1.32	1.32, 2.7
Mirror Separation	338 cm	262 cm
Output Beam Size	10x10 cm	10x20 cm
Geometric Outcoupling	0.426	0.426, 0.863
Beam Shape (Obscuration)	Decentered	Centered
Tube Fresnel Number	279	2700; 10,800
Mode Formation Time	489 nsec	513, 168 nsec
E-Beam Voltage	180 keV	300–500 keV
Discharge Voltage	0–50 keV	0
Guide Field Current	0	300 A

where in this case LF′ = 136 meters. The mirror radii of curvature may be determined by Equations (1.8), (1.9), and (1.21) and used in Equation (1.17). The laser medium was a mixture of equal parts of carbon dioxide and helium at 456 Torr pressure. Transverse pumping of the laser gas was performed by a DC discharge carbon/graphite anode of somewhat larger dimensions than the 10 x 100 cm e-beam area facing the e-beam cathode foil with 11 cm separation. The anode was preset in a range of 40 - 50 kV during the e-beam pulse. The e-beam determines the approximate laser pulse length.

The discharge supply provided the basic pump mechanism of the CO_2 laser. This is a source of DC current which is arbitrarily chosen for a given pulse. A DC supply charges a set of capacitors which are then discharged ("crowbarred") after cessation of the e-beam pulse. The actual CO_2 laser assembly used for these measurements is shown in Figure 11, without the resonator mirrors.

Figure 11. CO₂ laser.

The XeF laser was very similar to the CO_2 laser in construction. However, the e-beam was a higher voltage (300 - 500 kV) and the dimensions were larger (20 cm high by 200 cm long) than those of the CO_2 laser. The basic pumping mechanism in the XeF laser was through direct e-beam initiation; no DC discharge was used. The mirrors were set at the confocal spacing of 262 cm. Two resonator mirror-pairs were chosen for the experiments: an M = 1.32 set and M = 2.7 set, which gave a reasonable range of mode formation times according to Equation (1.2). The cavity pressures in this laser were higher than in the CO_2 laser, being in the range of 2 - 4 atmospheres. The typical active lasing medium was 10 x 20 x 200 cm in volume with a gas mixture ratio of 1 to 3 to 1140 for nitrogen tribluoride (NF_3) to xenon to neon. A magnetic guide field was produced by a pair of Helmholtz coils surrounding the cavity for e-beam confinement. The laser used for these measurements is shown in Figure 12.

2. Pumping Mechanisms

The value of small signal gain, γ_o, is determined by the following equation [39]

$$\gamma_o = \frac{\lambda^2 g(\nu)}{\eta^2 8\pi t_{spont}} \left(N_2 - N_1 \frac{g_1}{g_2} \right) \tag{2.2}$$

where λ is the wavelength of the laser line, $g(\nu)$ is the absorption normalized lineshape, η is the index of refraction, t_{spont} is the spontaneous emission lifetime of the medium N_2 and N_1 are the upper and lower laser level populations;

22
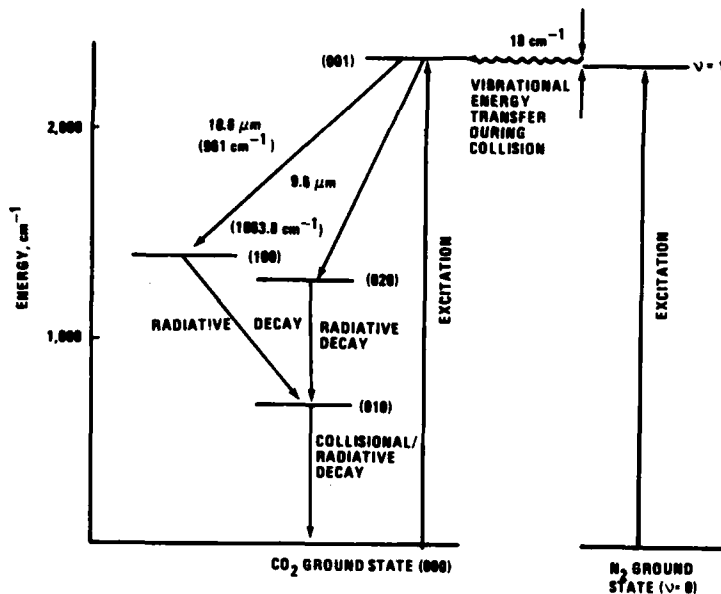
Figure 13.   Pumping scheme for the pulsed CO_2 laser [43]
(Nominal 3:2:1, He:N_2:CO_2 Mix).

The lower level (100) is quickly deactivated by collisional/radiative processes to the ground state. Collisional deactivation is increased with the aid of the He diluent.

The gain in the transversely pumped high pressure CO_2 laser has been shown to be proportional to E/N [44,45,46] where E is the transverse discharge field (in volts/cm) and N is the number of molecules per cubic centimeter (proportional to pressure).

The XeF laser kinetics are not straightforward as compared to the CO_2 laser. A number of complicated paths are possible for activation of the upper laser level represented by XeF*. These are shown in Figure 14 [47]. The major energy flow paths in the Figure are given as:

a.   pumping electrons $\rightarrow$ Ne$^+$ $\rightarrow$ NeF* $\rightarrow$ F* $\rightarrow$ Xe$^+$ $\rightarrow$ XeF*

b.   pumping electrons $\rightarrow$ Ne* $\rightarrow$ Xe$^+$ $\rightarrow$ XeF*

c.   pumping electrons $\rightarrow$ Xe$^+$ $\rightarrow$ XeF*

d.   pumping electrons $\rightarrow$ Xe* $\rightarrow$ XeF*

These expressions are not equations, but are shown only as examples of energy flow to illustrate the complexity of XeF pumping. With the pressures and diluent ratios of neon or argon described in this work, the B $\rightarrow$ X state

24

Figure 14. Major energy flow pathways in E-Beam pumped Ne/Xe/NF$_3$ mixtures [47].

(3532 Å) is pumped [48]. The lower level of this state was originally thought to be purely dissociative., i.e.,

$$2XeF^* \rightarrow 2Xe + F_2 + \nu \quad . \tag{2.5}$$

However, a bound state of XeF exists in the lower level below approximately 500°C, which reduces the overall population inversion and gain.
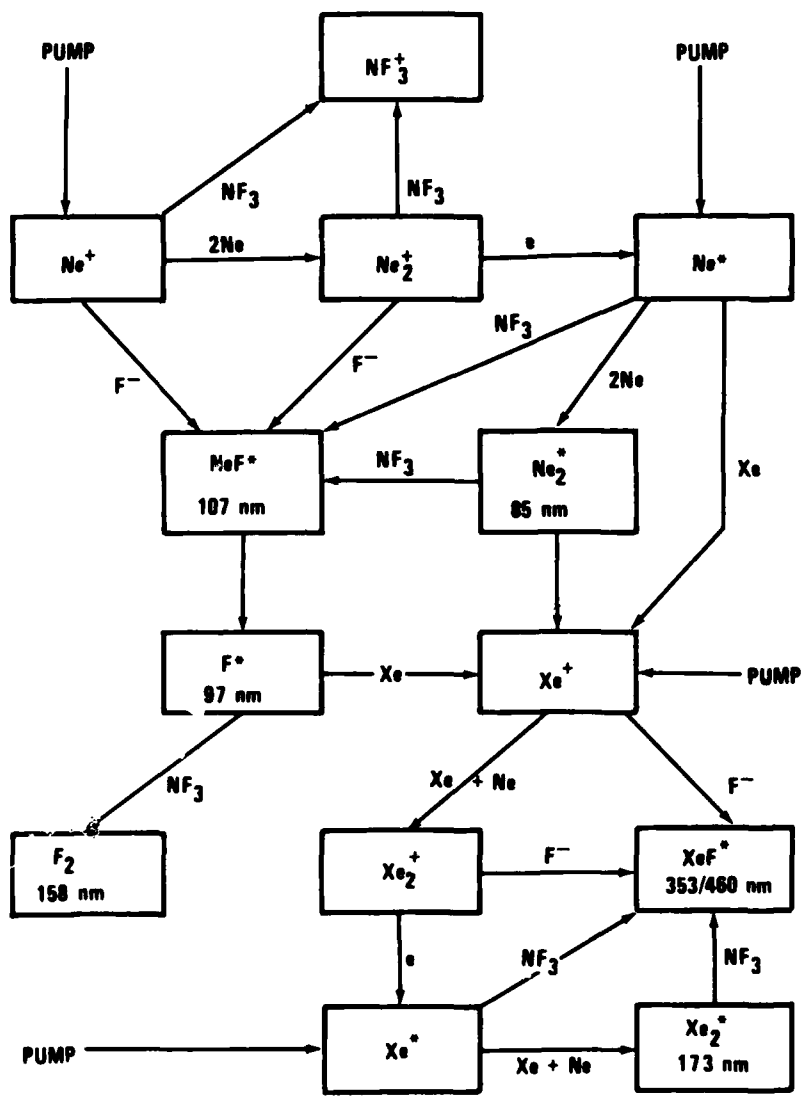
B. Small Signal Gain Measurements in CO_2 Lasers

The time of transverse mode formation, Equation (1.2), is measured from the time at which threshold gain, g_o, is achieved, i.e., feedback power over one round trip pass equals out coupled power. The method for measuring threshold gain is illustrated by Figure 15. This is shown for CO_2; similar measurements are possible for XeF with substitute of a suitable detector and probe laser and will be explained later. The experiment involves a single pass CO_2 probe laser turned to the high energy laser line and a high speed detector to make small signal gain measurements. DC levels of $I = 0$ and I_o are determined and the high energy laser is pumped under experimental operating conditions. The temporal history of the power increase, dI/dt, is measured as a function of time for each pumping condition. The expression for gain in a single pass is given as

$$\frac{I(t)}{I_o} = e^{g_o(t)\ell} \tag{2.6}$$

where ℓ is the active medium length. In actual high energy laser operation the threshold for a single round trip in the resonator occurs at

$$\frac{I'(t)}{I_o'} = M^2 = e^{2g_o(t)\ell} \tag{2.7}$$

where $I'(t)$ and I_o' are intensities measured under saturable gain conditions. Therefore,

$$M = e^{g_o(t)\ell} = \frac{I(t)}{I_o} \tag{2.8}$$

and threshold gain occurs when I/I_o is equal to the resonator magnification. The increase in I is related to a reference signal which is available during high energy lasing. This reference signal is the current produced by the electron beam entering the laser cavity (e-beam postfoil current).

Figure 15 shows the mechanics of making gain measurements with the Systems, Science, and Software (S^3) pulsed CO_2 laser with optics removed. A CW CO_2 laser set on the pulsed laser line (P-20) is transmitted through the S^3 laser to an RF shielded fast response mercury-cadmium-telluride detector. The

26
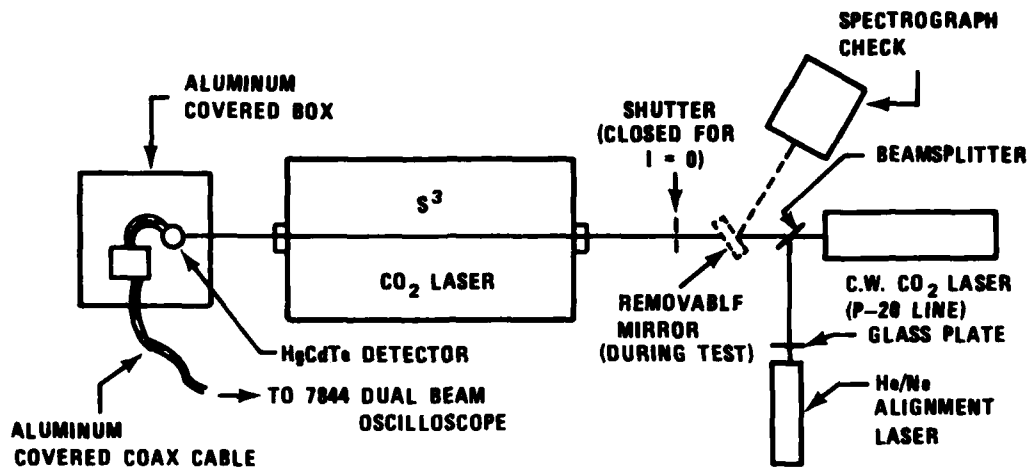
Figure 15. Gain measurement schematic.

output signal is displayed on a 7844 dual beam oscilloscope. A spectrograph checks the P-20 line immediately before and after S^3 firing with the beam deflected with a removable mirror. A helium neon laser is used for visible alignment of all components, the helium neon beam following the path of the CW CO_2 beam. Zero level intensity (I = 0) is obtained by closing a shutter in front of the laser and allowing the oscilloscope to sweep immediately before the test.

Figures 16 through 20 show small signal gain measurements as a function of time for various gain (discharge voltage) settings at 456 Torr cavity pressure and 100 cm gain length. The bottom trace is the e-beam postfoil current, the trace one division above is the I = 0 line, and the upper trace is I = I(t) with the flat portion to the left giving I = I_o. Threshold gain is measured from the rise of postfoil current ot the point at which I/I_o = 1.32. Figure 20 is interesting in that I(t) is shown over the nominal duration of the e-beam pulse in which I/I exceeds 40 (small signal gain > 3.7%/cm.)
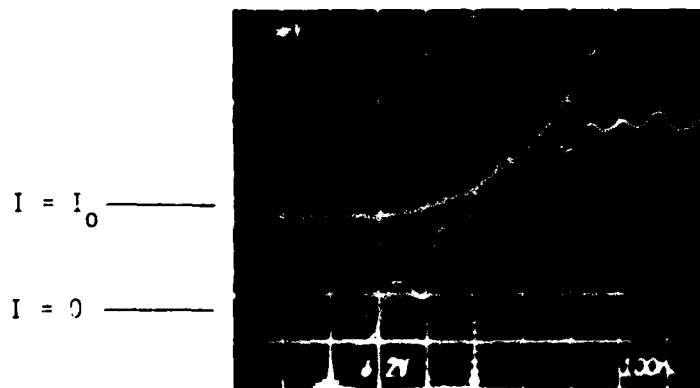
Figure 16. Small signal gain at 40.8 kV discharge voltage.

$I = I_0$

$I = 0$

Figure 17. Small signal gain at 46.9 kV discharge voltage.

$I = I_0$

$I = 0$

Figure 18. Small signal gain at 48.9 kV discharge voltage.

$I = I_0$

$I = 0$

Figure 19. Small signal gain at 50 kV discharge voltage.

Figure 21. Laser output at 40.8 kV discharge voltage.

Figure 22. Laser output at 46.8 kV discharge voltage.
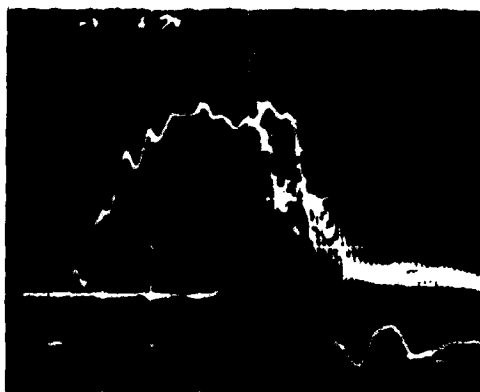
Figure 23. Laser output at 48.8 kV discharge voltage.

29

Figure 20.   Small signal gain at 47.9 kV discharge voltage $(I_o = 8\text{mV})$.

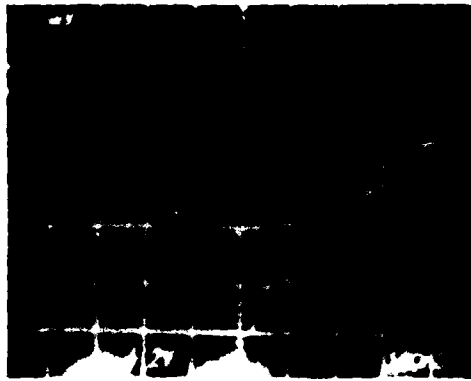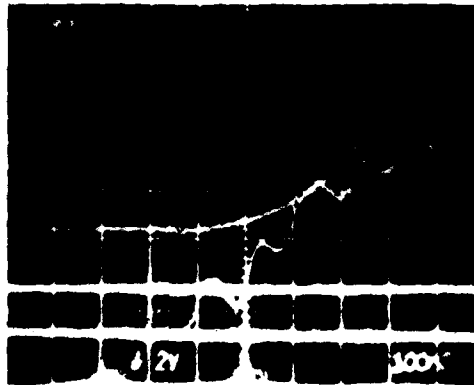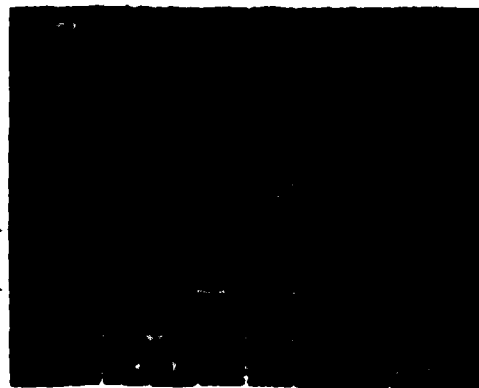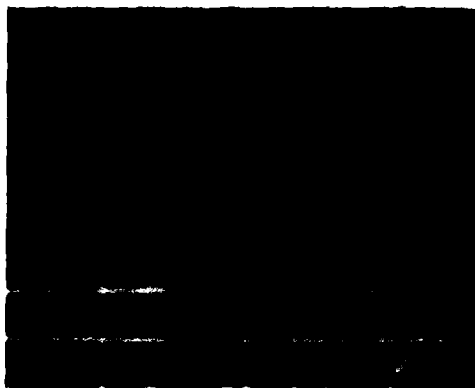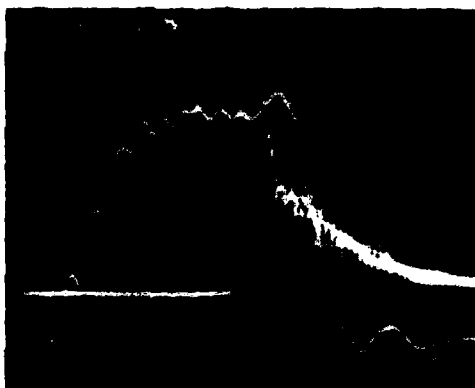Figures 21 through 24 show high power output from the S^3 laser with unstable resonator optics installed. The oscilloscope traces were taken with a 7441 photon drag detector in the near-field in the upper portion of the beam midway between anode and cathode. Again, the postfoil current is being used as a reference pulse and is the lower trace. The upper trace is the photon drag detector response. These photographs, along with Figures 16 through 19 of small signal gain, determine the time of threshold relative to the onset of high peak power from the laser by using the e-beam postfoil current as a reference marker. Increasing gain shortens the time between threshold and high peak output power from the S^3 laser. Transverse mode formation is measured from the threshold to a point required to produce a far-field burn pattern in these experiments. This occurs at a time determined by the onset of high peak power. The photon drag detector samples 2.3% of the total power in Figures 21 through 24. In the far-field measurements of mode formation time to be presented later, the detector sampled approximately 3% of the total power. The determination of burn pattern formation time from these figures assumes a rise in power of 40 mV on the scale of Figures 21 through 24, referenced to e-beam postfoil current rise time. Table II summarizes the results of burn pattern formation time and threshold gain time as a function of discharge voltage. The last column of numbers represents the actual mode formation time to obtain a far-field pattern burn and is the Anan'ev time for the following CO_2 experiments.

C.   Far-Field CO_2 Burn Patterns

The experimental arrangement for performing transverse mode formation is shown in Figure 25 and was placed at 136 meters from the S^3 laser. The laser beam focus is nominally at 136 meters. The beam is propagated an additional distance of 2.3 meters to a zinc selenide beamsplitter. Immediately behind the beamsplitter is a plastic sheet attenuator (3M infrared transparency) of < 30% transmission and Polaroid Sheet P_1 for recording long pulse (1.2 μ sec) burn patterns. This sheet is unexposed, developed Polaroid type 52 film. A front surface reflection from the beamsplitter is propagated 3.3 meters to concave mirror m_1 which focuses the beam at 1.2 meters with air breakdown at this position, P_2. The air breakdown is used as a fast plasma switch to clip all but the leading edge of the pulse. This is important in attempting to obtain a burn pattern at P_4 in the regime of mode formation as
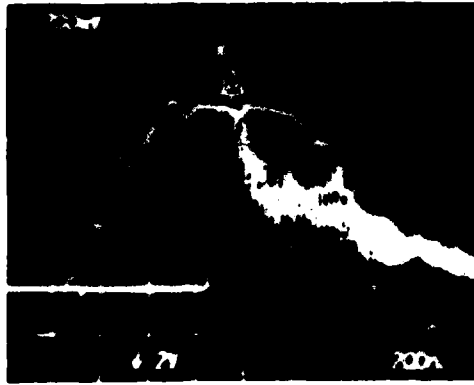
Figure 24. Laser output at 50 kV discharge voltage.

TABLE II. FAR-FIELD BURN PATTERN FORMATION TIME VERSUS DISCHARGE VOLTAGE.

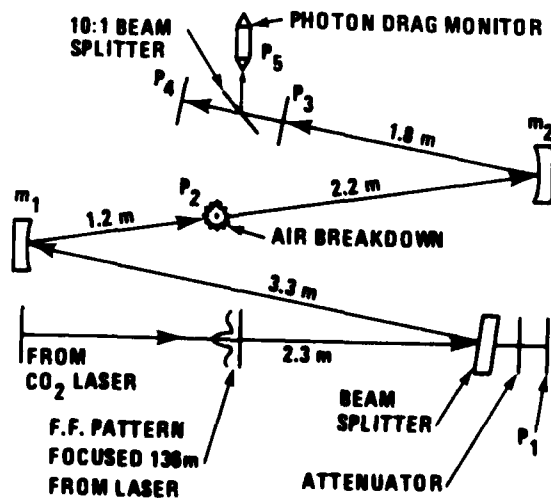| DISCHARGE VOLTAGE (kV)	BURN PATTERN FORMATION TIME (ns)	THRESHOLD GAIN TIME (ns)	MODE FORMATION TIME (ns)
40.8	740	220	520
46.8	650	190	460
48.8	640	180	460
50.0	620	180	440

Figure 25. Experimental schematic to obtain mode formation data.

predicted by Anan'ev. A long pulse burn pattern would have integrated
energy long after the transverse mode was expected to have been formed. After
air breakdown at P_2 occurs, the beam propagates an additional 2.2 meters to
concave mirror m_2 where the geometrical outline of the laser cavity is re-
imaged at P_3, a distance of 1.8 meters from m_2. At this position an aperture
stop is inserted. This is an oversized L-shaped hole which contains the image
of the near-field laser aperture. The purpose of the aperture stop is to
block rays of light transmitted after air breakdown at P_2. A beamsplitter is
positioned 2 cm downstream of the spatial filter. Ninety percent of the
clipped pulse forms a burn pattern at P_4. Ten percent of the beam is inter-
cepted by a photon drag detector at P_5. This signal is received by an os-
cilloscope which gives the temporal shape of the pulse.

The objective of these experiments was to obtain results as early as
possible in the temporal formation of a transverse mode. Toward this end
the E/N ratio of the 1:1 CO_2:He laser was maximized by setting the gas mixture
to 456 Torr. N_2 was not used because of its long N_2-CO_2 transfer time. The

discharge voltage was maximized in the regime of 40 to 50 kV to provide for
high initial gain; the e-beam pulse width was minimized to protect against
laser device damage; and the air breakdown plasma switch was used to produce
burn patterns representative of an early time in the pulse. The time of burn
pattern formation from threshold as a function of discharge voltage is given
in Table II.

Three sets of figures are representative of the burn patterns taken at P_4
of the clipped pulse in the far-field. Set I (Figures 26 through 29) was
taken at a discharge voltage of 40.8 kV which gives a burn pattern formation
of 520 nanoseconds – somewhat outside the nominal Anan'ev mode formation
prediction of 489 nanoseconds. Set II (Figures 30 through 33) is burns taken
with a discharge voltage of 47.8 kV, representing a burn pattern formed at
460 nanoseconds. Set III (Figures 34 through 37) was taken at the voltage
limit of the tests, with a discharge voltage of kV giving the shortest burn
pattern formation time of 440 nanoseconds.

An inspection of the three sets of figures shows a successive blurring
and subsequent loss of resolution in the far-field pattern—a result attri-
butable to mode formation. Set III, in face, has been blurred to an extreme
extent. Only the tip of the central maximum has sufficient fluence to burn the
Polaroid. This interpretation was corroborated by the photon drag detector
signal at P_3. Three representative temporal oscilloscope photographs are
shown in Figures 38 through 40 for 40.8 kV, 47.8 kV, and 50 kV discharge
voltages, respectively. The total energy obtained from integration of the
photon drag temporal response in each figure is approximately the same. One
can conclude that the energy was spread (blurred) over a larger area, as
anticipated from the dynamics of mode formation. However, the energy was
collected in a sufficiently large area by the photon drag detector to compen-
sate for the blurring of the far-field pattern, and recorded the same energy
for Figures 38 through 40.

Figure 41 is representative of all long pulse burn patterns taken at P_1
simultaneously with the patterns taken at P_4. The purpose of this burn is to
illustrate the quasi-steady-state far-field pattern from the laser. The burn
pattern in this figure has formed at least 1,000 nanoseconds after threshold.
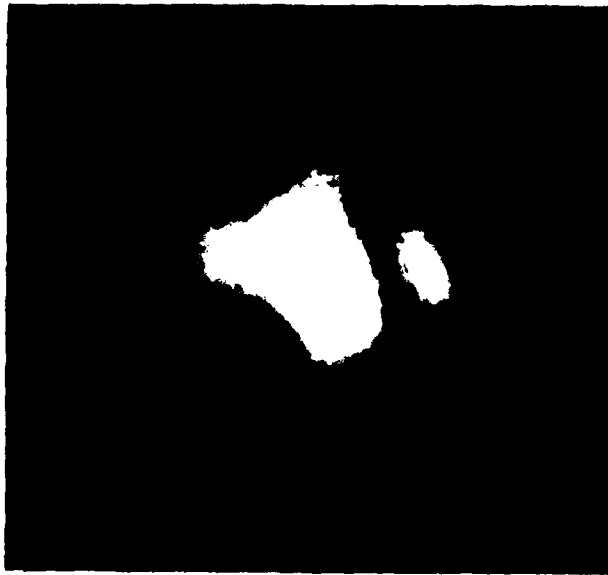
Figure 26.   Far-field pattern taken at 40.8 kV discharge
             (Shot number 7174) 7X enlargement.)
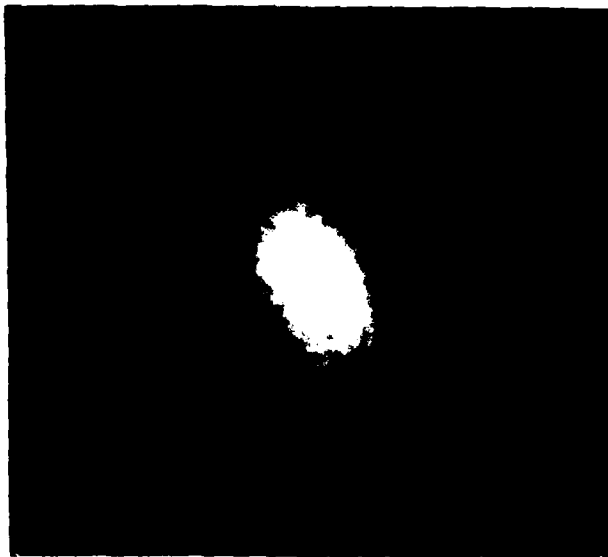
Figure 27.   Far-field pattern taken at 40.8 kV discharge
             (Shot number 7156) 7X Enlargement.
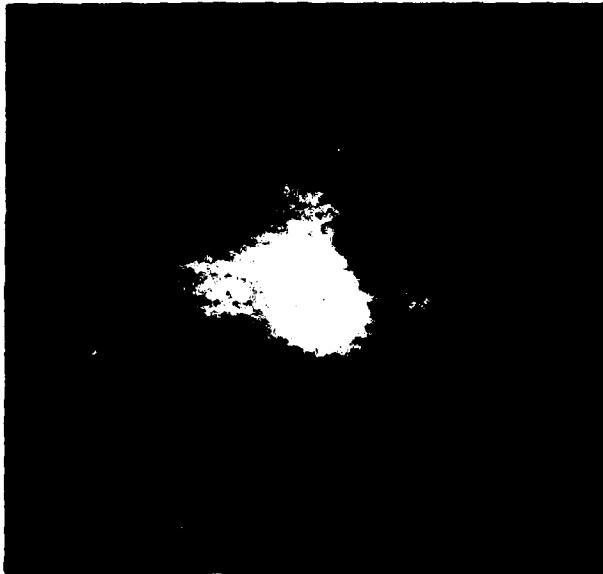
Figure 28. Far-field pattern taken at 40.8 kV discharge
(Shot number 7207) 7X enlargement.
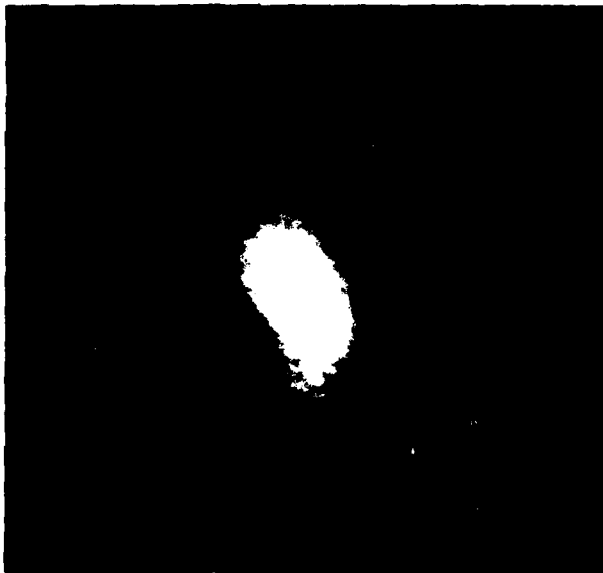
Figure 29. Far-field pattern taken at 40.8 kV discharge
(Shot number 7154) 7X enlargement.
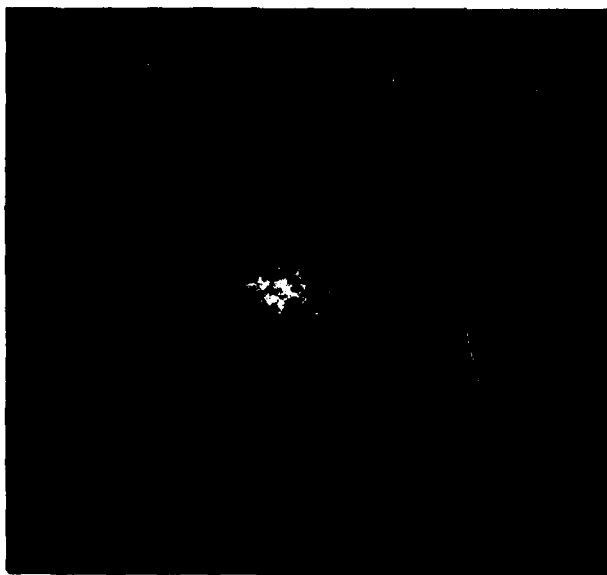
Figure 30. Far-field pattern taken at 47.8 kV discharge
(Shot number 7197) 7X enlargement.

Figure 31. Far-field pattern taken at 47.8 kV discharge
(Shot number 7210) 7X enlargement.

Figure 32. Far-field pattern taken at 47.8 kV discharge
(Shot number 7208) 7X enlargement.
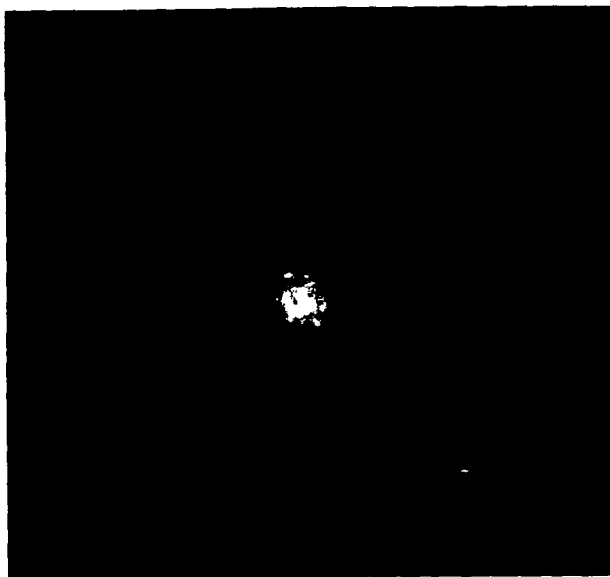
Figure 33. Far-field pattern taken at 47.8 kV discharge
(Shot number 7196) 7X enlargement.
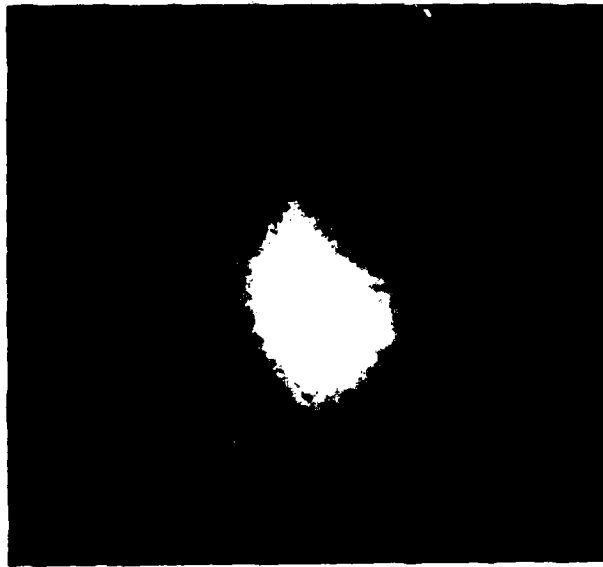
Figure 34.   Far-field pattern taken at 50 kV discharge
             (Shot number 7198) 7X enlargement.
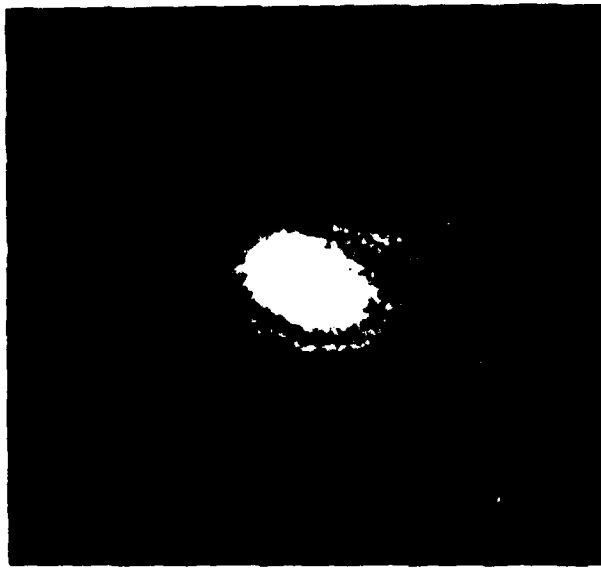
Figure 35.   Far-field pattern taken at 50 kV discharge
             (Shot number 7219) 7X enlargement.
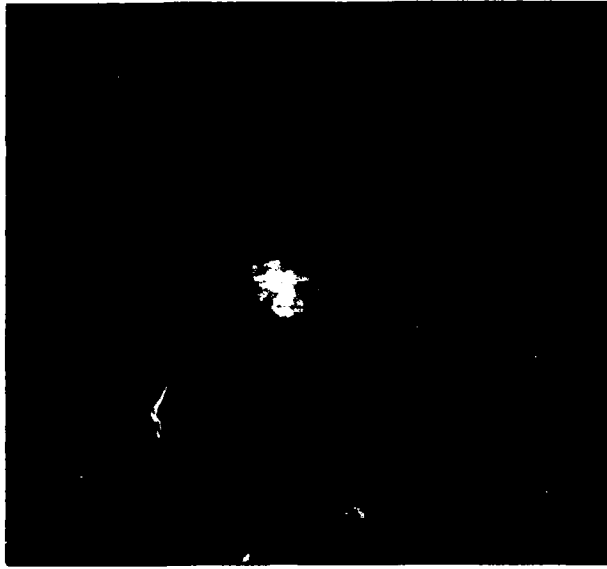
Figure 36. Far-field pattern taken at 50 kV discharge
(Shot number 7202) 7X enlargement.
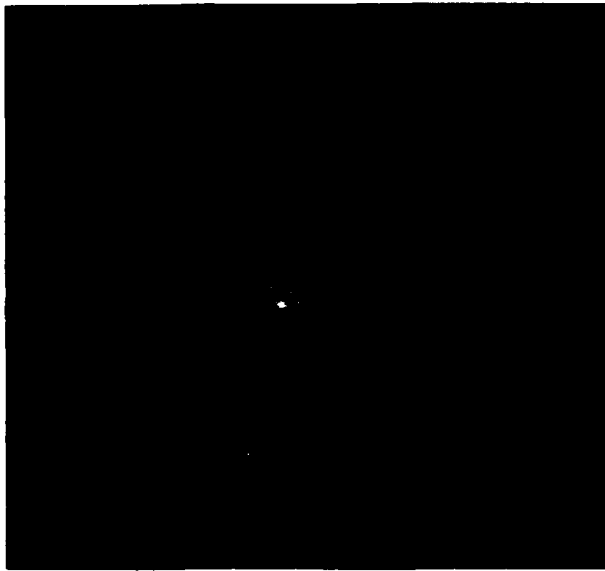
Figure 37. Far-field pattern taken at 50 kV discharge
(Shot number 7201) 7X enlargement.
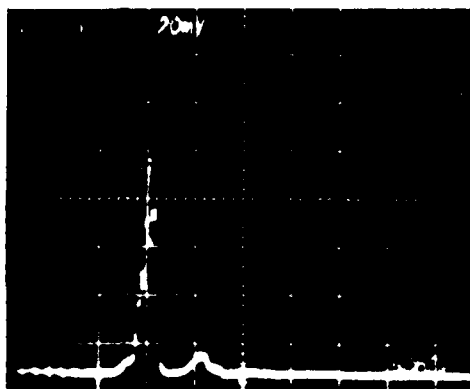
Figure 38.   Temporal response of clipped pulse at 40.8 kV
             discharge (Shot number 7207).
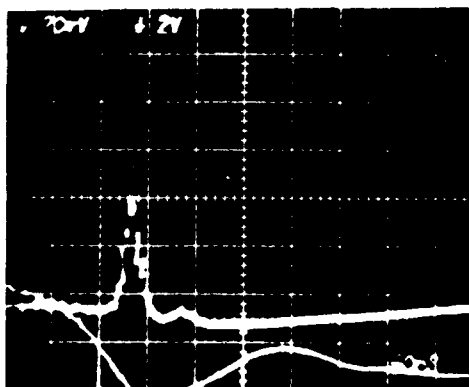
Figure 39.   Temporal response of clipped pulse at 47.8 kV
             discharge (Shot number 7197).
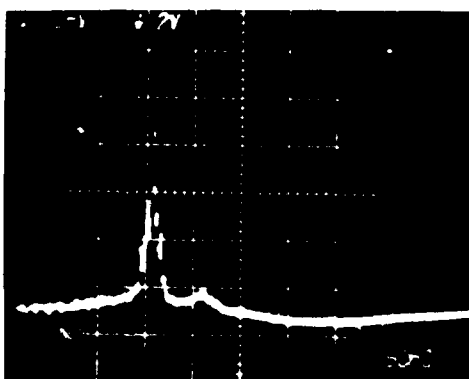
Figure 40.   Temporal response of clipped pulse at 50 kV
             discharge (Shot number 7201).
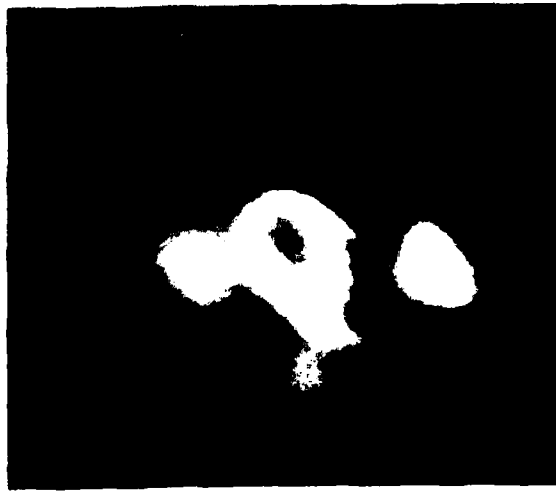
Figure 41. Long pulse burn pattern from laser at 50 kV
discharge (Shot number 7201).

The burn pattern at this position, except for overall fluence, is independent
of discharge voltage occurring well after the mode formation time predicted
by Anan'ev [5].

The temporal response of the long pulse burn compared to the e-beam
pulse is shown in Figure 42 for a discharge voltage of 47.8 kV. The long pulse
trace has been electronically shifted back 600 ns. as compared to the e-beam
initiation in order to observe the characteristics of the total pulse.
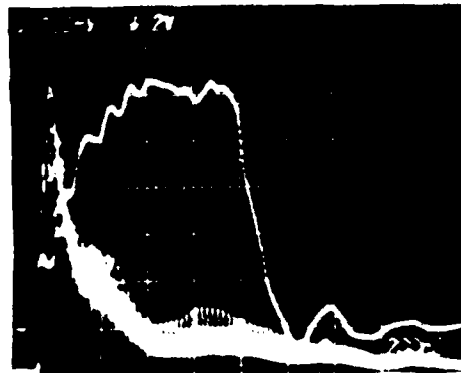
Figure 42. Long pulse burn temporal response (lower trace)
and E-beam current (upper trace).

In order that a comparison may be made to the long pulse burn of Figure 41,
an ideal steady-state calculation of relative fluence (Joules/cm^2) contours
has been made, and is shown in Figure 43. This is a good approximation to the
Fraunhofer pattern at the focus of the laser at 136 meters and is the pattern
resulting from a constant phase, constant amplitude "top hat" distribution
across the laser geometrical aperture. The L-shaped beam from the laser for
these experiments--a result of complete decentering of the feedback mirror
(Figure 4)--gives a far-field burn (Figure 41) which is notable different in
shape compared to the centered burn pattern (Figure 7) for this resonator. The
decentered configuration was chosen for two reasons: the increase of Fresnel
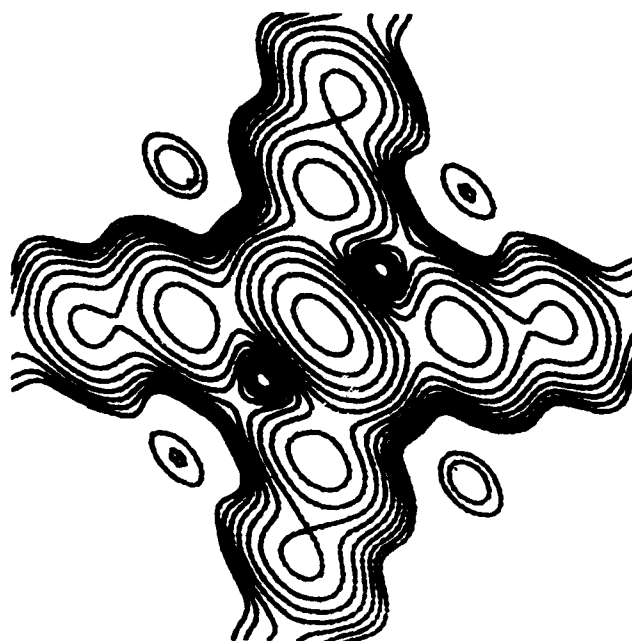
Figure 43. Ideal far-field pattern at 136 meters.

number to increase mode formation time and the ease of preparation of a spatial filtering mask, which for the decentered resonator is an L-shaped aperture. The relative fluence contours in Figure 43 are adjusted logarithmically at five per decade (1.58 X per contour). This is done to give a realistic comparison to the nonlinear burns of Figures 26 through 37 and Figure 41.

Calorimetry calibrations were attempted at P_1 and P_5 and in the laser near-field using the Scientech 364 Joulemeter (see Figure 25). This meter measures the temperature rise of a low reflectance thermopile, causing a change of voltage output that is interpreted as energy. The energy collected at P_4 was 0.1 Joules--typical number for the burn patterns fo Figures 26 through 37, which have been enlarged seven times in the photographs. The energy was collected over twice the burn dimensions as shown on the photographs.

By comparison, a similar collection of energy without the plastic attenuator at P_1 was approximately 26 Joules. With the plastic attenuator in place this would have been 6-8 Joules. Figure 41, which was taken at P_1 has about the same depth of burn as Figure 26, which was taken at P_4, and resulted in the same recorded fluence. Taking into account the 15% reflection per side of the zinc selenide beamsplitter, the 10:1 beamsplitter near P_4, and the 7X demagnification of the burn at P_4; P_4 should have an energy reading based on 8

joules at P_1 of: $8\left(\dfrac{.135}{.210}\right)\left(\dfrac{1}{49}\right)$ Joules equals 0.1 Joules, which was measured at P_4. The Type 52 Polaroid sheets used to obtain the burn patterns in Figures 26 through 37 and Figure 41 had a minimum sensitivity of approximately 0.15 Joules/cm^2 fluence. The fluence for Figures 26 through 37 is approximately the same as that of Figure 41, as expected.

41

The basic conclusions which may be drawn from mode formation experiments in this CO_2 laser are [49]:

(1) Far-field burn patterns taken at 1,000 and 520 nsec are relatively sharp with easily seen first order maxima. Burns taken at 520, 460, 440 nsec show a successive increase in loss of resolution and blurring. This can be attributed to mode formation dynamics.

(2) This pulsed CO_2 laser, with low magnification, unstable resonator optics in a decentered configuration, had a steady state transverse mode formed at a time approximately equal to that predicted by the Anan'ev formula (Equation 1.2).

(3) A steady-state symmetric transverse mode is always formed after the predicted mode formation time. No competing mode of similar losses was found to exist.

D. XeF Laser Experiments

The xenon fluoride laser appeared to be very useful for mode formation work. The initial spontaneous emission was much higher than CO_2 because of the fourth power dependence on wavelength – a factor of 10^6 increase in initial intensity. With a similar average gain profile the XeF laser would produce high peak power, "turn on", at essentially half the number of round trips required of the CO_2 laser used in this work. Assuming good beam quality, the properties of the mode formation should therefore be readily observed early in the mode formation process. This ideal approach was notably modified by experimental problems as described in a later section.

A schematic of the laser used is shown in Figure 10. The laser output aperture is 10 x 20 cm with confocal resonator optics of separation L equal to 262 cm. The gain length is 200 cm. No discharge voltage is used in the XeF laser; however, a pair of Helmholtz coils surround the cavity to supply an e-beam guide field. The e-beam voltage is considerably higher than the typical 180 kV gun voltage of the CO_2 laser, normally running at 280 – 500 kV and acting as the sole pump mechanism of the XeF device. The e-beam current through the foil into the cavity is 8 amps/cm^2 current density.

1. Gain Measurements

Before installing the confocal resonator cavity optics on the laser, a series of gain measurements was made by determination of an I/I_o signal with a short XeF pulse laser (20 nsec FWHM) as a function of high energy pump condition (sidelight fluorescence). The sidelight fluorescence was a measure of the transverse spontaneous emission of XeF at 0.3532 μ, thus giving a direct reference marker of small signal gain in the laser. Figure 44 represents a moderate number of shots from the short pulse excimer laser for 2 meter (high energy) laser pumping. The single pass I/I_o signal from the small laser is plotted against fluorescence signal from the 2 meter laser. This figure illustrates the point that threshold gain is reached essentially at the moment of sidelight fluorescence detection for the M = 1.32 magnification
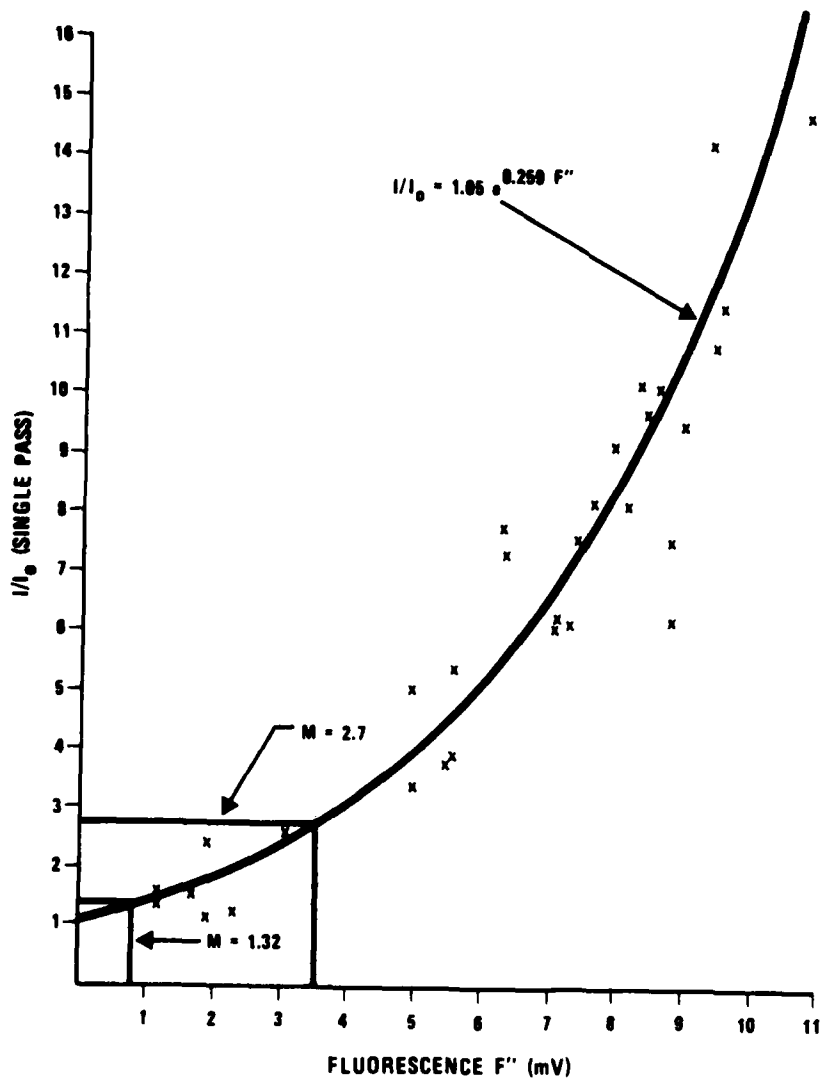
Figure 44. Single pass I/I_o versus fluorescence signal fluorescence values for threshold gain are shown on the curve for M = 1.32 and M = 2.7 resonators.

resonator optics (0.8 mV) and a short time after this value for the M = 2.7 resonator optics (3.6 mV). The purpose of the gain measurement versus side-light fluorescence is to show that the onset of sidelight fluorescence signifies threshold gain in this laser, within 10 nsec or less for the M = 1.32 resonator, and no more than 30 nsec for the M = 2.7 resonator. This may be seen from Figure 45 which is an oscilloscope trace of sidelight fluorescence with the resonator mirrors in place and extraction of high peak power (loaded cavity) as a function of time. To determine emission of high peak power relative to fluorescence (threshold gain), the temporal profiles of these curves were electronically summed at the oscilloscope.

43
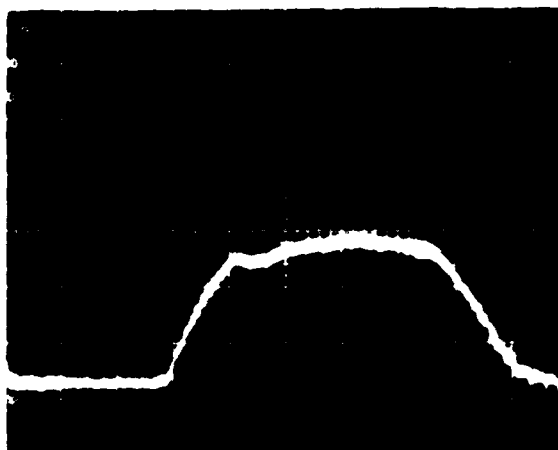
Figure 45. Sidelight fluorescence output.
(Vertical Scale 5 mV/div., horizontal
scale 100 nsec/div.).

2. Far-Field Measurements

Figure 46 is a schematic of the test configuration for XeF far-field mode formation experiments. A helium neon alignment laser is positioned such that the beam goes through a 2 mm non-aluminized centered hole in the primary mirror and strikes the secondary (feedback) mirror, which has centered 1 mm reference non-aluminized spot. Centering the helium-neon beam on these holes defines the optic axis of the resonator. The mirrors are aluminized and the He/Ne alignment beam will fill the laser cavity through diffraction. This resonator is then aligned by centering circular interference fringes (formed between successive passes of the laser beam in the resonator) on the feedback mirror. The visible beam should then track the excimer beam and can be used to position the far-field pattern as desired (to within $\sim$ 50 microradians).

Because of external optics size limitations only a vignetted portion of the laser beam was used in far-field mode formation analysis for both the M = 1.32 and M = 2.7 experiments. In the case of the lower magnification resonator, a vertical rectangle of 1.21 cm x 6.5 cm was extracted from the lower side of the beam toward the anode. For the M = 2.7 resonator a small 1.75 cm x 0.34 cm horizontal rectangle, centered 1.87 cm below the feedback mirror, was the extraction aperture. By turning flat mirrors these beams are propagated approximately 29.6 meters into a clean room area to an off-axis parabolic mirror, 10 cm diameter with 123 cm focal length. All mirrors were characterized to $\lambda/10$ or better at 0.3532 microns. The far-field pattern of the off-axis parabolic mirror was then magnified by a 5 cm focal length suprasil lens, which later imaged the pattern at over-exposed developed Polaroid film planes C_1 and C_2. The beam was first attenuated by reflection from a fused silica wedge, with the transmitted portion being absorbed on an unexposed developed Polaroid sheet. The reflected part of the beam was sent from mirror m_1 to a 30/30 chromium beamsplitter which, after suitable reflections from flat mirrors m_2, m_3, and m_4, positioned far-field patterns at c_1 c_2. It was necessary to use the Polaroid sheets as fluorescing screens (exposed Polaroid type 52 sheets) since the gated pulse cameras were insensitive

44

GATED PULSE CAMERAS
5-20 NSEC WINDOWS
50, 100, 200, 500, NSEC DELAYS
3 PICTURES EACH
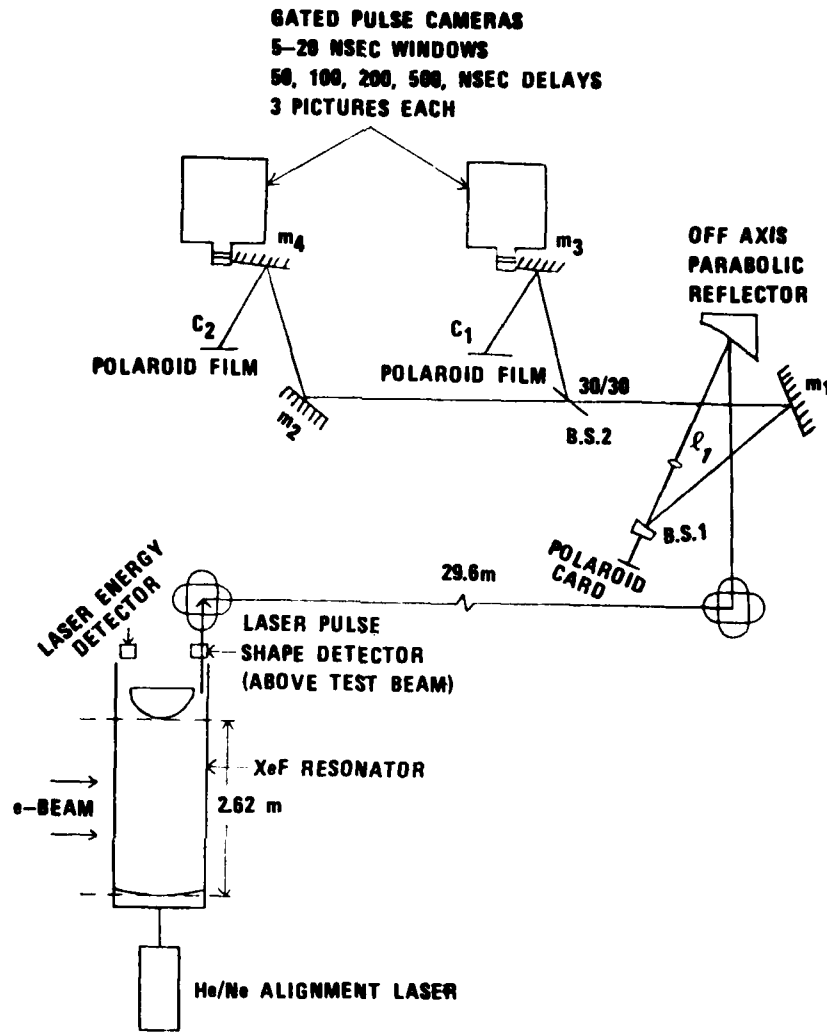
Figure 46. Experimental excimer laser configuration for
mode formation experiments.

to the uv output from the laser (0.3532 microns). The response for the
Polaroid sheets was remarkably rapid. The sheets were checked with a 15 nsec
pulse from the gain measurement XeF laser and no pulse-broadening from
fluorescent relaxation could be detected.

The patterns from the cards at c_1 and c_2 were focused on two high speed
image converter cameras. Both cameras were TRW Model 10 image converter
cameras equipped with three exposure framing heads. Each of these cameras
provide three pictures with arbitrary exposure times of 5, 10, or 20 nano-
seconds and arbitrary interframe times between pictures of 50, 100, 200, and
500 nsec. The five nanosecond exposure time was used in all of the frames
taken in this experiment. This was done to minimize the far-field pattern
change as a function of mode formation. One of the fluorescing cards was also
viewed by a S-5 vacuum photodiode (ITT 4018) to monitor laser pulse length

45

(not shown in Figure 46). Timing reference gates from the framing cameras were electronically added to the photodiode output to establish frame timing with respect to the laser pulse. At the laser end, vacuum photodiodes recorded laser energy as well as cavity sidelight fluorescence.

3. The Real Versus the Ideal

Three serious problems were encountered during these tests: gas life, mirror damage, and beam steering. The last two, in particular, tended to degrade the quality of the experiments.

Gas life, the number of laser pulses with a useful output/gas fill, was a problem with the stainless steel laser chamber, but was especially bad at the beginning of these experiments. A previous experiment with this laser had utilized XeCl in Raman conversion. Since we had little experience with the effects of residual chlorine on the XeF mix, the mode formation study was begun with only a perfunctory cleaning of the laser chamber. It soon became obvious that this was a mistake, as we were getting only one of two useful shots per laser fill as compared with a normal six to ten shots. This problem was cured by a total disassembly and thorough cleaning of all laser chamber parts.

The second, and more serious, problem was beam steering. The steering requirements were far higher than had ever been demanded of this system. The initial scheme called for the extraction of portion of the laser beam $\sim$ 1.21 x 6.5 cm, steering this to the off-axis parabola, focusing to a far-field pattern, and magnifying this pattern so that the central five diffraction angles filled the 10 cm field of view of the framing cameras. The focal length of the parabola was 123.2 cm, thus

$$\frac{5f\lambda}{d} = \frac{5(1.232) \ (3.53.2 \times 10^{-9})}{0.0121} = 1.8 \times 10^{-4} \text{m} \qquad (2.9)$$

where f is the parabolic focal length and d, the slit width.

This was equated to the camera image size

$$1.8 \times 10^{-4} \text{ M} = 4 \ (0.0254) \qquad (2.10)$$

thus

$$M = 567. \qquad (2.11)$$

With this system, the central lobe position could vary by about $\frac{1.5f\lambda}{d}$ and still be in the field of view of the camera. This required the laser beam steering to be repeatable to about 44 microradians. The initial tests mentioned above showed that the steering did not meet this requirement. A set of burns was taken behind the lens at a magnification of 15 which showed the beam on a shot-to-shot basis to be confined to an area about two inches in diameter. This implied a focal point movement of about 3 mm, for a steering accuracy of only 2.4 milliradians. This gross variation was not understood since the laser alignment and aiming method was felt to be far better than the test indicated. The procedure utilized a helium-neon laser on the laser

46

optical axis which was transmitted through the entire system to aim the laser. The resonator was aligned by interferometrically overlaying the He-Ne return spot from the primary and secondary. At this point, the laser was being dis-assembled for cleaning, so it was decided that the mirrors should be aluminized to allow the He-Ne beam to fill the mode volume by diffraction, and to use the resultant Ne-Ne beam to aim the laser. Unfortunately the chlorine in the laser chamber had already reacted with the dielectric coatings on the mirrors, and when cleaned, large portions of their surfaces showed damage. Due to a lack of time (stripping and refiguring would take several weeks), it was decided to proceed with the aluminizing. The M = 2.7 optics were aluminized at the same time. The resulting mirrors did not look good, but appeared to work well enough for the experiment.

With the aluminized mirrors, we could be much more confident in our alignment and aiming procedures. The aiming problem was not eliminated, and it was determined that the problem was due to a combination of the large secondary mirror mass and the electron beam magnetic guide field of the laser. When the laser is fired, the guide field coils are turned on about 0.6 seconds before the electron gun. The mechanical shock to the system was exciting a resonance in the secondary mirror mounting assembly so that the mirror vibrated for about three seconds after guide field initiation. This was observed by watching the He-Ne spot in the clean room and firing the coils by themselves. The problem was essentially cured by leaving the coils on for $3\frac{1}{2}$ seconds before firing the laser. This reduced the steering error to that resulting from the settling of the secondary mirror. The system could be aimed with an accuracy of about 380 microradians. In later experiments with the M = 2.7 resonator, the mirror resonance with the magnetic field shocks all but disappeared, and an aiming accuracy of better than 100 microradians was achieved with the former magnetic field e-beam delay of 0.6 seconds. The 380 μ-rad steering accuracy was not sufficient enough for the experimental design goal, so the image magnification was reduced to about 60 at the fluo-rescing cards to ensure obtaining the far-field pattern at that point.

4. Test Results

(a) M = 1.32 Resonator

Because of the degraded mirror quality, the far-field patterns taken by the image converter cameras were not diffraction limited. The spot sizes were, at best, about five times the diffraction limited central spot size. Even with this restriction, mode formation can easily be seen in Figure 47, which relates mode formation time to XeF far-field burn patterns. This figure shows the time resolved data from shot number 3/5-2. The upper photo is the fluorescence/laser output overlay. The center photo is the photodiode signal in the test room overlaid by the framing camera timing markers, and the bottom two photos are the framing camera pictures of the mode evolution. The center trace determined laser threshold relative to emission of high peak power seen by the negative photodiode signal with positive-going framing camera gate signals. The lower photographs were taken at image planes c_1 and c_2 by the image converter cameras. Frames 1 through 3 show images which were "pinching down," implying the mode had not yet formed. Frames 4 through 6 were essentially identical; a quasi-steady-state mode had formed. From these data it is apparent that the mode developed between Frames 3 and 4, for a mode formation time of between 320 and 430 nsec. A

47
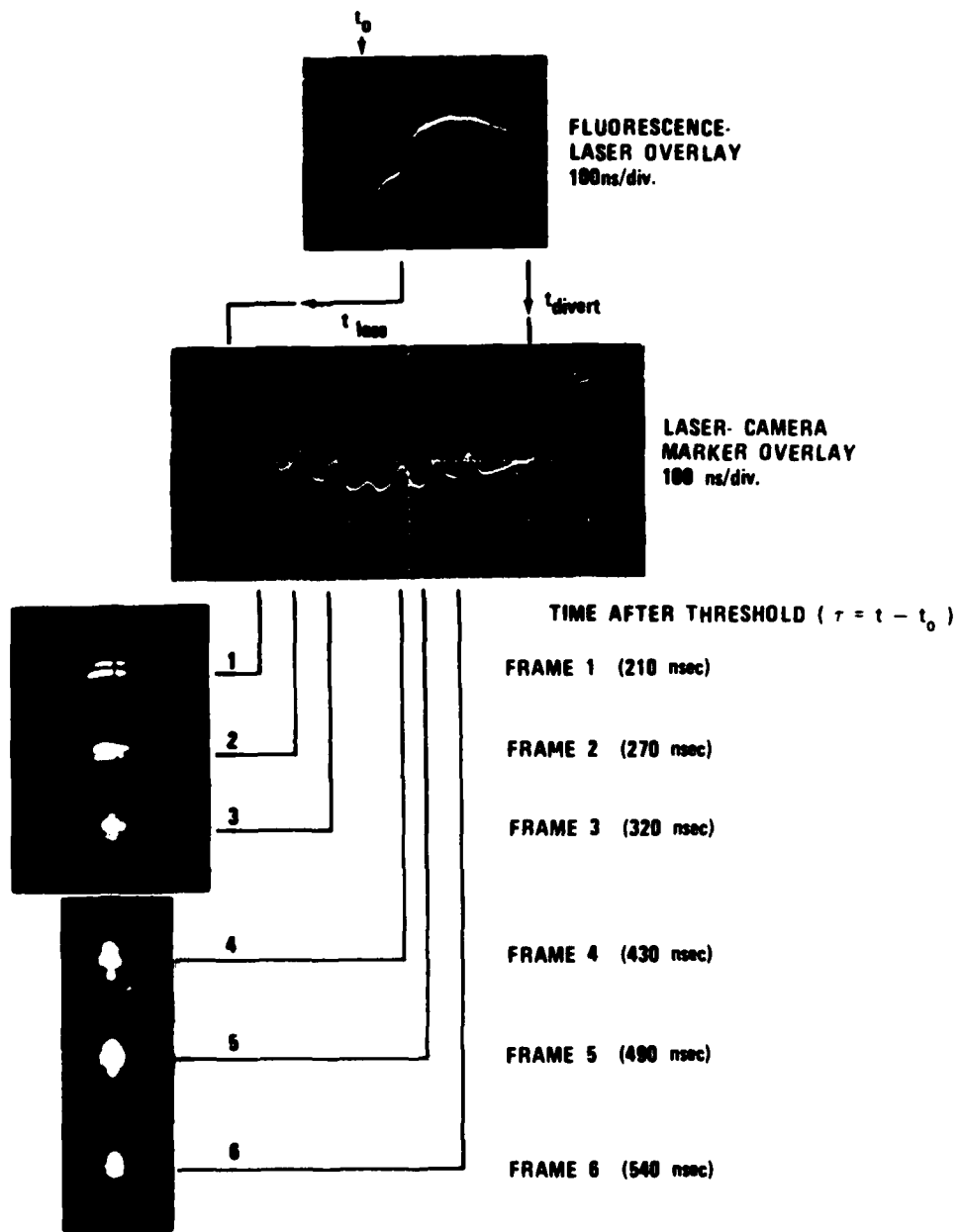
Figure 47. Mode formation time for the M = 1.32 resonator
(Shot Number 3/5-2).

separate run showing convergence of the mode along the lines of Figure 47 is shown in Figure 48. In this case mode formation occurred between 360 and 470 nsec. In both these figures t_o is threshold, t_{lase} is the onset of high peak power, and t_{divert} is the crowbaring of the e-gun, ending the laser pulse. The far-field pattern in Frames 4, 5, and 6 is a blurred area with a maximum of 5X diffraction limited dimension and is representative of the quasi-steady-state transverse mode.

FLUORESCENCE–
LASER OVERLAY
100 nsec/div.

LASER–CAMERA
MARKER OVERLAY
100 nsec/div.

TIME AFTER THRESHOLD ($\tau = t - t_o$)

FRAME 1 (250 nsec)

FRAME 2 (310 nsec)

FRAME 3 (360 nsec)

FRAME 4 (470 nsec)

FRAME 5 (530 nsec)

FRAME 6 (580 nsec)
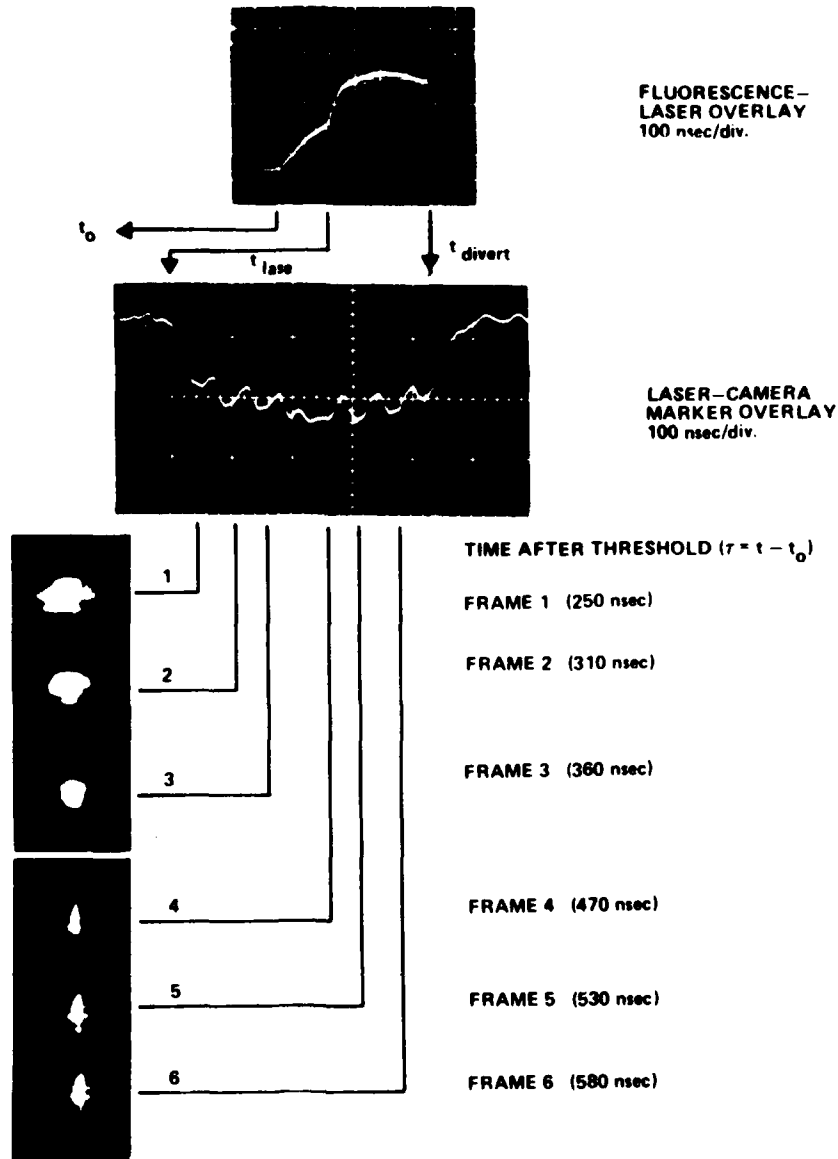
Figure 48. Mode formation time for the M = 1.32 resonator (Shot Number 3/5-1).

49

Figure 49 is a summary of all mode formation runs taken with the M = 1.32 resonator from the vignetted aperture of 1.21 x 6.5 cm. A range of time for mode formation is shown rather than a specific time. This is the result of: (1) poor mirror quality and/or the XeF active medium (since the far-field spot size was at least five times the central lobe size of a diffraction limited beam); (2) poor resolution of the framing cameras and shadowing of images by the image converter tube grid wires (these cameras represent a twenty year old technology); and (3) differences between the cameras in sensitivity and actual appearance. Some of the runs in Figure 49 are open ended--the e-beam may have crowbarred too soon, the framing intervals may have been too widely spaced, or the framing intervals may have been incorrectly timed, giving only a lower or upper bound for far-field pattern stabilization. The runs were divided almost equally between a mixture of 1:3:760 NF_3:Xe:Ar at two atmospheres and 1:3:1140 NF_3:Xe:Ne at three atmospheres. Neon diluent appeared to provide a better beam quality. It is interesting to note that the experimental data show the mode to have formed around 350 nsec--considerably less than the Anan'ev time of 513 nsec. This anomaly is explained in detail later in this work.

(b) M = 2.7 Resonator

Experiments using this resonator were performed in a manner similar to those using the M = 1.32 resonator. The resonator optics used in this test series were in better condition than the M = 1.32 optics and gave a somewhat better far-field pattern. The short mode formation time for this configuration (168 nsec) required working at the practical limit of the laser; i.e., four atmosphere cavity pressure and maximum laser gas pumping. The results were the same for this laser as the upper limit of the CO_2 experiments. The foil separating the laser and the e-gun chambers was punctured by arcing after a few runs.

The portion of the beam used for these tests was a 0.34 cm by 1.75 cm rectangle located below the feedback mirror. The far-field pattern size was increased along the dimension of interest by $\frac{1.21}{.34}$ = 3.6x compared to the M = 1.32 pattern. Figure 46 shows the test schematic. To compensate for the lower transmitted energy, the Suprasil wedge (B.S.1) was replaced with a dielectric coated total reflector. A typical run sequence for this resonator is shown in Figure 50, which is a counterpart of Figures 47 through 48 for the M = 1.32 case. The first frame is not resolved because of the low intensity from the laser pulse. It appears that mode formation occurred in this run between 130 and 170 nanoseconds.

The accumulated data for the M = 2.7 resonator are shown in Figure 51. A problem of a dim first frame applies to all runs from shot numbers 4/17-2 through 4/17-5. Again, as with the M = 1.32 data, these data show an anomalous early mode formation of time of 140 nsec as compared to the typical theoretical result of 168 nsec. Data were taken with NF_3:Xe:Ar 1:3:760 at two atmospheres and NF_3XE:Ne 1:3:1520 at four atmospheres.
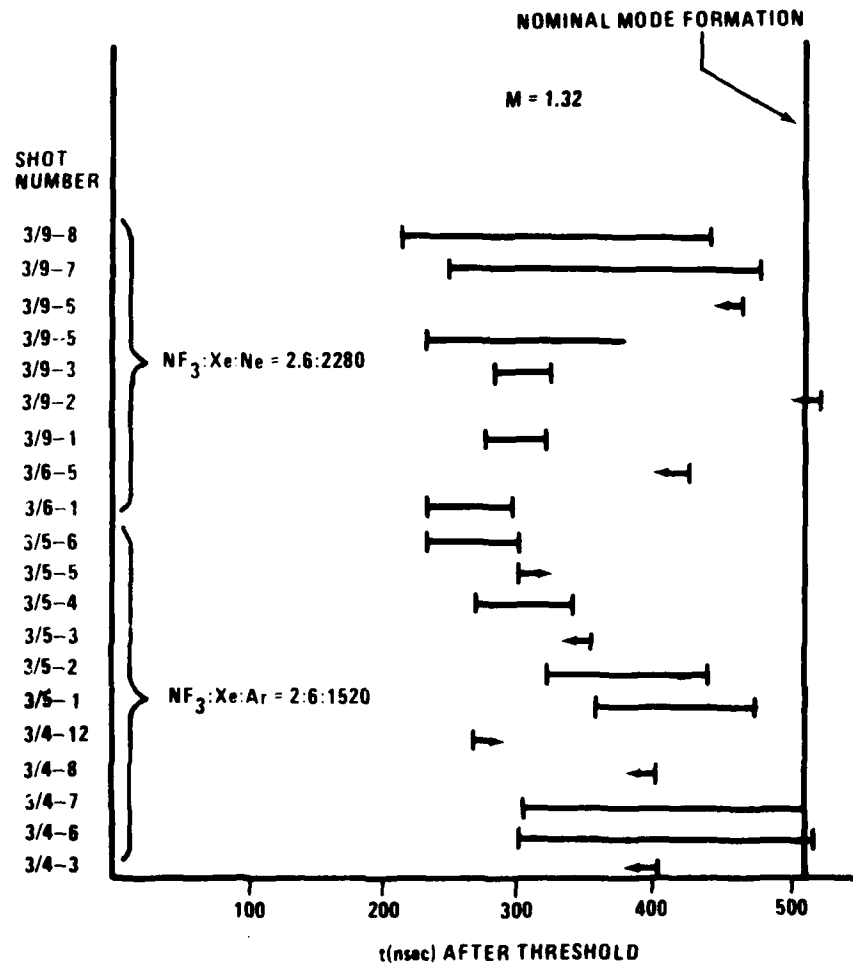
Figure 49. Mode formation in the M = 1.32 resonator.

FLUORESCENCE-
LASER SIGNAL
100 ns./div.

t_o t_{lase} t_{divert}

LASER–MARKER
SIGNAL
100 ns./div.

FRAME 1
t_o + 130 nsec

FRAME 2
t_o + 170 nsec

FRAME 3
t_o + 250 nsec

FRAME 5
t_o + 375 nsec

FRAME 4
t_o + 310 nsec

FRAME 6
t_o + 440 nsec
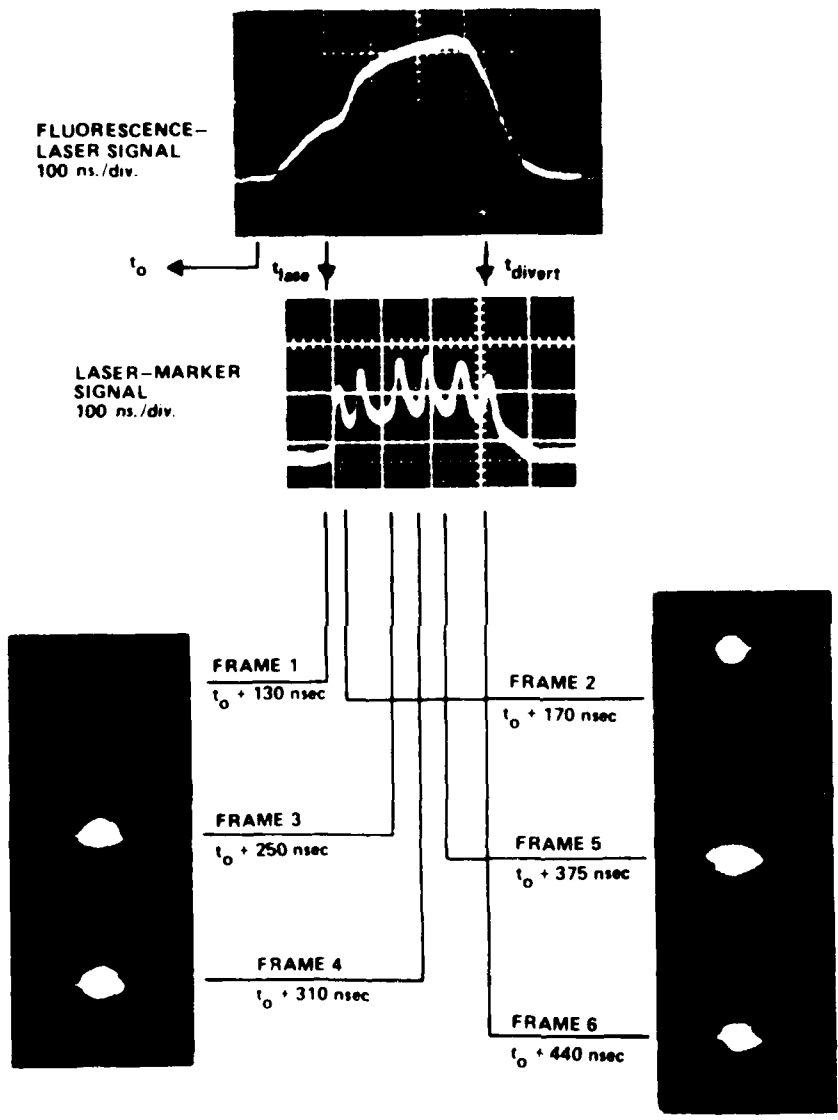
Figure 50.   Mode formation time for the M = 2.7 resonator
(Shot Number 4/17-3).
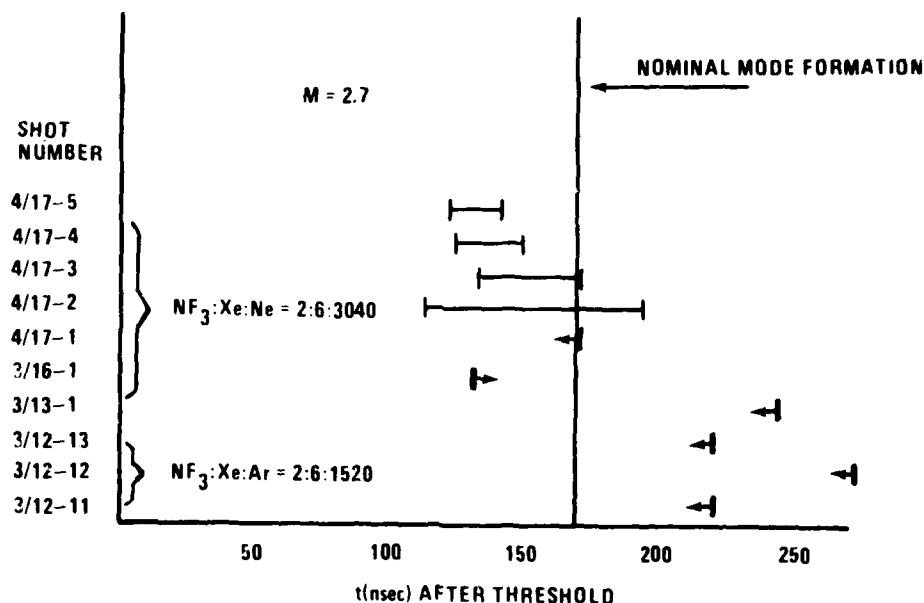
Figure 51. Mode formation in the M = 2.7 resonator.

A summary of the results of the XeF experiments and initial modeling
results were presented at the Annual Meeting of the Optical Society of America,
at Tucson, Arizona in 1982 [50]. These results will be submitted for publi-
cation at a later date [51].

5. Concluding Remarks on the XeF Laser Experiments

The excimer laser was anticipated to be of great use in the
verification of the formulas of Zemskov and Anan'ev for transverse mode
formation time in unstable resonators of moderate magnification (1.32 < M < 2.7).
This was primarily because of short time laser "turn on," i.e., high peak
power was normally achieved well within the Anan'ev time with a resonator
magnification, M of 1.32 and certainly somewhat within the time for the higher
magnification of 2.7. Therefore, the far-field patterns of such a laser could
be readily examined both before and beyond the predicted mode formation time.

Various experimental limitations did not permit a "fine tuned"
definition of mode formation. An ideal limit would have produced a central
lobe of the far-field pattern rise to within 90 percent of its peak value, and
the central lobe position to within 10 percent of the nominal angular steady-
state value; as would have been desired to validate an Anan'ev criterion. A
much coarser stability definition came from these experiments. This stability
was determined as variations observed from a nominal blur circle five times
the diffraction limited central maximum arising from a severely vignetted laser
aperture. The anomalous shortening of mode formation time will be justified
in Chapter III with the experimental constraints applied at this juncture.

Saturable gain was suspected to contribute to a large degree in the
observed early mode formation. The excimer laser quickly achieved saturation

at approximately 150 nsec. Calculations of saturable gain for this laser
(in Section III) tend to support the hypothesis of early mode formation.

The early mode formation time has been substantially confirmed for the
XeF laser case, taking into account the experimental limitations of the ex-
periment described above as well as modeling results. A series of experiments
currently being formed at Maxwell Laboratories at San Diego, where these
initial results were taken, may confirm this general assumption [52].

III. THEORETICAL MODELING

A. Introduction

A strip resonator called CAV2D (see Appendixes) has been used to
model mode formation dynamics [53]. This has been developed from a Fourier
transform code, the SOQ code of Siegman and Sziklas [54], which is used to
determine the lowest loss steady state transverse mode in unstable resonators.
The code can model external vignetting and saturable resonator gain using the
Rigrod equations [55,56] in an infinitely thin slice near the primary mirror.
A fast Fourier transform (FFT) subroutine [57] has been incorporated as a
considerable time saving measure for the large Fresnel number cases in cal-
culations of the direct and inverse Fourier transforms. As an example, con-
sider a typical run in this work for an XeF laser with a tube Fresnel number
$\approx$ 2700. 16,384 mesh points, m, were used in the calculation. A typical
calculating time using the FFT algorithm is proportional to $m \log_2 m$ rather
than m^2 for the usual methods of propagation: the direct solution of the
wave equation, the Huygens–Fresnel integral equation [58], or the Fourier
transform solution. The time saved is enormous for large Fresnel number
applications, e.g., the ratio of calculating time is

$$\frac{m^2}{m \log_2 m} = \frac{(16,384)^2}{16,384 \log_2 (16,384)} = 1170 \quad . \tag{3.1}$$

Considering a typical time of 300 seconds for one using the FFT, the run
by alternative computational approaches would be 10 hours. In addition, an
expanding coordinate system useful for the unstable resonator geometry is
included [59].

CAV2D is a Fortran program which calculates the transverse modes of
unstable resonators for lasers. It performs wave–optics calculations for the
propagation of a beam back and forth between the two mirrors of the resonator
until it obtains a transverse distribution of the complex optical amplitude
which is self-consistent, i.e., which repeats itself over a round trip to
within a complex multiplicative constant. The outcoupling of a strip resona-
tor equals unity minus the square of the absolute value of the multiplicative
constant (eigenvalue). This is the obvious purpose of the code for steady-
state calculations in unstable resonators.

Typically, a starting wave which has uniform intensity and has a phase
distribution equivalent to a collimated output beam is launched. This wave is
assumed to have just been reflected from the convex mirror. The starting
wave may be of a different form without affecting the final steady-state
result. One possibility would be a wave of constant intensity with randomized

54

phase distribution, though this choice would ordinarily require more itera-
tions to achieve a solution than would the uniform phase choice. The iterative
method can be justified merely as a numerical means of obtaining a solution
of the lowest-loss mode, without any reference to modeling of the actual
temporal progression of the course of events.

Successive propagation back and forth between mirrors is the physical
nature of the action of a resonator. Hence, the CAV2D code in this work is
extended to model the transverse mode formation process in which randomized
radiation from spontaneous emission develops into a well-formed transverse
mode. The code extensions involve introducing randomness into the initial
phase distribution, calculating the far-field distribution after each round
trip, saving tables of values of I/I_o and the directional orientation of the
point of maximum far-field intensity after each round trip, and printing or
punching those tables for further statistical analysis. The principal features
of the code are unchanged from those sed to obtain steady-state mode
distributions.

The code specifically treats strip, or cylindrical-mirror, resonators.
The limitation of one transverse dimension is not as restrictive as it may at
first seem. Resonators with square or rectangular cross-sections have the
property that the mode distribution for an empty cavity (equivalent to an
unsaturated uniform gain situation) may be factored into a product of a strip
resonator mode on each of the two transverse dimensions. When saturated gain
plays a significant role, or when the symmetry is broken (for example by a hole
in a mirror), the factoring is no longer valid. A separate, but somewhat
similar, computer program called CAV3D has been prepared and used for the
cases in which there is a hole in the concave mirror. This code, which takes
into account two transverse dimensions, is capable of handling Fresnel number
cases in the realm of CO_2 resonators ($N_T < 100$) but is certainly not valid in
the regime of excimer lasers ($2700 < N_T < 11,000$) because of computer memory
limitations. Even one of the largest computers, e.g., the CDC 7600 with the
inclusion of auxiliary "large core" memory (LCM), does not have the capability
of handling 256 x 256 mesh points.

A verification of CAV2D for steady-state transverse modes has been
achieved by comparison with the results of other workers using an entirely
different methodology. In particular, the asympotic expansion code results of
Horwitz [16, 21] and the work of Chen and Felsen [60] were examined. The
quite appreciable detail which is present in near-field intensity distributions,
readily apparent from the inspection of plots in the Horwitz papers, are
accurately reproduced by the CAV2D code.

The angular distribution of the far-field intensity ($I(\theta)$] is calculated
in CAV2D after each round trip in the resonator by direct numerical evaluation
of the Fraunhofer integral written as

$$I(\theta) = C \left| \int_{-\alpha}^{\alpha} U(x) \exp\left(\frac{i\ 2\pi\theta x}{\lambda}\right) dx \right| \qquad (3.2)$$

where θ is a diffraction angle and C is a normalization constant.

55

Considering one printout per round trip, the bulk of paper generated over one mode formation run requires condensation. The criterion for data selection becomes two independent data points per round trip selected as follows:

(1) the intensity of the highest peak in the far-field distribution is normalized to an intensity for a beam with identical power, uniform near-field intensity and phase across an aperture of width D;

(2) the angular position of the highest peak is normalized to the diffraction angle (λ/D) of the aperture.

The total number of data points depends upon the number of round trips acceptable for convergence of the data to a steady-state condition. Thirty to forty round trips per run appear to be suitable for CO_2 and XeF with M = 1.32. No more than twenty round trips per run are acceptable convergence criterion for XeF with a resonator magnification, M, of 2.7.

B. CO_2 Laser Analytical Modeling

A saturable gain model for the CO_2 experiments has been built into the code based upon CO_2 test parameters. A nominal average gain (0.009/cm) and an assumed initial intensity at threshold intensity relative to saturated intensity, I/I_{sat} of 5×10^{-12} was used. These initial conditions were determined by experimental measurement of average small signal gain during the period of mode formation; and measurement of loaded cavity gain, γ, relative to small signal gain, γ_o, at 21 round trips after threshold in the laser at the approximate mode formation time. The ratio I/I_{sat} can be derived at this time from the ratio of loaded cavity gain to small signal gain

$$\gamma = \frac{\gamma_o}{1 + I/I_{sat}} \tag{3.3}$$

therefore,

$$I/I_{sat} = \frac{\gamma_o}{\gamma} - 1 \tag{3.4}$$

γ_o is obtained from Figure 20 from the small signal intensity at approximately 21 round trips ($I'^\tau \approx 7.5$) and from gain length, ℓ;

$$\gamma_o = \frac{\ell n \ (I/I_o)}{\ell} = 0.02 \ cm \tag{3.5}$$

γ is derived from the average increase in intensity of one round trip during the gain switched spike leading edge at approximately 21 round trips ($I'/I_o' \approx 3.5$), as seen in Figure 23, so that

56

$$\gamma = \frac{\ln (I'/I_o')}{2\ell} = 0.0063/cm \quad . \tag{3.6}$$

Therefore, using Equations (3.4), (3.5), and (3.6), we have

$$I/I_{sat} = 2.2 \tag{3.7}$$

which determines the degree of saturation in the actual lasing process for a specific number of round trips. This information specifies the initial conditions of the analytical code saturable gain inputs for the CO_2 laser cases.

Figure 52 shows one selected run for the CO_2 case with saturable gain included. One value of relative normalized intensity, I/I_o, and angular position of maximum peak in terms of relative diffraction angle $D\theta/\lambda$ is shown for each round trip. Thirty round trips are shown in the figure. The nominal convergence of the graphs is around the mode formation time as predicted by Anan'ev for 22 round trips. The data presented in Figure 52, when combined with 19 other runs, give cumulative statistical results on mode formation in the CO_2 laser with saturable gain conditions as shown on later figures as normalized to a mode formation time of 20 round trips.

The convergence of the far-field distribution as a function of round trip number is typically shown by Figures 53 through 62. Again, each round trip peak intensity has been normalized to unity from a laser aperture of dimensions, D, plotted on a scale of $\pm \frac{5\lambda}{D}$ where λ is the laser wavelength.

A random phase wavefront was launched with initial conditions similar to those of Figure 52: I/I_{sat} at threshold is 5×10^{-12} and average small signal gain, λ_o, is 0.9%/cm. The variation of the far-field shape and position is shown in the series of figures to converge to the steady-state far-field shape and position is shown in the series of figures to converge to the steady-state and far-field pattern (Figure 62).

The compilation of 20 runs with differing values of random phase but with the same initial conditions as that of Figure 52 is shown in Figures 63 and 64 for the relative intensity of the highest peak, I/I_o, and the relative diffraction angle, $\frac{\theta D}{\lambda}$, of the highest peak, respectively. These are shown statistically with the mean (M) and one standard deviation (S) for each round trip. These tend to converge to the typical relative Anan'ev number (Equation 1.1) of 20 round trips (22 round trips in reality). A line is drawn across the statistical compilations which represents the mode formation round trip number as determined from the Anan'ev formula (Equation 1.1). This represents a baseline for mode formation and is referred to as the "nominal mode formation" in all figures of this type. The effect of gain introduced in these calculations seems to produce a change in apparent mode formation time. This may be seen from a single run comparison, for example, of Figure 65 and Figure 52. In Figure 65, the wavefront is launched with the same initial
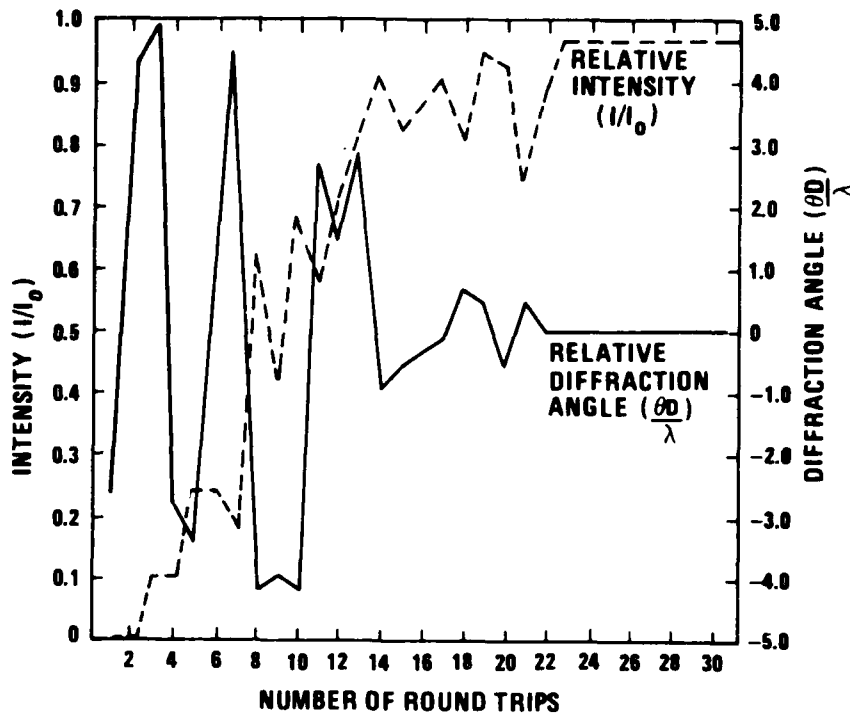
Figure 52. One mode formation run with gain for normalized
intensity and diffraction angle. Mode formation
is predicted at 22 round trips, M = 1.32, N_T = 279.
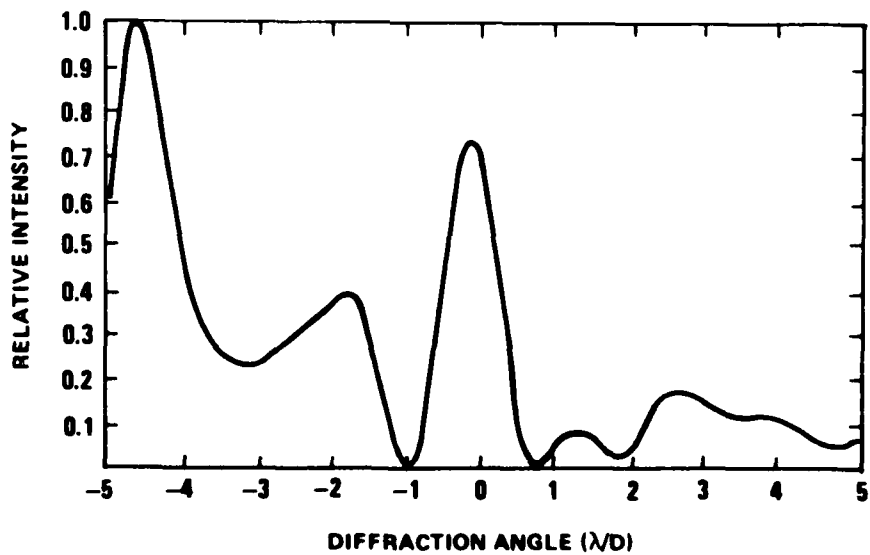
Figure 53. Far-field pattern at 1 round trip.
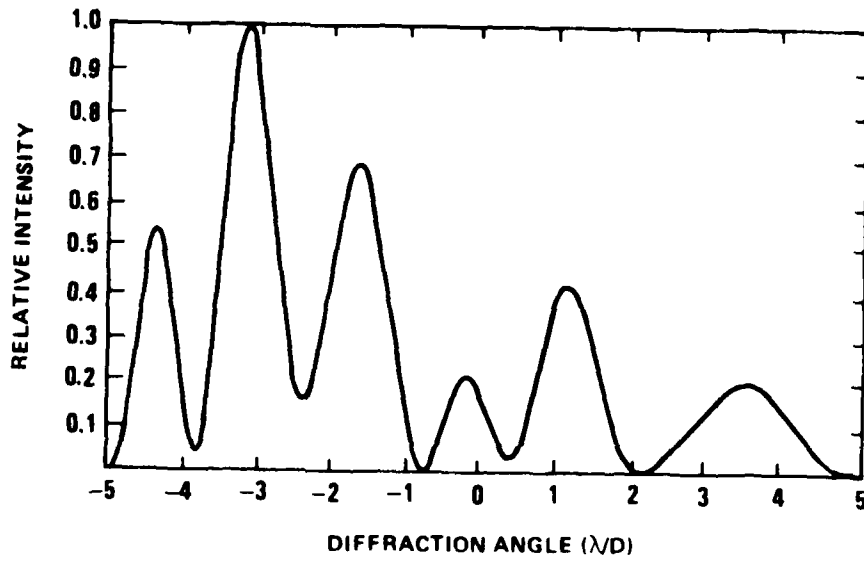
Figure 54. Far-field pattern at 2 round trips.
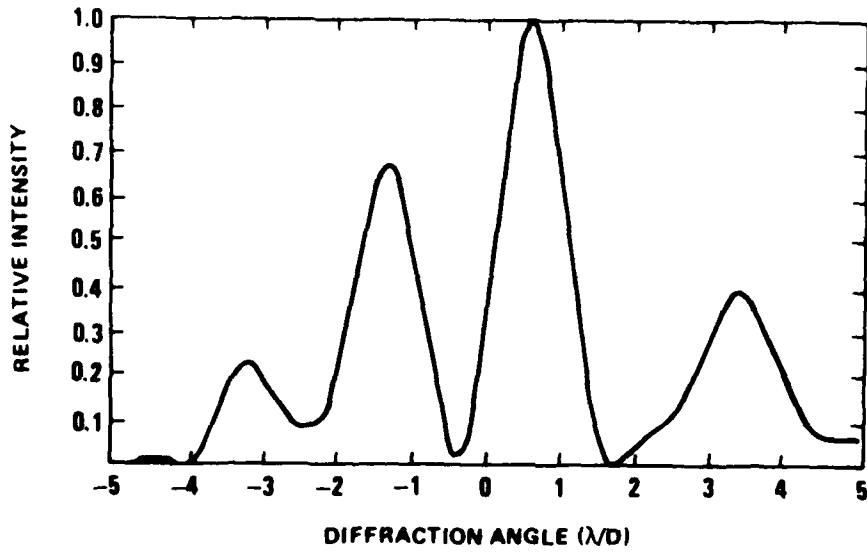
Figure 55. Far-field pattern at 3 round trips.
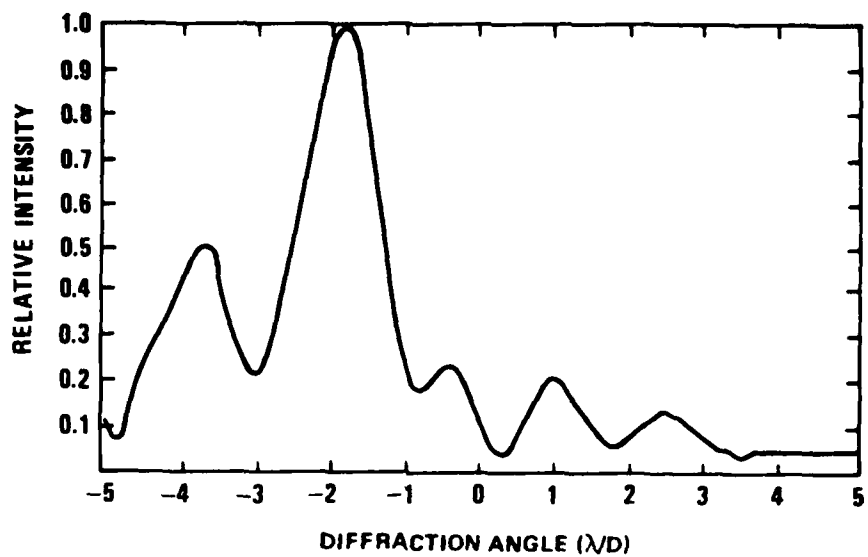
Figure 56. Far-field pattern at 4 round trips.
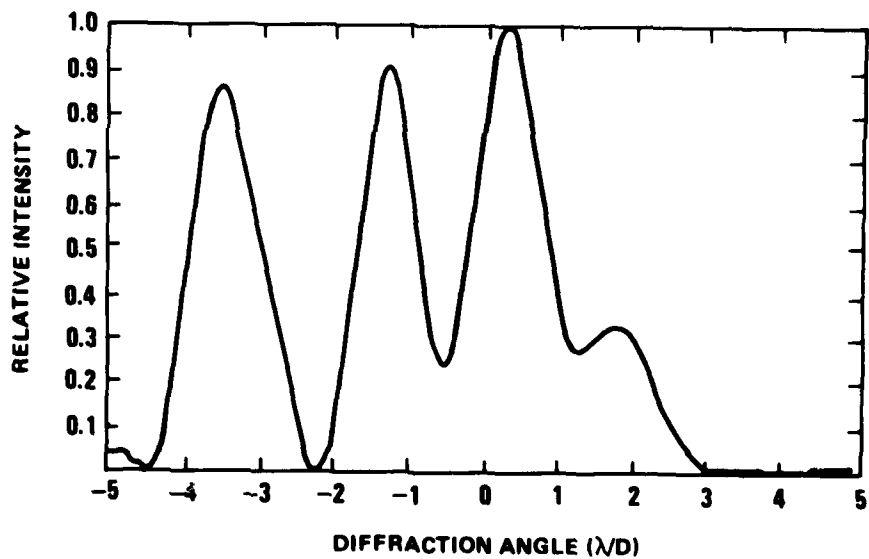
Figure 57. Far-field pattern at 6 round trips.

60
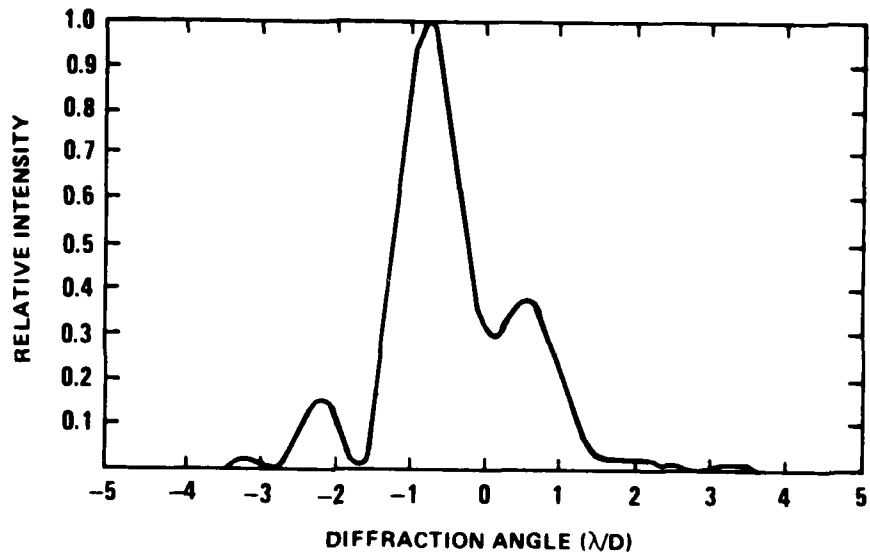
Figure 58. Far-field pattern at 8 round trips.
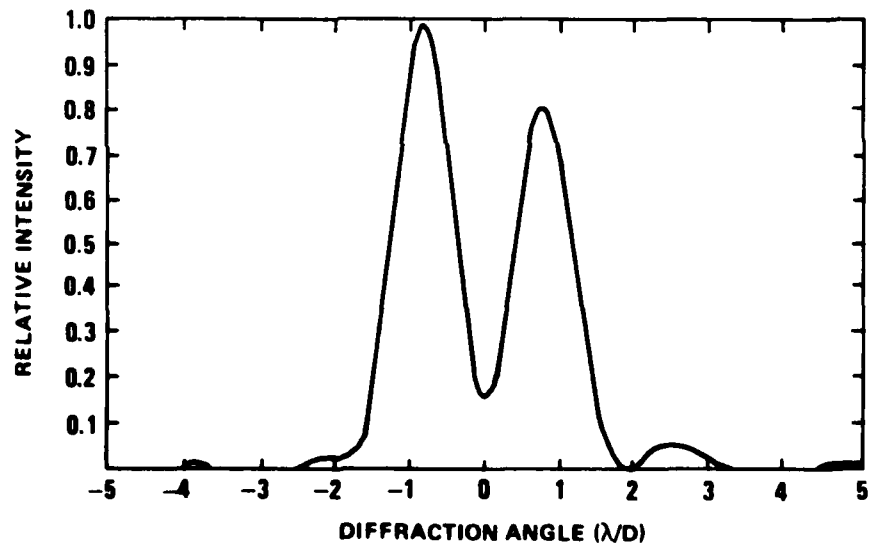
Figure 59. Far-field pattern at 9 round trips.
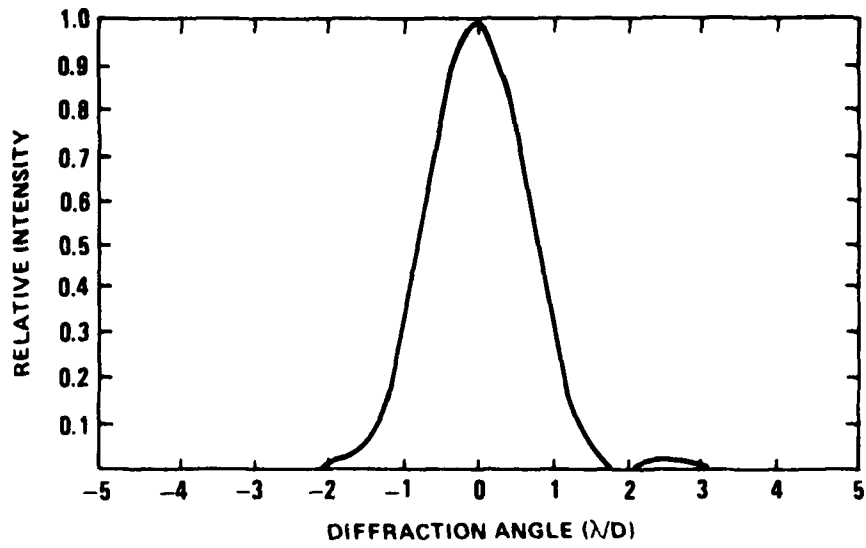
Figure 60.   Far-field pattern at 11 round trips.
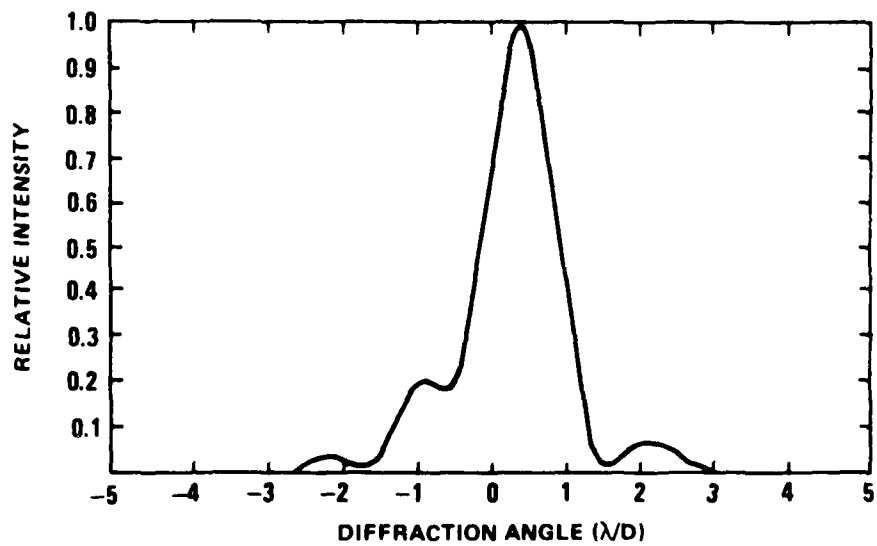
Figure 61.   Far-field pattern at 21 round trips.
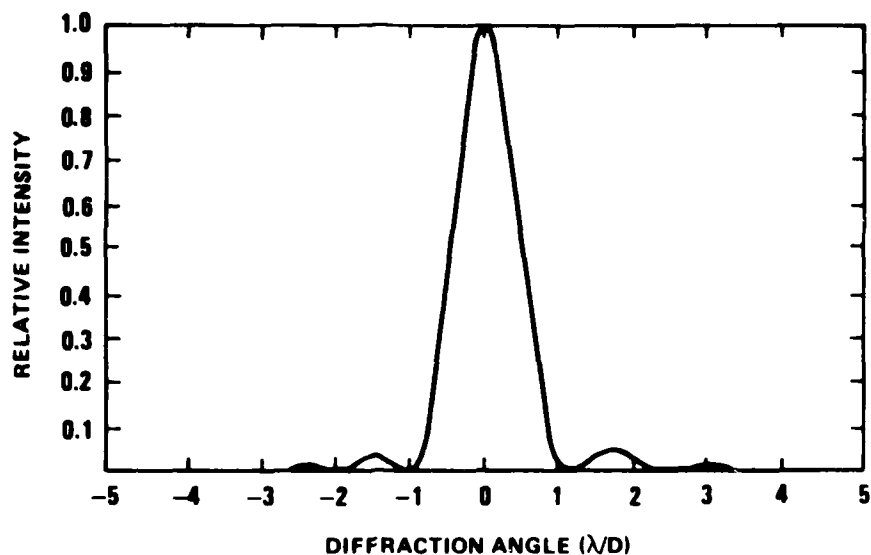
Figure 62. Far-field pattern at 24 round trips.

random phase numbers as in Figure 52 but without gain. A comparison of Figures 52 and 65 for the first few round trips is as expected--small gain in the loaded cavity gives results comparable to that of the empty cavity since intensity is not depleting the gain (small signal gain region). However, with the onset of saturated gain at 18 round trips the situation begins to change. The relative intensity of the dip located at approximately 21 round trips is much reduced in Figure 52 than in Figure 65. This causes a convergence at 22 round trips in Figure 52 instead of 27 as in Figure 65. The angular convergence in both figures is relatively unaffected. The overall effect appears to be a somewhat earlier mode formation time.

The statistical accumulation of the 20 empty cavity runs with the identical initial phase conditions of runs generated for Figures 63 and 63 is shown by Figures 66 and 67, respectively. The initial conclusion of earlier mode formation time in the loaded versus unloaded cavity cases is borne out by the statistical analysis of Figures 66 and 67.

The particularly poor convergence of the I/I_o statistics of the empty cavity runs as compared to the loaded cavity cases is apparent in Figures 63 and 66. An inspection of the individual runs of Figure 66 reveals that certain runs did not converge as expected but continued to change well beyond the Anan'ev criterion. This appeared to be caused by oscillation in the relative intensity values, and could be interpreted as competition of two or more modes of equal loss which would by necessity lengthen mode formation time. The application of typical gain in the CO_2 case seems to minimize if not eliminate this degeneracy. This potentially explains why mode competition has not been observed at mode crossing points which are located at

$$F_{eq} = n + 0.875 \quad . \tag{3.8}$$
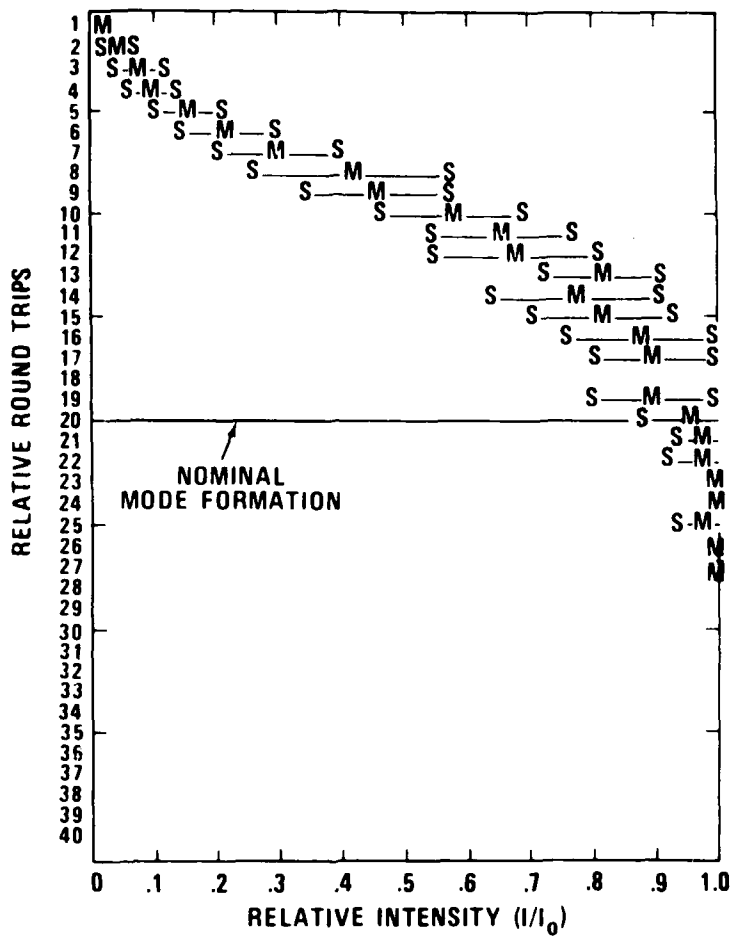
Figure 63. I/I_o statistics of 20 runs for CO_2 with gain, $M = 1.32$, $N_T = 279$.
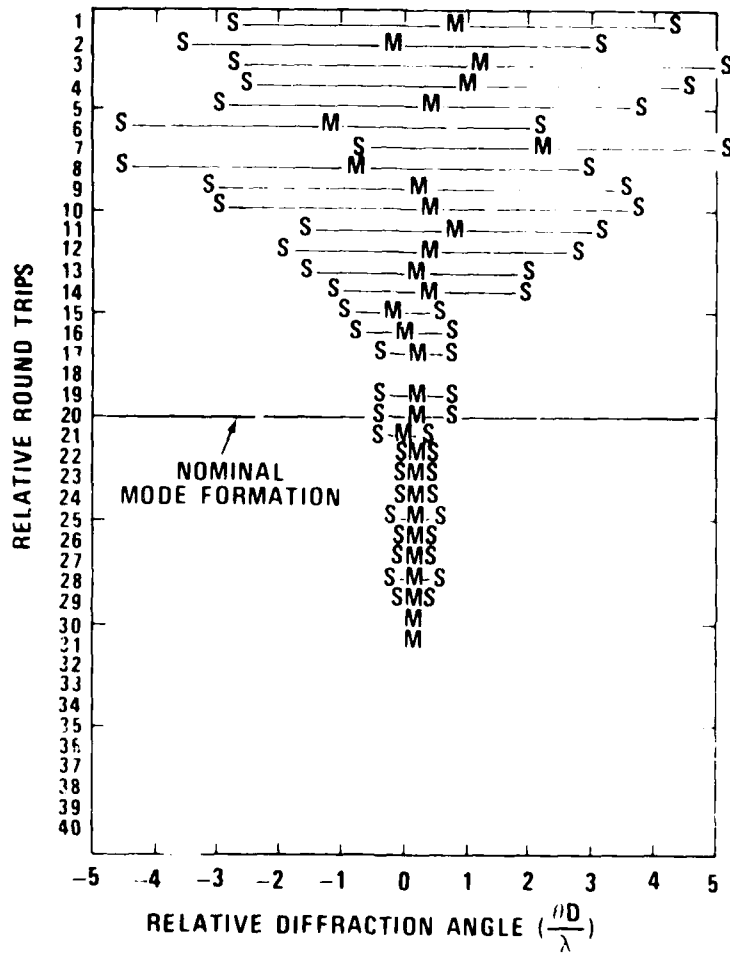
Figure 64. $\frac{\theta D}{\lambda}$ statistics of 20 runs for CO_2 with gain, M = 1.32, N_T = 279.
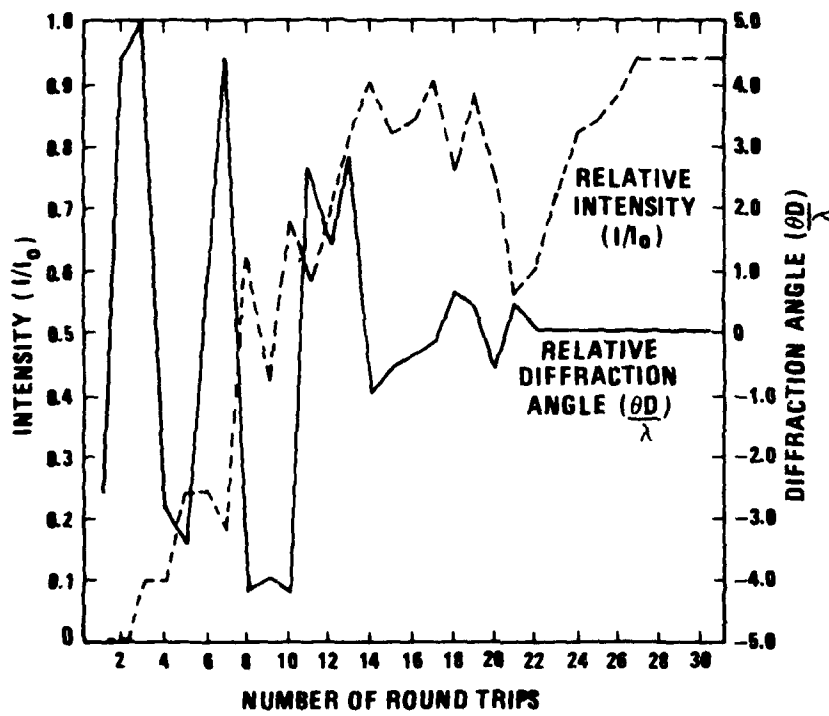
Figure 65. Empty cavity calculation of mode formation under
identical starting phase conditions of Figure 52
without gain, $M = 1.32$, $N_T = 279$.

Figure 66. I/I_o statistics of 20 runs for CO_2 with empty cavity,
M = 1.32, N_T = 279.

67
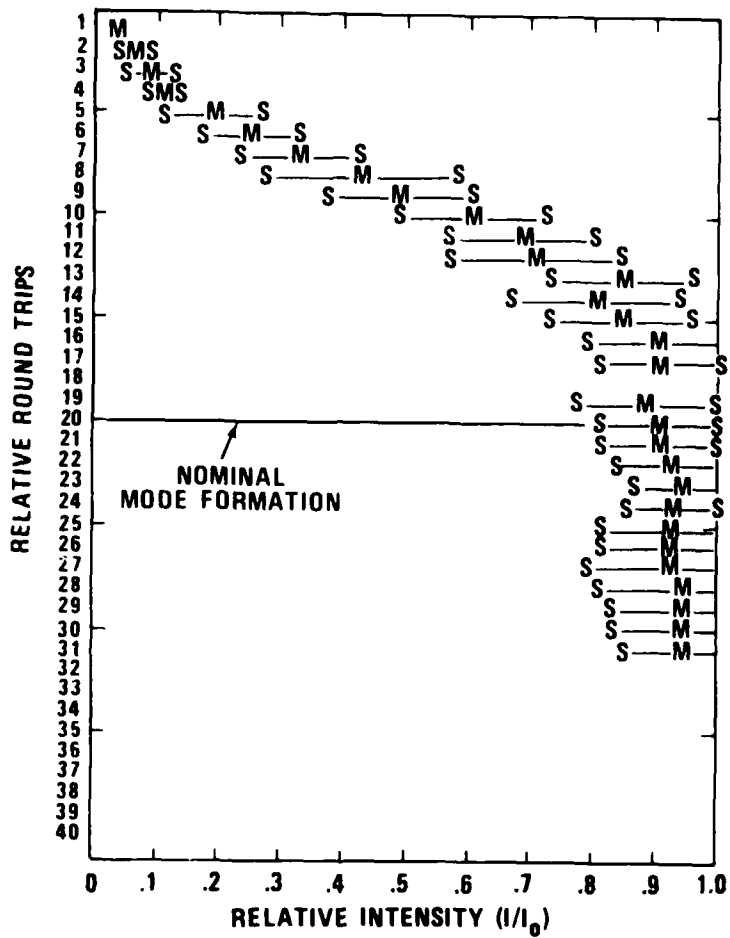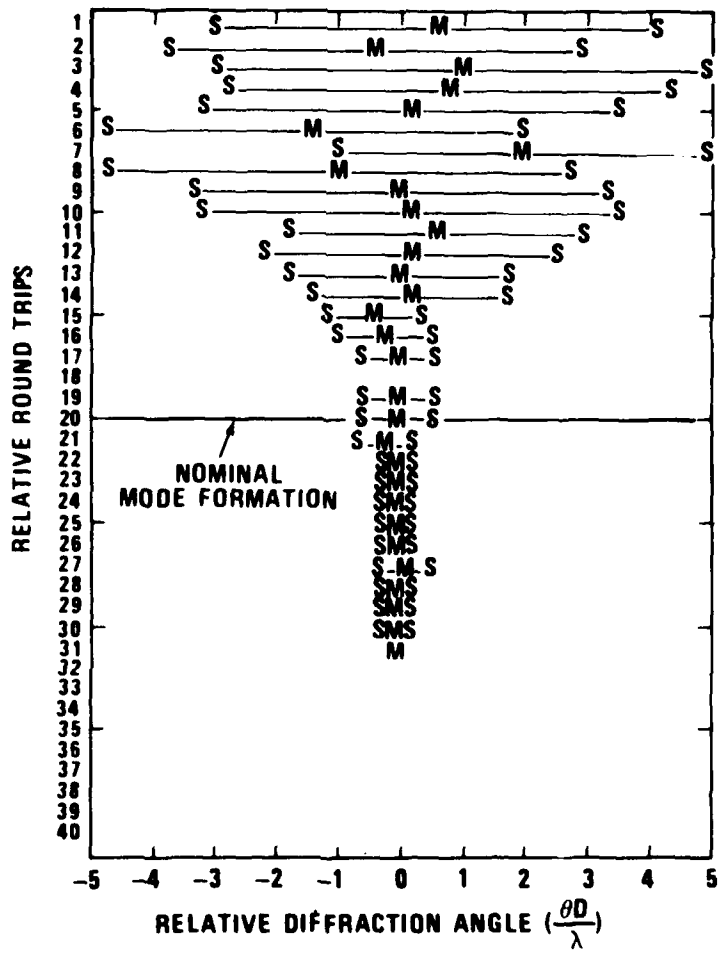
Figure 67. $\frac{\theta D}{\lambda}$ statistics of 20 runs for CO_2 with empty cavity, $M = 1.32$, $N_T \approx 279$.

We chose a Fresnel number for these calculations to produce maximum mode separation. However, the low magnification minimizes mode separation and emphasizes mode competition. This could be inherent within the definition of "mode formation time" for increasingly smaller magnification, especially in laser systems which do not saturate. In short, saturable gain appears to clear up any potential mode competition. Angular deviations in Figures 64 and 67 did not particularly appear to be affected by gain.

In one series of experiments, mode competition in the CO_2 laser was deliberately sought. This was done by spacing the resonator mirrors to give the "bad" equivalent Fresnel number of Equation (3.8). The two competing modes were calculated in empty cavity codes to have basically the same far-field pattern but differing phase angles. This should have given a temporal beat frequency easily observed in the near-field laser pulse with a photon drag detector. However, no such beat frequency was observed and far-field burn patterns were not abnormal. The tentative conclusion is that gain must eliminate or at least minimize the effects of mode competition in loaded resonators compared to the empty cavity results calculated by other authors at mode crossing points [61]. The formation, of a transverse mode at an earlier time with saturable gain for the empty cavity modeling results, may be analyzed in a similar manner as stable resonator modes [62]. In the empty cavity results, the lowest loss mode is obtained through diffraction losses in the resonator. With saturable gain, a nonlinear effect is added. The lowest loss mode tends to predominate earlier—by reducing the gain available to other competing modes—with the result that the mode forms earlier than with the empty cavity condition.

It will be shown for later cases of the excimer laser modeling at M = 1.32 that saturation seen early in the pulse at 10 round trips (compared to 30 round trips for mode formation) *readily gives an earlier mode formation for* loaded cavity than for empty cavity calculations and is well within the Anan'ev time.

C. XeF Laser Analytical Modeling

This work was similar to the CO_2 modeling but with the requirement of the larger tube Fresnel numbers of 2700 for the M − 1.32 resonator magnification case and 10,800 for the M = 2.7 case. In addition, the initial spontaneous intensity was much higher ($\sim 1 \times 10^{-4}$) for I/i_{sat} – in the excimer case at threshold). The average gain was fortuitously similar to that of CO_2 at 0.9%/cm. Saturation was achieved under these conditions much earlier than in the CO_2 cases at approximately 1/3 of the XeF mode formation time for M = 1.32 at 10 round trips.

Another restriction was the aperture vignetting necessary in the excimer laser cases. The M = 1.32 runs were analyzed through a near-field vertical rectangular stop of 1.21 cm width by a height of 6.5 cm. The 2.7 runs were even more restricted by a horizontal rectangle of 0.34 cm width by 1.75 cm length. These tended to change the mode formation time, apparently by a spatial filtering process.

In these cases, the tube Fresnel number was considerably larger than in the CO_2 runs (279 <u>versus</u> 2,700 - 10,800). The CO_2 runs were valid at 1024 mesh points: 16,384 were adjudged necessary for the XeF cases. The 10,800 tube Fresnel number was not as critical, in any event, since experimental results were not as precise for the rapid convergence of data in that magnification regime.

The statistical compilation of 15 runs with the gain conditions of the $M = 1.32$ XeF laser are shown in Figures 68 and 69. These cases include external vignetting with a 1.21 x 6.5 cm rectangle in the laser beam. Mode formation has been obviously moved to shorter times with respect to the Anan'ev formula. This appears to be partly a result of the vignetting process but primarily of early gain saturation. Saturation was achieved in Figures 68 and 69 after approximately 7 relative round trips (10 actual round trips). Relative round trips are defined in the statistical runs as the Anan'ev time normalized to 20 round trips.

A comparison must be made of these data with those of Figures 70 and 71 for empty cavity calculations with identical initial random phase starting conditions for each run. Again, as in the CO_2 cases, saturable gain plays a part in mode formation. In the loaded cavity (Figure 68) the mode is formed after approximately 14 relative round trips, whereas in the empty cavity (Figure 70) it has developed after approximately 18 relative round trips.

The angular development of the mode is not appreciably different in either case (Figures 69 and 71). Vignetting appears to move mode formation to slightly earlier times compared to the relative Anan'ev time.

The empty cavity results have been statistically analyzed for the $M = 2.7$ cm case in Figures 72 and 73. Thirteen runs similar to those of Figures 70 and 71 were utilized in the calculations. These were run at a mesh point dimension of 16,384. One individual run was obtained as a comparison to Figures 72 through 73 with 32,768 mesh points. The convergence results were similar. This represents the maximum memory capability of the CDC 7600 computer for these calculations. An accurate reproduction of the near-field phase and intensity for the $M = 2.7$ resonator would require approximately 60,000 mesh points. The consequence of a smaller number of mesh points is a smoothing of the near-field phase and intensity, giving a spatially filtered effect in the far-field. This appears as a secondary influence on mode formation.

Vignetting is more important in the $M = 2.7$ case because of the smaller vignetted aperture which causes more spatial filtering. Excluding any gain effects, the mode formation time has been moved back to 16 round trips as opposed to 20.

Finally, in this series, consider Figures 74 through 77 which were run with full aperture for the excimer case of $M = 1.32$, $N_T = 2700$. These cases were run for comparison with previous vignetted examples to show earlier mode formation from vignetting and also to directly evaluate saturable gain effects in large aperture excimer lasers. The mode formation time was found to move forward from 14 round trips (Figure 68) to 16 round trips (Figure 74) presumably
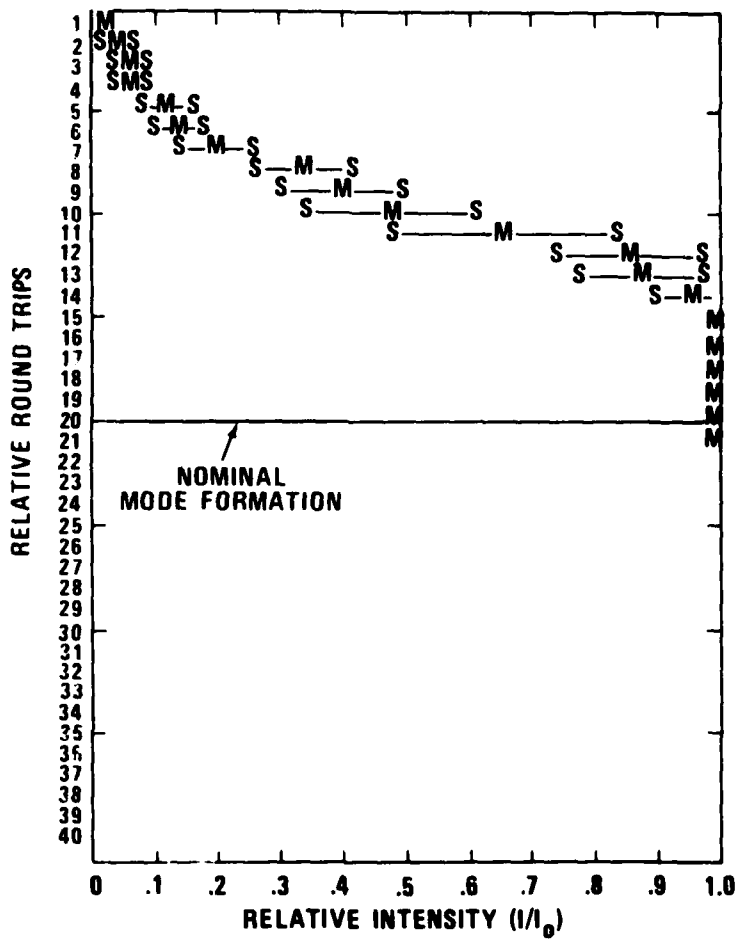
Figure 68. I/I_o statistics of 15 runs for XeF with gain and vignetting, M = 1.32, N_T = 2700.
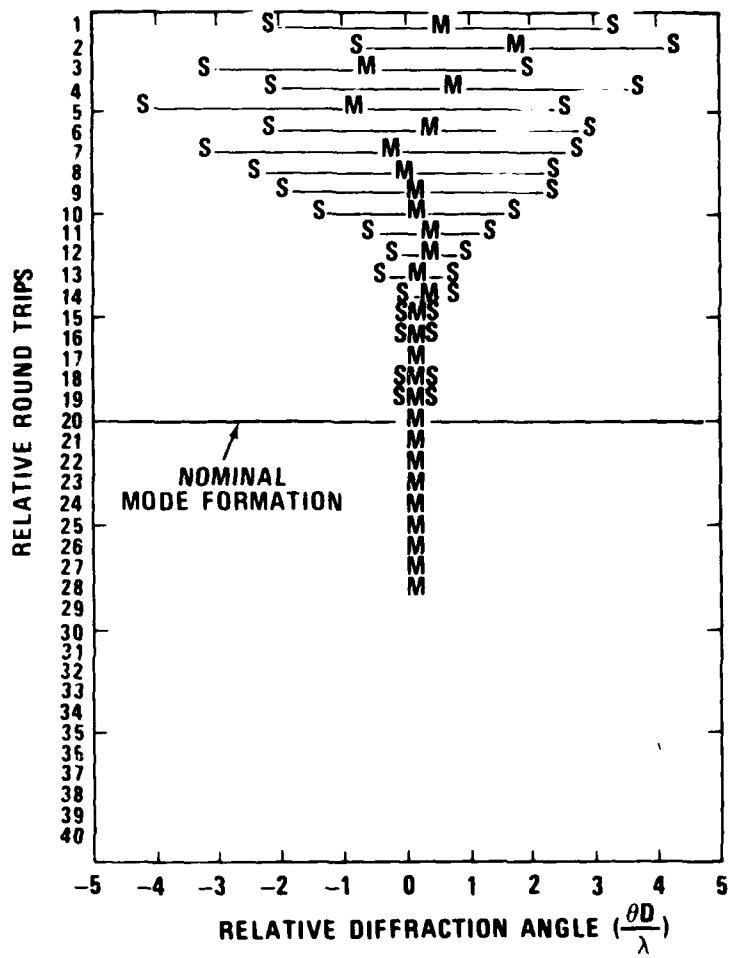
Figure 69. $\frac{\theta D}{\lambda}$ statistics of 15 runs for XeF with gain and vignetting, $M = 1.32$, $N_T = 2700$.
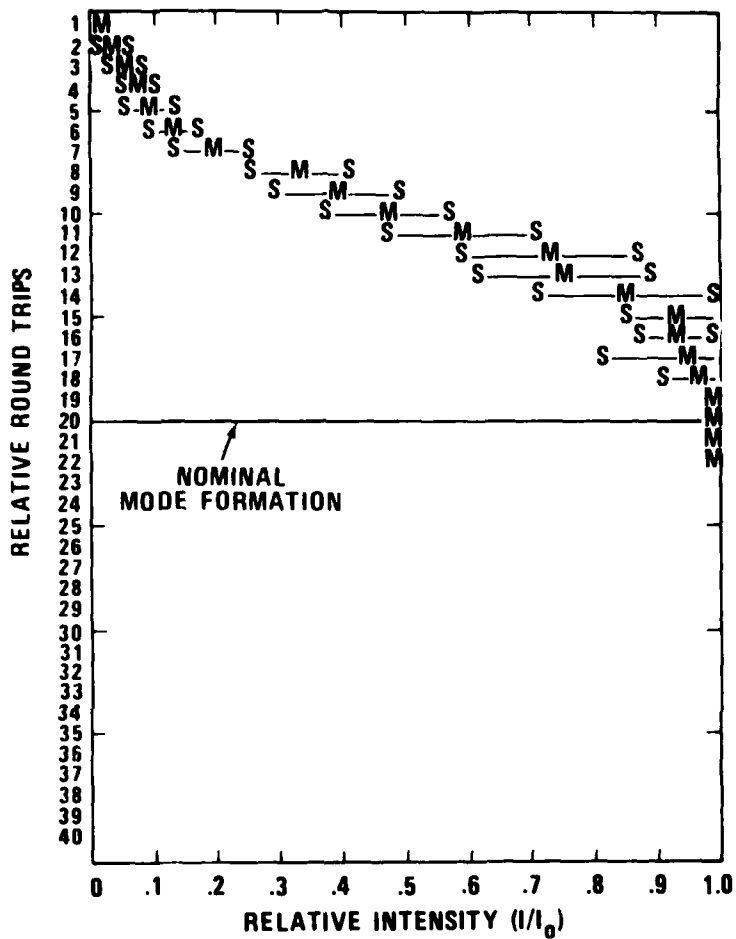
Figure 70. I/I_o statistics of 15 runs for XeF empty cavity calculations and vignetting, $M = 1.32$, $N_T = 2700$.

RELATIVE ROUND TRIPS

S — M — S
S — M — M — S
S — M — M — S
S — M — S
S — M — S
S — M — S
S — M — S
S — M — S
S — M — S
S — M — S
S — M — S
S-M-S
S-M-S
S-M-S
SMS
SMS
SMS
SMS
M
M
M
M
M
M
M
M
M
M

NOMINAL
MODE FORMATION

RELATIVE DIFFRACTION ANGLE ($\frac{\theta D}{\lambda}$)
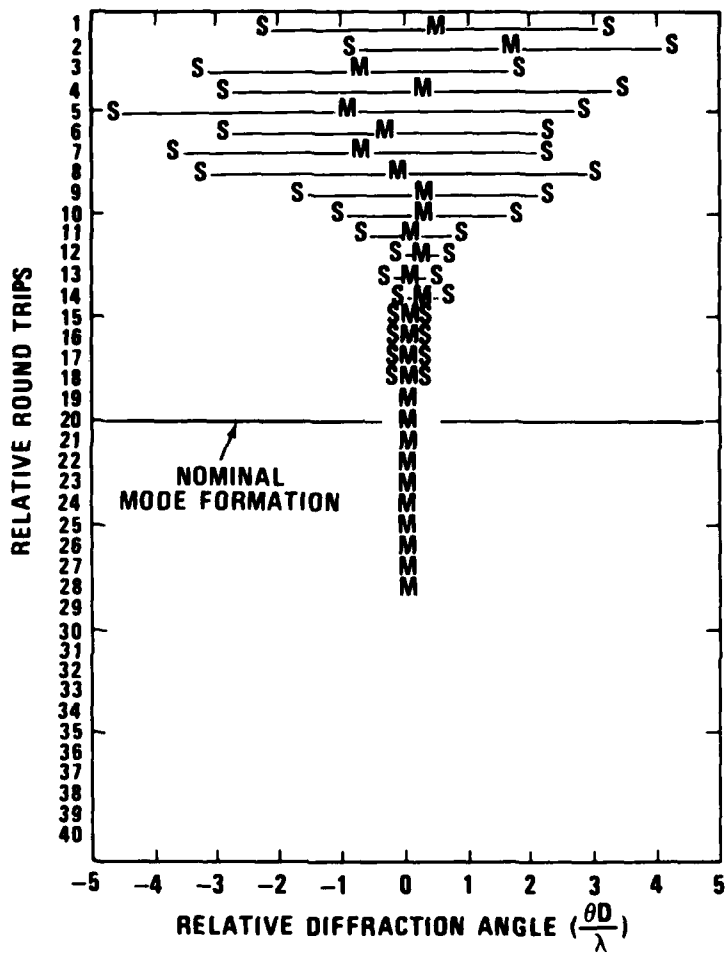
Figure 71. $\frac{\theta D}{\lambda}$ statistics of 15 runs for XeF empty cavity calculations and vignetting, $M = 1.32$, $N_T = 2700$.
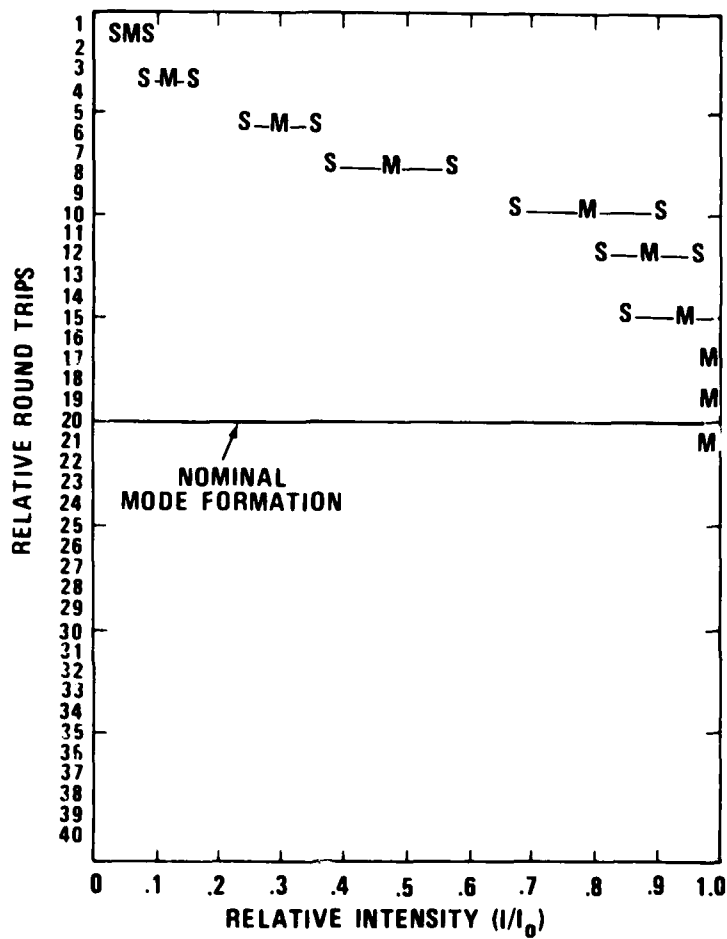
Figure 72. I/I_o satistics of 13 runs for XeF empty cavity calculations and vignetting, M - 2.7, N_T = 10,800.
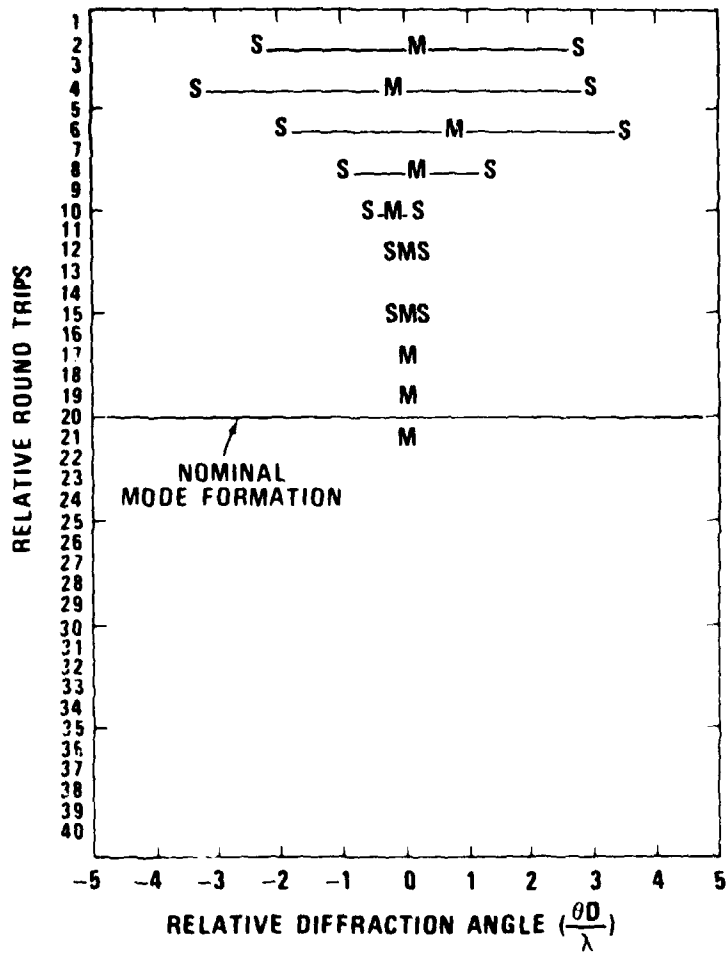
Figure 73. $\frac{\theta D}{\lambda}$ statistics of 13 runs for XeF empty cavity calculations and vignetting, $M = 2.7$, $N_T = 10,800$.
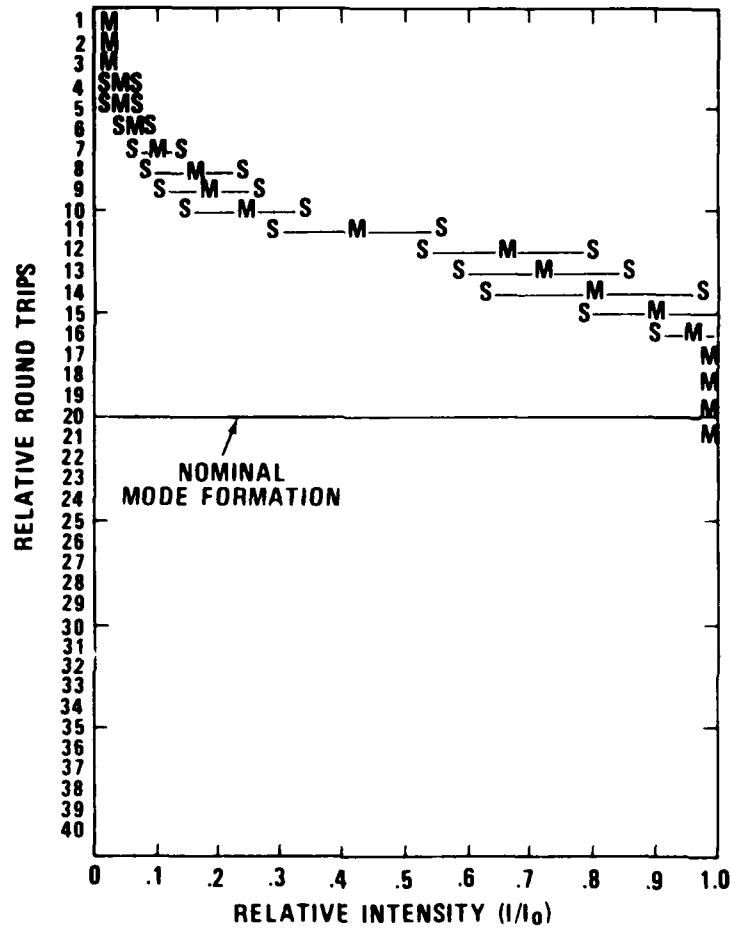
Figure 74. I/I$_o$ statistics of 13 full aperture runs for XeF
with gain, M = 1.32, N$_T$ = 2700.

77

because of the absence of vignetting effects. Also, the angular selection is not as rapid for the nonvignetted case (Figure 75) as for the vignetted case (Figure 69). As a concluding example, Figures 76 through 77 show full aperture from runs for the excimer laser case M = 1.32, N_T = 2700, without gain.

A comparison of these figures to Figures 74 through 75 shows that saturable gain does significantly affect mode formation time. The same initial random phase of the runs in Figures 68 through 69 was used to generate Figures 74 through 75 and Figures 76 through 77 for direct comparison.

In general, early mode formation time of the XeF experimental data may be explained by Figure 68. Without respect to experimental considerations of poor far-field resolution, the mode has formed early in time. In fact, the figure shows mode formation at about 14 relative round trips (about 360 nsec) rather than 20 relative round trips (513 nsec). An examination of the experimental results for the M = 1.32 resonator of Figure 49 gives a comparable answer. Therefore, the modeling and the experiment agree in terms of the results. Mostly as a result of saturable gain, however, the mode is formed ahead of the nominal Anan'ev time.

A consideration of the M = 2.7 results produces a similar conclusion. The extreme vignetting in this case moves the mode formation to an earlier time than it is in the M = 1.32 case. The empty cavity calculations of Figures 72 through 73 show the mode to have been formed around 16 relative round trips. This is a time of 134 nsec which is consistent with the results of Figure 51. In this case, because of larger magnification, mode competition is not a serious problem, and with earlier mode formation saturable gain should not be as much of an effect in moving back mode formation time. Spatial filtering, because of extreme vignetting, should be the predominating variable.

IV. CONCLUSIONS AND RECOMMENDATIONS

The geometrical formulation, as proposed by Anan'ev for the formation of transverse modes in positive branch unstable resonators as an upper limit, has been validated experimentally and by statistical modeling for moderate resonator magnifications ($1.32 \leq M \leq 2.7$) over a large regime of tube Fresnel numbers ($279 < N_T < 10,800$).

A. Summary of Experimental Results

The objective of these experiments was to observe the far-field pattern from two selected high energy lasers, CO_2 amd XeF. at times before,

during, and beyond nominal transverse mode formation time, as predicted from geometric optics theory. This represents the transition time required for the laser to convert the radiation in the cavity from initial spontaneous emission to a quasi-steady-state self-replicating wavefront characteristic of a dif- fraction limited laser beam.

The initial temporal points of the lasers were referenced to threshold gain conditions experimentally determined by small signal gain measurements. Mode formation was determined from the threshold time to the time required for steady-state formation of the far-field pattern.
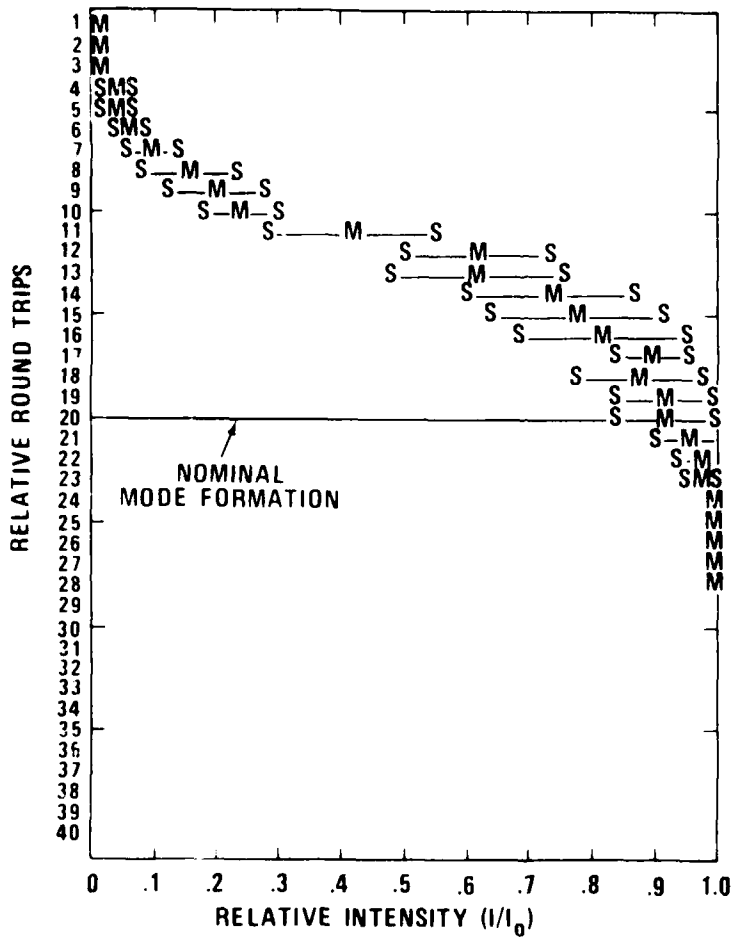
RELATIVE ROUND TRIPS

RELATIVE INTENSITY (I/I₀)

NOMINAL
MODE FORMATION

Figure 76.   I/I$_o$ statistics of 13 full aperture runs for XeF
without gain, M = 1.32, N$_T$ = 2700.

80
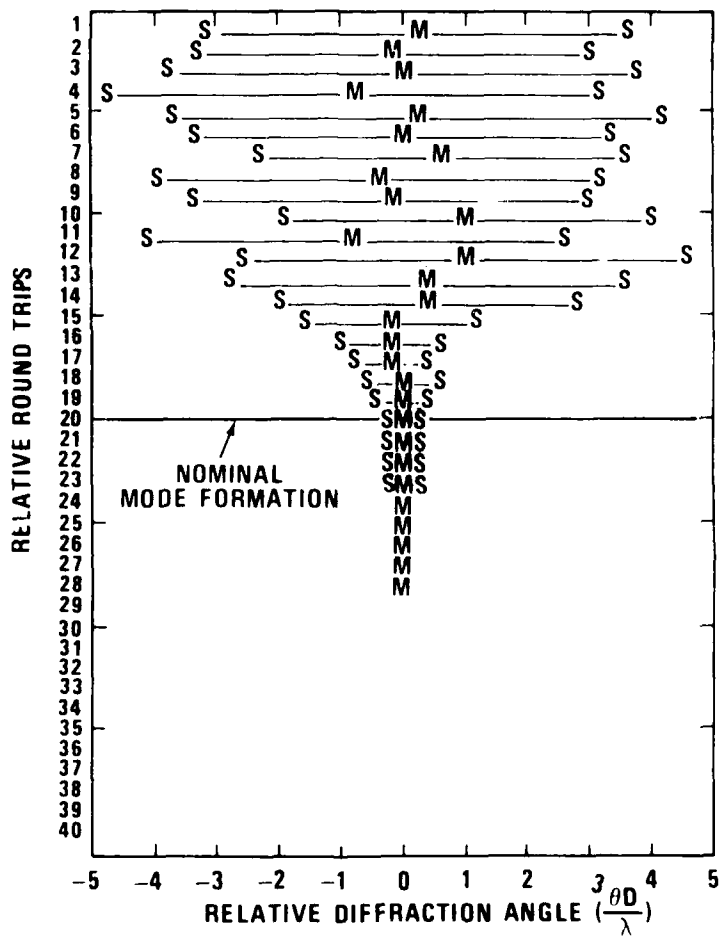
Figure 77. $\theta D/\lambda$ statistics of 13 full aperture runs for XeF without gain, M = 1.32, N_T = 2700.

81

The CO_2 experiments examined far-field burn patterns of truncated pulses which were varied before and beyond the nominal mode formation time by variation of laser gain. These data indicated mode formation in the range of 460-520 nsec. agreeing well with the predicted value of 490 nsec for an M = 1.32 resonator.

The XeF experiments used an electronically imaged-gated framing camera to observe a fluorescing image in the far-field. The advantage of the XeF laser was that it "turns on" early with high peak power, allowing the far-field to be observed in one series of experiments at approximately half the predicted mode formation time. These data indicated mode formation in the regime of 300 - 400 nsec (predicted mode formation time 513 nsec) for an M = 1.32 resonator and 130 - 180 nsec (predicted mode formation time 168 nsec) for an M = 2.7 resonator.

The apparently anomalous early mode formation time of the XeF cases can be justified by modeling analysis of saturable gain and laser aperture vignetting, as well as by poor far-field patterns. Poor far-field patterns were the result of severely degraded resonator optics and poor imaging quality of framing cameras. These characteristics made it difficult to determine a reasonably exact time of formation of the mode.

The results of the CO_2 work indicate a formation time consistent with the Anan'ev prediction. The XeF work gives a significantly earlier time for mode formation.

B. Summary of Theoretical Modeling

The CAV2D code used in this work was a modification of earlier codes which derived the lowest loss transverse mode in unstable resonators. It used Fourier propagation within the resonator to develop a self-consistent steady-state wavefront output.

The code had some time saving devices built into it: the fast Fourier transform (FFT) algorithm and an expanding coordinate system.

Instead of being interested in the steady-state transverse mode, we desired to obtain wavefront properties of phase and amplitude at each round trip in the resonator at an early time and project these properties to the far-field for statistical analysis. A random phase, uniform amplitude wave was launched to begin a convergence process as a function of resonator round trip.

Statistical modeling of the CO_2 case showed convergence around the Anan'ev time and agreed with the CO_2 experiments. Modeling with vignetting in the XeF cases showed the convergence time of the lowest order steady-state mode to be considerably earlier than the Anan'ev mode formation time. This was consistent with the experimental evidence.

An interesting result of the analytical work was that saturable gain early in time had an appreciable effect in developing a steady-state pattern in the far-field considerably sooner than in the empty cavity case or Anan'ev

predictions. With the knowledge of early saturable gain in certain high energy lasers, it appears that the Anan'ev formula is quite conservative and that the actual transverse mode forms earlier in time.

C. Recommendations for Future Work

It would be desirable to repeat the XeF experiments under better conditions which would allow more accurately determined mode formation times in the range of resonator magnifications ($1.3 < M < 3$) of interest. The modifications suggested for a more accurate set of results are:

(1) the use of better resonator optics (better than $\lambda/20$ RMS surface figure),

(2) the use of technologically current gated-image cameras having more frames and greater spatial resolution per run), and

(3) the use of the full aperture of the laser for far-field analysis, which would necessarily require large, good quality optics to direct a 10 x 20 cm beam (the size of the "2 Meter Maxwell laser" beam).

Recent communications with individuals at Maxwell Laboratories, Incorporated, at San Diego, California indicate that work in these directions is now in progress [52].

APPENDIX A

CAC2D CODE DESCRIPTION [63]

CAV2D is primarily a two-curved-mirror code, which is realistic for most unstable resonators. The most common mirror configuration for unstable resonators includes a concave mirror which is at least as large in transverse extent as the gain region, and a convex mirror which is smaller than the gain region. A substantial fraction (the outcoupling fraction) of the radiation is propagated from the concave mirror toward the convex mirror, passing outside of the convex mirror and is emitted fror the resonator. The convex mirror is taken as mirror number one in the code, while the concave mirror is mirror number two. For convenience the calculation is normally started with a wave which has just been reflected from the convex mirror. For ordinary calculations not involving modeling of mode formation, this starting wave is uniform in intensity. It also has a phase distribution which is the same as would apply to an idealized, i.e., geometric-optics, resonator wave.

The most common configuration is a confocal or near-confocal one. However, this limitation is not imposed in the code. Instead, the code accepts as input data the g values (XG1 and XG2) of each mirror. Near statement 10 there is a calculation of the normalized (i.e., measured in units of the mirror separation) radius of curvature (RP1 and RP2) of each of the mirrors, and the corresponding magnifications (XMAG1 and XMAG2) associated with propagation from mirror 1 to mirror 2 and from mirror 2 to mirror 1, respectively. When the input g values correspond to a confocal resonator, the magnification XMAG2 is unity, corresponding to a collimated beam propagating from mirror 2 toward mirror 1, while the magnification XMAG1 equals the overall magnification which in magnitude equals the ratio of radii of curvature of the two mirrors. The advantage of dealing with g values is that these quite general formulas are based on g values as independent variables. Of course, the code could start with input radii of curvatures and calculate the g values.

Near statement 8 the code tests the g values to see whether they correspond to the unstable resonator. If the resonator is stable, the code rejects that set of input data, prints a message (format 86) "STABLE RESONATOR," and proceeds to the next set of input data. If desired, this could be modified to permit calculations of stable resonators. The code detects whether the mirrors are reversed from the normal ordering in which mirror 1 is the convex mirror. If the ordering is reversed, a message is printed (format 96) "BACKWARD WAVE CALCULATION" and the values of XMAG1 and XMAG2 are suitably adjusted. This feature has only been used for limited tests.

A factor, named FACT, which is the ratio of the number of total mesh points (XNTOT or NTOT) to the number of mesh points across each mirror (XMIR or XNMIR), enters into various steps. The total Fresnel numbers XNF1T and XNF2T, which are involved in the propagation kernals, are greater than the input values, XNF1 and XN2T, of the ordinary Fresnel numbers of the mirrors by the square of this factor.

The ratio of the transverse size of the mirrors, A1OA2, and its reciprocal, A2OA1, are needed in determining the location of points involved in the interpolation process. They are obtained as the square root of the ratio of Fresnel numbers of the two mirrors, and its reciprocal. These are calculated below statement 5.

If the two g values are equal and the two Fresnel numbers are equal, the resonator is symmetric (this special case is often used as discussed elsewhere). [23] A test for this is made at consecutive statements 126 and 112. If the resonator is symmetric, a message (format 83) "SYMMETRIC RESONATOR" is printed, and a simple formula is used to calculate the equivalent Fresnel number FEQ. It it is not symmetric, a message (format 84) "NONSYMMETRIC RESONATOR" is printed; and FEQ is calculated by a more involved formula. The latter is based on the formulation for an equivalent symmetric resonator (which assumes that the actual concave mirror is oversized as compared to the beam). GEQ is the g parameter of the "symmetric-equivalent" resonator, and XNSEQ is its Fresnel number. The relevant formulas are given in the "crib sheet." In either event, the value of FEQ is printed. The special feature, which treats a ring resonator with unequal lengths of the two paths, will not be considered here.

To determine when the iterations have converged, use is made of the ratio of the complex amplitude at a test position on two successive round trips. This position is determined by the value of an input parameter TSTFR (whose default value is zero), such that the position is removed from beam center by an amount equal to TSTFR times the half-width of the overall beam (including guard band).

CAV2D Program Modules

The program consists of the following modules, of which all but the MAIN program are subroutines:

MAIN	GGNPM
PROPCBM	GGUBS
FOURT	BQUAL
INTRP	PHSEM
NFLPP	
FRFLD1	
GAINM2	
MFLPP	

The four modules listed in the right-hand column are of relatively minor signficance but have been listed for completeness. The GGNPM and GGUBS subroutines are taken from the IMSL Library which is available on most mainframe computers. If RNPH2 is non-zero, a correlated randomness of phase at the position of mirror 2 is applied to simulate effects such as gas density fluctuations. The random numbers for that purpose are obtained from GGNPM, but this is not of much current interest. For mode-formation calculations, a randomness is applied to the phase of the starting wave. This is called, if the parameter RANST (mnemonic for "random start") is non-zero. The pseudo-random numbers used for that purpose are obtained from the subroutine GGUBS. BQUAL calculates a simple measure of beam quality, but it is not as useful as

88

calculating the overall far-field intensity distribution. PHSEM can be used
to introduce a "phase modulation" across the beam, but is probably not needed
for future work.

The MAIN program controls the overall calculations. It reads input data,
initializes various arrays, registers and prepares the "starting wave;"
then begins the iterative process of calculating propagation back and forth
between the two mirrors. This iterative process is continued until it either
satisfies a convergence criterion (based on input or default value of CVTST
parameter) or completes the maximum prescribed number of iterations, XMITR.
The program always prints the values of data parameters, which determine the
problem being calculated, and generates at least one line of print for each
iteration, which gives an indication of the iterative behavior. It optionally
calls the line printer plotting program NFLPP, and produces plots of intensity
and/or phase across the entire aperture. An earlier version could optionally
plot across one-half of the mirror; but the current version does not permit
this, as it is not appropriate if the resonator is not ideally aligned.
Control parameters PLLP1 and PLLP2 control the plots at position 1 and 2.
Such plots may optionally be made only after completion of the iterations (if
PLLP1 or PLLP2 equals unity) or after each iteration (if PLLP1 or PLLP2 equals
two). Upon completion of one problem, the MAIN program reads input data for
another problem, if such is available.

The overall program is arranged such that the typical phase distribution
is an idealized flat distribution across the reference surface, i.e., a
pseudo-collimated beam is being propagated. Of course, there are departures
from such ideal behavior at the starting point for each propagation step, and
departures that arise from diffraction as a result of each propagation step.
The MAIN program establishes the complex amplitude distribution U(I) prior to
each propagation step, then calls the PRPCBM (mnemonic for "propagate colli-
mated beam") subroutine. The MAIN program also furnishes to the PRPCBM sub-
routine the value of the overall Fresnel number (called XNFT in the PRPCBM
subroutine) for the propagation step, and a value of the parameter XPAVG as
well as the total number of mesh points, NTOT. XPAVG is most commonly set
to unity. If XPAVG is greater than unity, the propagation kernel is averaged
over XPAVG subintervals at each mesh point. The PRPCBM subroutine, in turn,
calls the fast-Fourier-transform subroutine FOURT. The values of complex
amplitude after propagation are returned in the same array U(I). FOURT is
the only subroutine that is called by another subroutine; all others are called
by MAIN.

After each return from the propagation subroutine PRPCBM, the MAIN pro-
gram can optionally call the plotter program NFLPP. In addition, after re-
turn from PRPCBM for propagating from mirror 2 back to mirror 1 (i.e., back to
the position of the convex mirror), there is an optional call to FRFLD1 for
calculation of the far-field intensity distribution. The call to FRFLD1 is
made for each iteration, if the control parameter CFFLD is greater than
unity; this option is useful in mode formation calculations. Aside from
these optional calculations, the interpolation subroutine INTRP is called
after completion of a propagation step in order to obtain the complex ampli-
tude distribution across the "receiving" mirror in a suitable form. The
propagation steps have generated the complex amplitude distribution at points
which cannot cover the receiving mirror with NMIR mesh points, as desired. For
example, in the propagation from concave to convex mirror of a confocal

89

resonator, the calculated distribution has the range of NMIR points, covering the full size of the beam; whereas one wants to determine a new distribution with NMIR points, covering the small size of the convex mirror.

After interpolating to find the distribution across the "receiving" mirror, there is an optional call to the plotter program NFLPP to plot the distribution across the entire aperture, as referred to earlier.

After completion of the two propagation steps and associated options, the program saves the ratio of the amplitudes (at a selected position) for the last two iterations. This ratio is used to generate a test parameter TEST, which approaches zero as the calculation converges, i.e., as the ratios for successive round trips tends to become the same with each new round trip. The absolute value of the difference from unity, called ABTS, is tested again in a preselected convergence test parameter, CVTST. When it is less than CVTST on two successive evaluations, the calculation is assumed to be successfully converged (as signalled by the parameter STOPTS being equal to two).

After convergence, there is an optional plot of near-field distribution as noted above. Also, there is an optional calculation of the far-field intensity distribution by the FRFLD1 subroutine. Often, the far-field intensity distribution is also plotted. For mode formation calculations, there would be excessive printed output, if the far-field distribution were plotted each time it is calculated, namely, after each iteration. Hence, an option is provided to omit the far-field pattern. For mode formation studies, the values of IMXFF(ITER) and of FFMAX(ITER) are calculated in the FRFLD1 subroutine and returned to the MAIN program. For simplicity, these values are always generated, even if CFFLD is not greater than unity, so as to produce mode formation plots as discussed below. These are the values of the angular position of the most intense far-field point and the relative intensity (compared to the value for a uniphase near-field output with the same integrated intensity) at that point, for the present iteration, as indicated by the index ITER.

Upon completion of the iterative process, the MAIN program may optionally (if CFFLD is greater than unity) call the "mode formation" subroutine MFLPP. The subroutine produces a line-printer plot of the values of FFMAX(ITER) and IMXFF(ITER) for inspection. The arrays are printed with identifying parameters to logical unit number 1 for punching into cards for further analysis. This writing to unit 1 will be suppressed if PCHMF is less than or equal to zero.

After completion of one problem, control is transferred to the beginning of the program (by a GO TO 1 statement) to read input data for a new problem.

APPENDIX B

CAV2D CODE LISTING

```
      DIMENSION U(32768), UP(32768)
      DIMENSION RNORM(32768),CRAND(32768)
      DIMENSION IMXFF(250),FFMAX(200)
      COMPLEX U,UP
      COMPLEX RAT1,SAVU1,SAVU1P
      COMMON /COM1/U/COM2/UP/COM3/RNORM/COM4/CRAND
      LEVEL 2, U,UP,RNORM,CRAND
      COMPLEX PRMT,CFKTR
C***************THIS DOUBLE-PRECISON NEEDED BY NATURE OF SUBROUTINE
      DOUBLE PRECISION ISEED,JSEED
   61 FORMAT(1X,4F10.5,E10.4,F10.5)
   70 FORMAT(1H0,9HCONVERGED)
   71 FORMAT(1H0,20HMAX NO OF ITERATIONS)
   76 FORMAT(1H0)
   77 FORMAT(1H1)
   78 FORMAT(2X,1*HERROR IN CAVT7)
   83 FORMAT('   SYMMETRIC RESONATOR')
   84 FORMAT('   NON-SYMMETRIC RESONATOR')
   85 FORMAT('   EQUIVALENT FRESNEL NUMBER FEQ=',F10.5)
   86 FORMAT(1X,16HSTABLE RESONATOR)
   87 FORMAT(' SPECIAL TREATMENT OF RING RESONATOR WITH UNEQUAL PATHS')
   88 FORMAT(' OF COLLIMATED AND EXPANDING BEAMS. FEQP= ',F10.5)
   89 FORMAT(1X,4HXG1=,F10.5,5X,4HXG2=,F10.5,5X,5HXNF1=,F10.5,
     15X,5HXNF2=,F10.5,5X,5HEPSL=,F10.5)
   90 FORMAT(1X,6HXNTOT=,F10.5,5X,6HXNMIR=,F10.5)
   91 FORMAT(1X,6HXMAG1=,F10.5,5X,6HXMAG2=,F10.5)
   92 FORMAT(1X,6HXNF1T=,F10.5,5X,6HXNF2T=,F10.5)
   93 FORMAT('     XMITR     RAT1AM     RAT1PH     GAMRT     AVFLX     OUT
     1CP')
   94 FORMAT('            EMPTY RESONATOR CALCULATION')
   95 FORMAT('   LOADED RESONATOR CALCULATION WITH GAIN IN NARROW REGION
     1NEAR MIRROR 2. GAIN SATURATION BY RIGROD-LIKE SCHEME.')
      NAMELIST/CVDAT/XG1,XG2,XNF1,XNF2,XNTOT,XNITR,XLAST,
     1XNTOR,CFFLD,      XNMIR,PA112,      XPAVG,      EPSL,GL, RANST,
     2                             TVBQ,QDGLP,        PLLP1,PLLP2,
     3          PHAM1,PHAM2,PHCY1,PHCY2,GNOFS,INCPL,BMTLT,XINTS,
     4RNPH2,ISEED,NCRLT,JSEED,WRCRN,XSPAM,XHM2F,XFCTR,AMPRF,PHSRF,ISKMF,
C*********TSTFR ADDED 26 NOV 80.
C*********RTPHS ADDED 27 JAN 81.
     5STOPN,XLPOL,TSTFP,PRDGS,CVTST,XININT,FRINF,BMTIN,RTPHS,PCHMF,
     6FNFCS,SPCLFF,FRCMSK
      DATA STOPN/2.0/
      DATA XG1,XG2/1.25,1.25/
      DATA XNF1,XNF2/12.8,12.8/
      DATA XNTOT,XNMIR/512.0,256.0/
      DATA XNITR/1.0/,XLAST/0.0/,XNTCR/3.0/,           CFFLD/0.0/
      DATA GL/0.0/,                PA112/2.0/,          EPSL/0.0/,XPAVG/1.0/
      DATA                         TVBQ/0.0/,QDGLP/0.0/,BMTLT/0.0/
      DATA PLLP1/0.0/,PLLP2/0.0/
      DATA     TSTFR/0.0/
      DATA PHAM1/0.0/,PHAM2/0.0/,PHCY1/0.0/,PHCY2/0.0/,GNOFS/0.0/
      DATA INCPL/1/,XINTS/1.0/,RANST/0.0/
      DATA RNPH2/0.0/,JSEED/55555.0/,NCRLT/12/,ISEED/33333.0/,WRCRN/0.0/
      DATA XSPAM/0.0/
      DATA XHM2F/0.0/,XFCTR/0.0/,AMPRF/0.0/,PHSRF/0.0/
```

```
       DATA ISKMF/1/,PCHMF/0.0/
       DATA XLPOL/1.0/,PRDGS/0.0/
       DATA PI/3.141592654/
       DATA CVTST/0.001/
       DATA XININT/0.000 /,FRINF/0.0001/,EMTIN/0.0  /
       DATA HTPHS/0.0/,FNFCS/0.0/,SPCLFF/0.0/,FRCMSK/0.0/
       NX= 32768
C******READ AND WRITE INPUT DATA AND DO INITIAL CALCULATIONS.************
     1 READ (5,CVDAT)
       IF(XLAST)99,4,9001
     4 WRITE(6,CVDAT)
       STP = STOPN-1.0
       NTOT=XNTOT
  9999 IF(NTOT .LE. NX)GO TO 950
       WRITE(6,940)
   940 FORMAT(' INVALID RUN SINCE NTOT WAS GREATER THAN NX.')
       STOP
   950 CONTINUE
       IF(XNITR .LE. 200.0)GO TO 952
       WRITE(6,951)
   951 FORMAT(' XNITR EXCEEDS 200.0 NOT SUITABLE RE IMXFF AND FFMAX.')
       STOP
   952 CONTINUE
       NMIR=XNMIR
       RAT1TS=1.0
       STOPT=0.0
       XMITR=1.0
       G1G2=XG1*XG2
C********STABLE RESONATORS ARE REJECTED.
       IF(G1G2)10,8,8
     8 IF(G1G2-1.0)9,9,10
     9 WRITE(6,86)
       GO TO 1
    10 XARG=G1G2*(G1G2-1.0)
       XARG=SQRT(XARG)
       IF(G1G2 .LT. 0.0)XARG=-XARG
       RP1=XG2/(XARG+G1G2-XG2)
       RP2=XG1/(XARG+G1G2-XG1)
       XMAG1=1.0+1.0/RP1
       XMAG2=1.0+1.0/RP2
       IF(XNF2-XNF1) 3,5,5
     3 WRITE(6,96)
    96 FORMAT('    BACKWARD WAVE CALCULATION')
       XSAVV=XMAG1
       XMAG1=1.0/XMAG2
       XMAG2=1.0/XSAVV
     5 FACT=XNTOT/XNMIR
       FACT=FACT**2
       XNF1T=XNF1*FACT*XMAG1
       XNF2T=XNF2*FACT*XMAG2
       XNF2T=XNF2T/XLPOL
       ARG=XNF2/XNF1
       A2OA1=SQRT(ARG)
       A1OA2=1.0/A2OA1
       WRITE(6,76)
       WRITE(6,89)XG1,XG2,XNF1,XNF2,EPSL
       WRITE(6,90)XNTOT,XNMIR
```

```
IAG2
IF2T


,114
,99


51)/2.0*XNF1


52)
/XG2)
*2-1.0)
0)/(XMAG1+XLPOL)
     WRITE(6,87)
     WRITE(6,88)FEQP


2.0*(TSTFR+1.0)

I6)
     GO TO 127
CTR
*XHM2F)/2.0+1.0


SRF)
RMT)

IRROR HAS CENTRAL APERTURE WITH COMPLEX REFLECTI

LIMUU
6," LIMUU=",I6)


DES.******************************************
/2.0+1.0

.0

TOT,RNORM)


1
```

```
      DO 15 J=LIMLJ,LIMUJ
   15 SRAND=SRAND+RNORM(J)
      CRAND(I)=SRAND/SQRT(XN
      IF(WRCRN .NE. C.0) WR
   20 CONTINUE
  122 DO 108 I=1,NTOT
      U (I)=CMPLX(0.0,0.0)
      UP(I)=CMPLX(0.0,0.0)
  108 CONTINUE
      ARG=SQRT(XINTS)
      DO 110 I=LIML,LIMU
      U (I)=CMPLX(ARG,0.0)
  110 CONTINUE
      YSEED=ISEED
      IF(RANST)102,103,102
  102 DO 104 I=LIML,LIMU
      J=I-LIML
      IF(J .LE. 10 )WRITE(6,
  107 FORMAT(1X,2E30.20)
      CALL GGUBS(ISEED,1,RAN
      ARG=(2.0*RAND-1.0)*PI*
      U (I)=U (I)*CEXP(CMPLX
  104 CONTINUE
      IF(XSPAM)119,103,118
  118 NMID=XMID
      DO 117 I=LIML,NMID
      LLL=NTOT-I+1
      U (I)  =(U (I) + XSPAM
      U (LLL) = XSPAM * U (I
  117 CONTINUE
  103 IF(BMTLT)106,109,106
  106 DO 105 I=LIML,LIMU
      XI=I
      ARG=(XI-XMID)/XNMIR*2.
      U (I)=CEXP(CMPLX(C.0,A
  105 CONTINUE
  109 IF(XG1-XG2)121,120,121
  120 OFST1=EPSL*XNMIR/2.0*(
      OFST2=OFST1
      GO TO 128
  121 XMAGRT=XMAG1*XMAG2
      OFST1=EPSL*XNMIR/2.0*(
      OFST2=0.0
C**********START A ROUND
  128 CONTINUE
      SU1AM=0.C
      DO 129 I=LIML,LIMU
      SU1AM=SU1AM+U(I)*CCNJG
  129 CONTINUE
      SAVU1=U(ITEST)
      IF(PHAM1 .NE. 0.0)CALL
      CALL PROPCB(U,NTOT,XNF
      IF((PLLP2 .GT. 0.0) .A
     1 (STOPT .GE. STP))) CA
C*****INTERPOLATE TO GET U2P
      CALL        INTRP(U,U P
C********RIGROD-TYPE GAIN AT
```

95

END
DATE
FILMED
2-84
DTIC
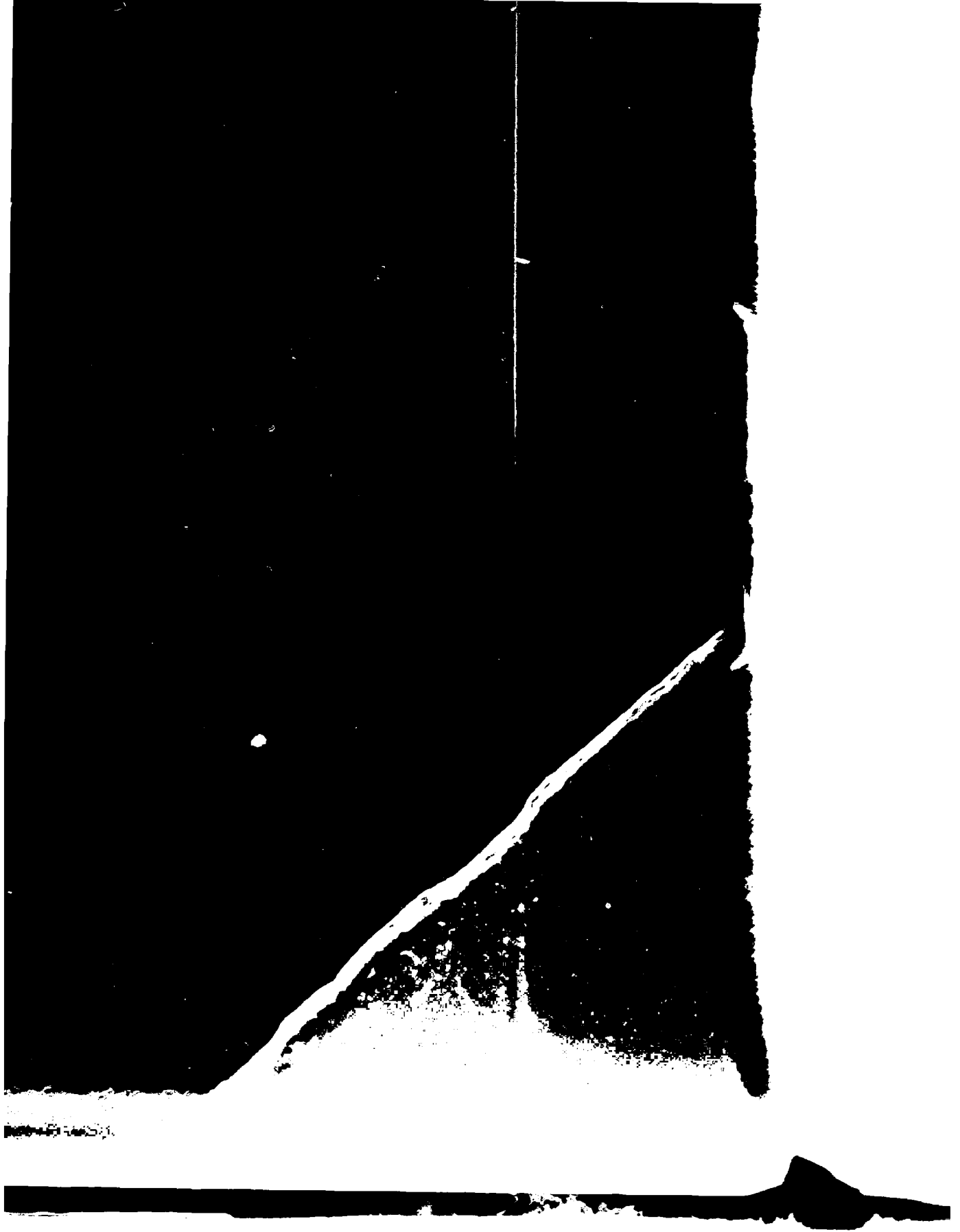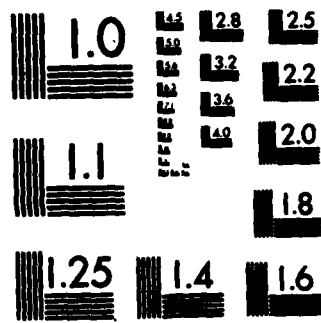
MICROCOPY RESOLUTION TEST CHART

NATIONAL BUREAU OF STANDARDS-1963-A

```
      IF(GL)131,135,131
  131 CALL        GAINM2(U P,NTOT,NMIR,GL,GDGLP,GNOFS)
C*****PROPAGATE TO MIRROR 1.*****************************************
  135 IF(RNPH2)30,36,30
   30 DO 35 I=LIML,LIMU
      ARG=CRAND(I)*RNPH2
      U P(I)=U P(I)*CEXP(CMPLX(0.0,ARG))
   35 CONTINUE
   36 CONTINUE
      SU2PAM=0.0
      DO 141 I=LIML,LIMU
  141 SU2PAM=SU2PAM+UP(I)*CONJG(UP(I))
      XDEN=LIMU-LIML+1
      AVFLX=SU2PAM/XDEN
      DO 140 I=1,NTOT
      IF(PRDGS .GT. 0.0)WRITE(6,201)I,UP(I)
  201 FORMAT(' AT 140 UP(',I6,')=',2E20.12)
  140 U(I)=U P(I)
      IF(PHAM2 .NE. 0.0)CALL PHSEM(PHAM2,PHCY2,NMIR,NTOT,U)
      XINAMP=SQRT(XININT)
      IF(XHMM2F .EQ. 0.0) GO TO 1044
      IF(LIMLL .GT. LIMUU) GO TO 1044
      DO 1043 I=LIMLL,LIMUU
      U(I)=U(I)*CFKTR
      IF(XININT .EQ. 0.0)GO TO 1043
      XI=I
      ARG=(XI-XMID)/XNMIR*2.0
      DLPH =PI*FRINF*ARG**2 + (XMITR-1.0) * RTPHS
      DLPHI = DLPH + (XI-XMID)/XNMIR*2.0*PI*BMTIN
      ARGC=COS(DLPHI)
      ARGS=SIN(DLPHI)
      CARP=CMPLX(ARGC,-ARGS)
      UINCR=XINAMP*CARP
      WRITE(6,1060)I,UINCR,DLPH,DLPHI
 1060 FORMAT(1X,I4,4E20.12)
      U(I) = U(I) + UINCR
 1043 CONTINUE
 1044 CONTINUE
 1045 CALL PROPCB(U,NTOT,XNF2T,XPAVG)
      IF(((PLLP1.GT. 0.0) .AND. ((XNITR .EQ. XPITR) .OR.
     1 (STOPT .GE. STP))) .OR.(PLLP1 .GT.1.0))CALL NFLPP(U,1,NTOT,PA112,
     21,INCPL,XMITR)
      IF(CFFLD .GT. 1.0)CALL FRFLD1(U      ,NTOT,NMIR,EPSL,XMAG2,A10A2,
     1XMITR,IMXFF,FFMAX,CFFLD,FNFCS,SPCLFF,FRCMSK)
C*****INTERPOLATE TO GET U P, I.E. AMPLITUDE RECEIVED AT MIRROR 1.*******
      CALL        INTRP(U,U P,LIML,LIMU,OFST1,A10A2,XNTOR,XMAG2)
C*******GET POWER RATIOS*****
      SU1PAM=0.0
      DO 145 I=LIML,LIMU
  145 SU1PAM=SU1PAM+U P(I)*CONJG(U P(I))
      SUTAM = 0.0
      DO 144 I=1,NTOT
  144 SUTAM = SUTAM + U(I) * CONJG(U(I))
      OUTCP = 1.0 -(SU1PAM/SUTAM * A10A2)
      GAMRT=SU1PAM/SU1AM
      SAVU1P=UP(ITEST)
C*****GET COMPLEX RATIOS OF AMPLITUDES AT MIRROR CENTERS.****************
```

```
      RAT1=SAVU1P/SAVU1
      ARG=AIMAG(RAT1)/REAL(RAT1)
      RAT1PH=ATAN(ARG)
      RAT1AM=CABS(RAT1)
      WRITE(6,61)XMITR,RAT1AM,RAT1PH,GAMOT,AVFLX,OUTCP
      TEST=RAT1AM/RAT1TS-1.0
      RAT1TS=RAT1AM
      AUTS=ABS(TEST)
      IF(AUTS-CVTST)159,159,158
  158 STOPT=0.0
      GO TO 160
  159 STOPT=STOPT+1.0
  160 CONTINUE
C******CALCULATED VALUE OF TVBQL IS RATIO OF CENTRAL FAR-FIELD
C******INTENSITY ARISING FROM GEOMETRIC-OPTICS PORTION OF BEAM TO
C******VALUE WHICH WOULD RESULT IF OUTPUT WERE UNIPHASE.
      IF((TVBQ .GT. 0.0) .AND. ((XN1TR .EQ. XMITR) .OR.
     1(STOPT .GT. 1.0))) CALL BQUAL(NTOT,NMIR,U)
      IF(STOPT- STOPN)169,190,190
  169 IF(XN1TR-XMITR)99, 191,170
  170 XMITR=XMITR+1.0
C******RENEW U (I)            FOR NEXT ITERATION.**********************
      IF(GL)174,173,174
  173 DO 172 I=1,NTOT
      U (I)=U P(I)/RAT1
      IF(PRDGS .GT. 0.0)WRITE(6,202)I,UP(I)
  202 FORMAT(' AT 172 UP(',I6,')=',2E20.12)
  172 CONTINUE
      GO TO 176
  174 DO 175 I=1,NTOT
      U (I)=U P(I)
  175 CONTINUE
  176 GO TO 128
  190 WRITE(6,70)
      GO TO 192
  191 WRITE(6,71)
  192 CONTINUE
C******OPTIONAL FAR-FIELD CALCULATION.*******************************
      IF(CFFLD .GT. 0.0)CALL FRFLD1(U      ,NTOT,NMIR,EPSL,XPAG2,A10A2,
     1XMITR,IMXFF,FFMAX,CFFLD,FNFCS,SPCLFF,FRCMSK)
      IF (CFFLD .GT. 1.0) CALL MFLPP(IMXFF,FFMAX,XMITR,ISKMF,
     1XNF2,XPAG1,EPSL,XNMIR,YSEED,PCHMF)
      GO TO 1
   99 WRITE(6,78)
 9001 STOP
      END
      SUBROUTINE PROPCB(U,NTOT,XNFT,XPAVG)
C****DOES COLLIMATED BEAM PROPAGATION OF COMPLEX ARRAY U, WITH NTOT
C****MESH POINTS. XNFT IS TOTAL FRESNEL NUMBER. XPAVG IS NUMBER OF
C****POINTS USED IN AVERAGING OF PROPAGATION KERNEL(NOMINALLY UNITY).
      LEVEL 2, U
      DIMENSION WORK(100),NN(1)
      DIMENSION U(NTOT)
      COMPLEX U,FFTC
      DATA PI/3.1415926536/
      NN(1)=NTOT
      XNTOT=NTOT
```

```
      XHTOT=NTOT/2
      NPAVG=XPAVG
      FACT=1.C/(16.G*PI*XNFT)
      CALL FOURT(U,NN,1,+1,1,WORK)
      DO 132 I=1,NTOT
      XI=I
      FFTC=CMPLX(C.0,0.C)
      DO 120 J=1,NPAVG
      X2JM1=2*J-1
      XII=XHTOT-XI+1.5-X2JM1/2.0/XPAVG
      XASQ=(XHTOT-ABS(XII))**2
      PSQ=4.0*PI**2*XASQ
      ARG=PSQ*FACT
      ARGC=COS(ARG)
      ARGS=SIN(ARG)
  12C FFTC=FFTC+CMPLX(ARGC,-ARGS)
      FFTC=FFTC/XPAVG
  132 U(I)=U(I)*FFTC
      CALL FOURT(U,NN,1,-1,1,WORK)
      DO 134 I=1,NTOT
  134 U(I)=U(I)/XNTOT
      RETURN
      END
      SUBROUTINE INTRP(U,UP ,LIML,LIMU,OFST ,AROAS,XNTOR,XMAG )
C***BESSEL FORMULA FOR INTERPOLATION BY HALVES. SCARBORO P 85 EQ VI.
      LEVEL 2, U,UP
      COMPLEX U(1),UP(1),CINT1,CINT2,CINT3,VAL
      ARG=ABS(XMAG)
      RTPAG=SQRT(ARG)
      XMID=(FLOAT(LIML)+FLOAT(LIMU))/2.C
      DO 136 I=LIML,LIMU
      XI=I
      ARG=(XI-XMID-OFST )/XMAG +AROAS+XMID
      IARG=ARG
      XIARG=IARG
      FRACT=ARG-XIARG
      VFRAC=FRACT-0.5
      CINT1=U(IARG+1)-U(IARG)
      VAL=(U(IARG)+U(IARG+1))/2.0+CINT1*VFRAC
      IF(XNTOR-2.0)139,138,137
  137 CINT3=U(IARG+2)-3.0*U(IARG+1)+3.C*U(IARG)-U(IARG-1)
      VAL=VAL+CINT3/6.0*VFRAC*(VFRAC**2-0.25)
  138 CINT2=(U(IARG+2)-U(IARG+1)-U(IARG)+U(IARG-1))/2.C
      VAL=VAL+CINT2/2.0*(VFRAC**2-0.25)
  139 UP (I)=VAL
  136 UP (I)=UP (I)/RTMAG
      RETURN
      END
      SUBROUTINE PHSEM(PHAM,PHCV,NMIR,NTOT,U)
      LEVEL 2, U
      COMPLEX U(NTOT),CVAR ,PHSE
      DATA PI/3.1415926536/
      XNTOT=NTOT
      XNMIR=NMIR
      XMID=(XNTOT+1.0)/2.3
      DO 117 I=1,NTOT
      XI=I
```

```
      XARG =(XI-XMID)/XNMIR*PI*PHCV *2.L
      YARG =PHAM *(COS(XARG )-1.0)
      CVAR =CMPLX(C.0,YARG )
      PHSE =CEXP(CVAR )
      U(I)=U(I)*PHSE
  117 CONTINUE
      RETURN
      END
      SUBROUTINE NFLPP(CU,NMIN,NMAX,PA1I2,IPOS,INCR,XNITR)
      LEVEL 2, CU
      DIMENSION GRAPH(101)
      COMPLEX CDENM,CARG
      COMPLEX CU(NMAX)
   76 FORMAT(1H0)
   77 FORMAT(1H1)
   79 FORMAT(64X,8HPOSITION,I3)
   80 FORMAT(19X,3H0.0,32X,'XXX  RELATIVE   0.5  INTENSITY   XXX',
     131X,3H1.0)
   81 FORMAT(19X,3H0.0,32X,'XXX  RELATIVE   0.5  AMPLITUDE   XXX',
     131X,3H1.0)
   85 FORMAT(18X,5H-PI/2,33X,'++ RELATIVE   0.0  PHASE ++',36X,5H+PI/2)
   89 FORMAT(63X,9HITERATION,I4)
  111 FORMAT(20X,101A1)
  112 FORMAT(13X,I5,2X,101A1)
      DATA PI/3.141562654/
      DATA BLANK/1H /,DOT/1H./,X/1HX/,ZERO/1H0/,PLUS/1H+/
      NGRAPH=101
      XNGRM1=NGRAPH-1
C********PRINT HEADING
      WRITE(6,77)
      ITER=XNITR
      WRITE(6,89)ITER
      WRITE(6,76)
      WRITE(6,79)IPOS
      WRITE(6,76)
      IF(PA1I2 .LE. 1.0)GO TO 7
      WRITE(6,80)
      GO TO 8
    7 WRITE(6,81)
    8 WRITE(6,76)
      WRITE(6,85)
      WRITE(6,76)
      DO 10 I=1,NGRAPH
   10 GRAPH(I)=BLANK
      DO 11 I=1,NGRAPH,10
   11 GRAPH(I)=DOT
      WRITE(6,111)GRAPH
      WRITE(6,111)GRAPH
      DO 15 I=1,NGRAPH
   15 GRAPH(I)=DOT
      WRITE(6,111)GRAPH
      DO 16 I=1,NGRAPH
   16 GRAPH(I)=BLANK
C******GET NORMALIZATION
      XMAX=0.0
      DO 30 I=NMIN,NMAX
      PARG=CU(I)*CONJG(CU(I))
```

100

```
      IF(RARG .GT. XMAX)XMAX=RARG
   30 CONTINUE
      XMAX=SQRT(XMAX)
      ICNTR=(NMIN+NMAX)/2
      PHSE =ATAN(AIMAG(CU(ICNTR))/REAL(CU(ICNTR)))
      CARG=CMPLX(0.0,PHSE)
      CDENM=XMAX*CEXP(CARG)
C******SET UP MAIN PLOT LOOP
      DO 200 I=NMIN,NMAX,INCR
      GRAPH(NGRAPH)=DOT
        CARG=CU(I)/CDENM
        PHSE=ATAN(AIMAG(CARG)/REAL(CARG))
        AORI=CABS(CARG)
        IF(PA1I2 .GT. 1.0)AORI=AORI**2
C********PRINT AN X
        J=AORI*XNGRM1 +1.0
        IF(J .GT. NGRAPH) J=NGRAPH
        GRAPH(J)=X
        K=XNGRM1/2.0+PHSE/PI*XNGRM1+1.0
        IF(K .LT. 1) K=1
        IF(K .GT. NGRAPH) K=NGRAPH
      GRAPH(K)=PLUS
      GRAPH(1)=DOT
      WRITE(6,112)I,GRAPH
      GRAPH(J)=BLANK
      GRAPH(K)=BLANK
  200 CONTINUE
      DO 211 I=1,NGRAPH
  211 GRAPH(I)=DOT
      WRITE(6,111)GRAPH
      DO 212 I=1,NGRAPH
  212 GRAPH(I)=BLANK
      DO 213 I=1,NGRAPH,10
  213 GRAPH(I)=DOT
      WRITE(6,111)GRAPH
      WRITE(6,111)GRAPH
      RETURN
      END
      SUBROUTINE GAINM2(U2P,NTOT,NMIR,GLC,QDGLP,GNOFS)
C****SMALL-SIGNAL GAIN IS GLC AT CENTER AND REDUCES QUADRATICALLY TO
C     GLC*(1.0-QDGLP) AT EDGES(PROVIDED GNOFS=0.0).  IF GNOFS .NE. 0.0,
C     CENTER OF QUADRATIC GAIN PROFILE IS SHIFTED BY THE FRACTION GNOFS
C     OF THE HALF-WIDTH OF MIRROR 2.
      LEVEL 2, U2P
      COMPLEX U2P(NTOT)
      XNMIR=NMIR
      XNTOT=NTOT
      XMID=(XNTOT+1.0)/2.0
      LIML=(NTOT-NMIR)/2+1
      LIMU=NTOT-LIML+1
      DO 2045 I=LIML,LIMU
      IF(QDGLP .EQ. 0.0)GO TO 7
      XXMID=XMID-GNOFS*(XNMIR/2.0)
      XI=I
      BRG=((XI-XXMID)/XNMIR*2)**2
      GL=GLC*(1.0-BRG*QDGLP)
      GO TO 8
```

101

```fortran
    7 GL=GLC
    9 BET1=U2P(I)*CONJG(U2P(I))
      ICNT=1
      BET4=BET1
    1 SAVE=BET4
      BET4=GL+BET1-0.5*ALOG(BET4/BET1)
      BET4=(BET4+SAVE)/2.0
      TEST=ABS(BET4-SAVE)
C              TEST MADE RELATIVE ON 1-31-83
               TEST=TEST/SAVE
      IF(TEST-C.00001)20,20,10
   10 ICNT=ICNT+1
      IF(ICNT-50)17,100,100
   17 IF(BET4)100,100,1
  100 ICNT=1
      BET4=BET1
  101 SAVE=BET4
      XARG=(GL+BET1-BET4)*2.0
      BET4=BET1*EXP(XARG)
      BET4=(BET4+SAVE)/2.0
      TEST=ABS(BET4-SAVE)
               TEST=TEST/SAVE
      IF(TEST-0.00001)20,20,110
  110 ICNT=ICNT+1
      IF(ICNT-50)101,18,18
   18 WRITE(6,83)GL,BET1,BET4
   83 FORMAT(1X,15HPROBLEM IN BET4,5F10.5)
      STOP
   20 ARG=SQRT(BET4)
 2045 U2P(I)=U2P(I)/CABS(U2P(I))*ARG
      RETURN
      END
      SUBROUTINE BQUAL(NTOT,NMIR,U)
      LEVEL 2, U
      COMPLEX U(NTOT),CARG
      XNMIR=NMIR
      LIML=(NTOT-NMIR)/2+1
      LIMU=NTOT-LIML+1
      CARG=CMPLX(0.0,0.0)
      RARG=0.0
      XINTS=0.0
      DO 10 I=LIML,LIMU
      CARG=CARG+U(I)
      RARG=RARG+CSQRT(U(I)*CONJG(U(I)))
      XINTS = XINTS + U(I)*CONJG(U(I))
   10 CONTINUE
      TVBQL=CARG*CONJG(CARG)/RARG**2
      WRITE(6,90)TVBQL
   90 FORMAT(1H0,6HTVBQL=,F10.5)
      CARG=CARG/XNMIR
      XINTS=XINTS/XNMIR
      TVBQT = CARG * CONJG(CARG)/XINTS
      WRITE(6,91)TVBQT
   91 FORMAT(' TVBQT=',F10.5)
      RETURN
      END
      SUBROUTINE FRFLD1 (UNFLD,NTOT,NMIR,EPSL,XMAG2,A10A2,XMITR,
```

102

```
      1IMXFF,FFMAX,CFFLD,FNFCS,SPCLFF,FRCMSK)
C******TEMPORARY CHANGES HAVE BEEN MADE ON 02-12-81 IN ORDER TO TREAT
C******PROPAGATION FROM ONE HALF OF FULL OUTPUT APERTURE.
C
C******NTOTH IS HALF OF NTOT.
C
C******XNMIRH IS HALF OF XNMIR.
C
C******UPPER LIMITS OF SUMMATION CHANGED FROM NTOT TO NTOTH AT FR2037 AND
C******FR2063.   XNMIRH REPLACED XNMIR AT FR2055,FP2056,AND FR2081.
C******ALSO FAKTR  AT FR2022+1 AND FR2025 AND FR2100
      LEVEL 2, UNFLD
      DIMENSION UNFLD(NTOT)
      DIMENSION IMXFF(200),FFMAX(200)
      DIMENSION GRAPH(101), FFI(101)
      COMPLEX CFCN,FFFCT,AFFAM,BFFAM,AMCPX
      COMPLEX UNFLD
      COMPLEX CFCTRF
      DATA PI/3.141592654/
   76 FORMAT(1H0)
   77 FORMAT(1H1)
  111 FORMAT(20X,101A1)
  112 FORMAT(1X, F10.5, 4X, I3, 2X, 101A1)
      DATA PI/3.141592654/
      DATA BLANK/1H /,DOT/1H./,X/1HX/
      NFFLD=101
      XNMIR=NMIR
      XNTOT=NTOT
      FACTR=XMAG2/A10A2
      OFFST=EPSL*XNMIR/2.0*(FACTR-1.0)/FACTR
      XMID=(XNTOT+1.0)/2.0
      X2=XMID-OFFST-XNMIR/2.0/FACTR
      X3=XMID-OFFST+XNMIR/2.0/FACTR
      NMDFF=(NFFLD+1)/2
      FAKTR=1.0
      IF(SPCLFF .EQ. 1.0)FAKTR=2.0/(1.0-A10A2)
      IF(SPCLFF .EQ. 2.0)FAKTR=1.0/FRCMSK
      IF(SPCLFF .EQ. 2.0)FACTR=1.0E10
      XCNTR = XNTOT/2.0
      IF(SPCLFF .EQ. 1.0)XCNTR=XCNTR-XNMIR/4.0*(1.0+1.0/FACTR)
      XNMI = XNMIR
      XNMIRH=XNMIR/2.0
      IF(SPCLFF .GT. 0.0)XNMI = XNMIRH
      LIMML=1
      LIMMU = NTOT
      NTOTH=NTOT/2
      IF(SPCLFF .EQ. 1.0)LIMMU = NTOTH
      IF (SPCLFF .NE. 2.0)GO TO 777
      XMIDL=XNTOT/2.0 - XNMIR/4.0*(1.0+A10A2)
      IRGMSK = XNMIR*FRCMSK/2.0
      LIMML= XMIDL - IRGMSK
      LIMMU= XMIDL + IRGMSK
      XNMI = LIMMU - LIMML + 1
      WRITE(6,80)IRGMSK,LIMML,LIMMU,XNMI
   80 FORMAT(3I6,F10.1)
  777 CONTINUE
      DO 360 I=1,NFFLD
```

```
      XARG=1-NPDFF
      THETP=XARG/10.0*FAKTR
C*****FAR-FIELD ANGLE IS IN UNITS OF LAMBDA/WIDTH.  WIDTH IS GEOMETRIC--
C*****OPTICS SIZE OF EMITTED BEAM, I. E. WIDTH OF LAST REFLECTING********
C*****(LARGER FOR CONFOCAL CASE) MIRROR TIMES MAGNIFICATION IN**********
C*****PROPAGATING PAST OBSCURING MIRROR TO FOCUSING MIRROR(IF ANY).*****
      ARG=-THETP*2.0*PI/XNMIR
      ARGS=SIN(ARG)
      ARGC=COS(ARG)
      CFCN=CMPLX(ARGC,ARGS)
      FFFCT=CMPLX(1.0,0.0)
      AFFAM   =CMPLX(0.0,0.0)
      BFFAM   =CMPLX(0.0,0.0)
      DO 350 J=LIMML,LIMMU
      XJ=J
      XJ=XJ-0.5
      CFCTRF = CMPLX(1.0,0.0)
      IF(FNFCS .EQ. 0.0)GO TO 302
      ARGPH = ((XCNTR-XJ)/XNMIR*2.0)**2*PI*FNFCS
      ARGCF = COS(ARGPH)
      ARGSF = SIN(ARGPH)
      CFCTRF = CMPLX(ARGCF,+ARGSF)
  302 FFFCT=FFFCT*CFCN
      FCTR=0.0
      IF(XJ-X2+1.0)320,320,310
  310 IF(XJ-X2)311,311,312
  311 FCTR=XJ+1.0-X2
      GO TO 318
  312 IF(XJ-X3+1.0)313,314,314
  313 FCTR=1.0
      GO TO 318
  314 IF(XJ-X3)315,320,320
  315 FCTR=X3-XJ
  320 CONTINUE
  318 BFFAM   =BFFAM    +FFFCT*UNFLD(J)*FCTR * CFCTRF
      AFFAM   =AFFAM    +FFFCT*UNFLD(J)*CFCTRF
  350 CONTINUE
      AFFAM=AFFAM/XNMI
      BFFAM=BFFAM/XNMI
      AMCPX=AFFAM-BFFAM
      FFI(I)=REAL(AMCPX)**2+AIMAG(AMCPX)**2
  360 CONTINUE
C*****CALCULATE AVERAGE NEAR-FIELD POWER.***************************
      ASQNF=0.0
      BSQNF=0.0
      DO 352 J=LIMML,LIMMU
      XARG=REAL(UNFLD(J))**2+AIMAG(UNFLD(J))**2
      XJ=J
      XJ=XJ-0.5
      IF(XJ-X2+1.0)330,330,326
  326 IF(XJ-X2)321,321,322
  329 FCTR=XJ+1.0-X2
      GO TO 328
  322 IF(XJ-X3+1.0)323,324,324
  323 FCTR=1.0
      GO TO 328
  324 IF(XJ-X3)325,330,330
```

```
  325 FCTR=X3-XJ
  329 BSQNF=BSQNF+XARG*FCTR
  330 CONTINUE
      ASQNF=ASQNF+XARG
  352 CONTINUE
      PAVNF=ASQNF-BSQNF
      PAVNF=PAVNF/XNM1
      PAVNF=PAVNF/(1.0-1.0/FACTR)
      DEN=PAVNF*(1.0-1.0/FACTR)**2
      DO 370 I=1,NFFLD
      FFI(I)=FFI(I)/DEN
  370 CONTINUE
      ITER=XMITR
C******GET NORMALIZATION
      XMAX = 0.0
      IMXFF(ITER) = 1
      DO 30 I = 1, NFFLD
      IF(FFI(I) .GT.  XMAX) IMXFF(ITER) = I
      IF(FFI(I) .GT. XMAX) XMAX = FFI(I)
   30 CONTINUE
      FFMAX(ITER)  = XMAX
      IF(CFFLD .GT. 2.0)     GO TO 392
      FFINT=0.0
      DO 388 I=1,NFFLD
  388 FFINT=FFINT+FFI(I)
      FFINT=FFINT/10.0*FAKTR
      FFINT=FFINT*(1.0-1.0/FACTR)
      NGRAPH=101
      XNGRM1=NGRAPH-1
C********PRINT HEADING
      WRITE(6,77)
      WRITE(6,79)ITER
   79 FORMAT(63X,'ITERATION',I4)
      WRITE(6,78)
   78 FORMAT(      60X, 'FAR-FIELD INTENSITY')
      WRITE(6,76)
      DO 10 I=1,NGRAPH
   10 GRAPH(I)=BLANK
      DO 11 I=1,NGRAPH,10
   11 GRAPH(I)=DOT
      WRITE(6,111)GRAPH
      WRITE(6,111)GRAPH
      DO 15 I=1,NGRAPH
   15 GRAPH(I)=DOT
      WRITE(6,111)GRAPH
      DO 16 I=1,NGRAPH
   16 GRAPH(I)=BLANK
C******SET UP MAIN PLOT LOOP
      DO 200 I = 1, NFFLD
      GRAPH(1)=DOT
      GRAPH(NGRAPH)=DOT
      K = FFI(I)/XMAX * XNGRM1 + 1.0
        IF(K .LT. 1) K=1
        IF(K .GT. NGRAPH) K=NGRAPH
      GRAPH(K) = X
      WRITE(6,112) FFI(I), I, GRAPH
      GRAPH(K)=BLANK
```

```
203 CONTINUE
    DO 211 I=1,NGRAPH
211 GRAPH(I)=DOT
    WRITE(6,111)GRAPH
    DO 212 I=1,NGRAPH
212 GRAPH(I)=BLANK
    DO 213 I=1,NGRAPH,10
213 GRAPH(I)=DOT
    WRITE(6,111)GRAPH
    WRITE(6,111)GRAPH
    WRITE(6,391)PAVNF
391 FORMAT(1X,'PAVNF=',E15.5)
    WRITE(6,390)FFINT
390 FORMAT(1X,'FFINT=',E15.5)
392 CONTINUE
    RETURN
    END
    SUBROUTINE            MFLPP(IMXFF,FFMAX,XMITR,ISKNF,
   1XNF2,XMAG1,EPSL,XNMIR,YSEED,PCHMF)
    DIMENSION IMXFF(200),FFMAX(200)
    DIMENSION GRAPH(101)
    DATA BLANK/1H /,DOT/1H./,X/1HX/,ZERO/1H0/,PLUS/1H+/
 75 FORMAT('   MODE-FORMATION FAR-FIELD RESULTS.')
 76 FORMAT(1H )
 77 FORMAT(1H1)
 79 FORMAT('   XNF2=   ',F10.5,'   XMAG1=   ',F10.5,'   EPSL=
   1F10.5,'   XNMIR=   ',F10.1,'   YSEED=   ',F20.0)
 80 FORMAT(19X,3H0.0,37X,'XXX       IP/IO       XXX',37X,3H1.0)
 81 FORMAT(18X,4H-5.0,37X,'+++      THETA      +++',37X,3H5.0)
 85 FORMAT(2I9,5F10.5)
 86 FORMAT('   ITERATION  IMXFF   FFMAX(I)')
111 FORMAT(20X,101A1)
112 FORMAT(15X,I3,2X,101A1)
    ITER = XMITR
    WRITE(6,77)
    WRITE(6,75)
    WRITE(6,76)
    WRITE(6,86)
    WRITE(6,76)
    DO 100 I=1,ITER
    WRITE(6,85)I,IMXFF(I),FFMAX(I)
100 CONTINUE
    WRITE(6,77)
    WRITE(6,79)   XNF2,XMAG1,EPSL,XNMIR,YSEED
    WRITE(6,76)
    WRITE(6,80)
    WRITE(6,76)
    NGRAPH=101
    XNGRM1=NGRAPH-1
    DO 10 I=1,NGRAPH
 10 GRAPH(I)=BLANK
    DO 11 I=1,NGRAPH,10
 11 GRAPH(I)=DOT
    WRITE(6,111)GRAPH
    WRITE(6,111)GRAPH
    DO 15 I=1,NGRAPH
 15 GRAPH(I) = DOT
```

```
      WRITE(6,111)GRAPH
      DO 16 I=1,NGRAPH
   16 GRAPH(I)=BLANK
      DO 200 I=1,ITER
      GRAPH(1)=DOT
      GRAPH(NGRAPH)=DOT
      J = IMXFF(I)
      IF(J .GT. NGRAPH) J = NGRAPH
      GRAPH(J)=PLUS
      K = FFMAX(I)*XNGRM1+1.C
      IF(K .LT .1) K = 1
      IF(K .GT. NGRAPH) K = NGRAPH
      GRAPH(K)=X
      WRITE(6,112)I,GRAPH
      GRAPH(J)=BLANK
      GRAPH(K)=BLANK
      IF(ISKMF .EQ. 0) GO TO 200
      DO 190 IS=1,ISKMF
  190 WRITE(6,76)
  200 CONTINUE
      DO 211 I=1,NGRAPH
  211 GRAPH(I)=DOT
      WRITE(6,111)GRAPH
      DO 212 I=1,NGRAPH
  212 GRAPH(I)=BLANK
      DO 213 I=1,NGRAPH,10
  213 GRAPH(I)=DOT
      WRITE(6,111)GRAPH
      WRITE(6,111)GRAPH
      WRITE(6,76)
      WRITE(6,81)
      IF(PCHMF .LE. 0.0)GO TO 214
      WRITE(1,410)XMITR,XNF2,XMAG1,EPSL,XNMIR,YSEED
  410 FORMAT(5(F14.5/),F14.5)
      DO 300 I=1,ITER
      RCOUNT = I
      RMXFF = IMXFF(I)
      WRITE(1,400)RCOUNT,RMXFF,FFMAX(I)
  400 FORMAT(3F10.5)
  300 CONTINUE
  214 RETURN
      END
      SUBROUTINE FOURT(DATA,NN,NDIM,ISIGN,IFORM,WORK)
      LEVEL 2, DATA
C     DESCRIPTION
C         FOURT PERFORMS AN N-DIMENSIONAL FAST FOURIER TRANSFORM ON AN
C         N-DIMENSIONAL ARRAY OF COMPLEX DATA.  THE TRANSFORM PERFORMED
C         MAY BE EXPRESSED AS FOLLOWS --
C
C         TRANSFORM(J1,J2,....)=SUM(DATA(I1,I2,....)*W1**((I1-1)*(J1-1))
C                                                   *W2**((I2-1)*(J2-1))
C                                                   *...)
C         WHERE I1 AND J1 RUN FROM 1 TO NN(1), AND
C               I2 AND J2 RUN FROM 1 TO NN(2), ETC.
C         AND
C               W1 = EXP(ISIGN*2*PI*SQRT(-1)/NN(1)) , ETC.
C
```

```
C         FOR ONE DIMENSION, THE TRANSFORM IS PRECISELY
C
C         TRANSFORM(J1) = SUM(DATA(I1)*W1**((I1-1)*(J1-1)))
C
C         FOUR IS FASTEST WHEN THE NUMBER OF DATA VALUES IN EACH
C         DIMENSION IS A HIGHLY COMPOSITE (FACTORABLE) NUMBER.
C      INPUT
C         GIVEN AN N-DIMENSIONAL COMPLEX ARRAY OF DATA
C
C         DATA -- COMPLEX ARRAY IN WHICH THE DATA TO BE TRANSFORMED
C                 IS PLACED.  UPON RETURN TO CALLING PROGRAM DATA
C                 CONTAINS THE TRANSFORM VALUES.
C         NN    - INTEGER ARRAY GIVING THE (POSITIVE) NUMBER OF POINTS,
C                 OR VALUES, IN EACH DIMENSION, RESPECTIVELY.
C         NDIM  - NUMBER OF DIMENSIONS (INTEGER)  NDIM.GE.1
C         ISIGN - INTEGER GIVING DIRECTION OF TRANSFORM TO BE DONE.
C                 = -1 IMPLIES FORWARD
C                 = +1 IMPLIES BACKWARD
C         IFORM - INTEGER PARAMETER DESCRIBING THE FORM OF THE DATA.
C                 = 1 IMPLIES THE DATA IS COMPLEX (NON-TRIVIALLY).
C                 = 0 IMPLIES THE DATA IS ACTUALLY REAL.  I.E., THE
C                     IMAGINARY PART OF EACH COMPLEX ELEMENT OF DATA
C                     IS ZERO.  FOUR IS SIGNIFICANTLY FASTER WHEN
C                     IFORM=0.
C         WORK  - COMPLEX WORK ARRAY.  WORK MUST BE DIMENSIONED AS
C                 LARGE AS THE LARGEST DIMENSION OF DATA WHICH IS NOT
C                 A POWER OF TWO.  IF ALL DIMENSIONS OF DATA ARE
C                 POWERS OF TWO THEN WORK IS A DUMMY ARGUMENT.
C      OUTPUT
C         TRANSFORMED VALUES OF DATA ARRAY.IF COMBINED FORWARD AND
C         BACKWARD TRANSFORMS ARE MADE IN SEQUENCE,THE VALUES IN
C         THE DATA ARRAY ARE THE ORIGINAL VALUES MULTIPLIED BY
C         NN(1)*NN(2)* . . . NN(NDIM)
C      REMARKS
C         CONTROL DATA 6600 VERSION
C
C         CONSULT REFERENCE IN MAKING CHOICES OF TRANSFORMED VARIABLES
C         OR FREQUENCIES IN DOING CALCULATIONS IN THE TRANSFORMED
C         PLANE
C      REFERENCE
C         THREE FORTRAN PROGRAMS THAT PERFORM THE
C         COOLEY-TUKEY FOURIER TRANSFORM
C         N. M. BRENNER
C         M. I. T. LINCOLN LABORATORIES
C         TECHNICAL NOTE 1967-2
C         29 JULY 1967
C         AD 657019
C      SUBROUTINE FOURT(DATA,NN,NDIM,ISIGN,IFORM,WORK)
       DIMENSION DATA(1),NN(1),IFACT(32),WORK(1)
       TWOPI = 6.2831853071795
       RTHLF = 0.70710678118655
     1 NTOT=2
       DO 2 IDIM=1,NDIM
     2 NTOT=NTOT*NN(IDIM)
       NP1=2
       DO 910 IDIM=1,NDIM
       N=NN(IDIM)
```

```
      NP2=NP1*N
      IF(N.EQ.1)GO TO 900
   5  M=N
      NTWO=NP1
      IF=1
      IDIV=2
  10  IQUOT=M/IDIV
      IREM=M-IDIV*IQUOT
      IF(IQUOT-IDIV)50,11,11
  11  IF(IREM)20,12,20
  12  NTWO=NTWO+NTWO
      IFACT(IF)=IDIV
      IF=IF+1
      M=IQUOT
      GOTO 10
  20  IDIV=3
      INON2=IF
  30  IQUOT=M/IDIV
      IREM=M-IDIV*IQUOT
      IF(IQUOT-IDIV)60,31,31
  31  IF(IREM)40,32,40
  32  IFACT(IF)=IDIV
      IF=IF+1
      M=IQUOT
      GOTO 30
  40  IDIV=IDIV+2
      GOTO 30
  50  INON2=IF
      IF(IREM)60,51,60
  51  NTWO=NTWO+NTWO
      GOTO 70
  60  IFACT(IF)=M
  70  NON2P=NP2/NTWO
      ICASE=1
      IFMIN=1
      I1RNG=NP1
      IF(IDIM-4)74,100,100
  74  IF(IFORM)71,71,100
  71  ICASE=2
      I1RNG=NPC*(1+NPREV/2)
      IF(IDIM-1)72,72,100
  72  ICASE=3
      I1RNG=NP1
      IF(NTWO-NP1)100,100,73
  73  ICASE=4
      IFMIN=2
      NTWO=NTWO/2
      N=N/2
      NP2=NP2/2
      NTOT=NTOT/2
      I=1
      DO 80 J=1,NTOT
      DATA(J)=DATA(I)
  80  I=I+2
 100  IF(NON2P-1)101,101,200
 101  NP2HF=NP2/2
      J=1
```

```
      DO 150 I2=1,NP2,NP1
      IF(J-I2)121,130,130
121   I1MAX=I2+NP1-2
      DO 125 I1=I2,I1MAX,2
      DO 125 I3=I1,NTOT,NP2
      J3=J+I3-I2
      TEMPR=DATA(I3)
      TEMPI=DATA(I3+1)
      DATA(I3)=DATA(J3)
      DATA(I3+1)=DATA(J3+1)
      DATA(J3)=TEMPR
125   DATA(J3+1)=TEMPI
130   M=NP2HF
140   IF(J-M)150,150,141
141   J=J-M
      M=M/2
      IF(M-NP1)150,140,140
150   J=J+M
      GOTO 300
200   NWORK=2*N
      DO 270 I1=1,NP1,2
      DO 270 I3=I1,NTOT,NP2
      J=I3
      DO 260 I=1,NWORK,2
      IF(ICASE-3)210,220,210
210   WORK(I)=DATA(J)
      WORK(I+1)=DATA(J+1)
      GOTO 240
220   WORK(I)=DATA(J)
      WORK(I+1)=0.0
240   IFP2=NP2
      IF=IFMIN
250   IFP1=IFP2/IFACT(IF)
      J=J+IFP1
      IF(J-I3-IFP2)260,255,255
255   J=J-IFP2
      IFP2=IFP1
      IF=IF+1
      IF(IFP2-NP1)260,260,250
260   CONTINUE
      I2MAX=I3+NP2-NP1
      I=1
      DO 270 I2=I3,I2MAX,NP1
      DATA(I2)=WORK(I)
      DATA(I2+1)=WORK(I+1)
270   I=I+2
300   IF(NTWO-NP1)600,600,305
305   NP1TW=NP1+NP1
      IPAR=NTWO/NP1
310   IF(IPAR-2)350,330,320
320   IPAR=IPAR/4
      GOTO 310
330   DO 340 I1=1,I1RNG,2
      DO 340 K1=I1,NTOT,NP1TW
      K2=K1+NP1
      TEMPR=DATA(K2)
      TEMPI=DATA(K2+1)
```

```fortran
      DATA(K2)=DATA(K1)-TEMPR
      DATA(K2+1)=DATA(K1+1)-TEMPI
      DATA(K1)=DATA(K1)+TEMPR
  340 DATA(K1+1)=DATA(K1+1)+TEMPI
  350 MMAX=NP1
  360 IF(MMAX-NTWO/2)370,600,600
  370 LMAX=MAXC(NP1TW,MMAX/2)
      DO 570 L=NP1,LMAX,NP1TW
      M=L
      IF(MMAX-NP1)420,420,380
  380 THETA=-TWOPI*FLOAT(L)/FLOAT(4*MMAX)
      IF(ISIGN)400,390,390
  390 THETA=-THETA
  400 WR=COS(THETA)
      WI=SIN(THETA)
  410 W2R=WR*WR-WI*WI
      W2I=2.0*WR*WI
      W3R=W2R*WR-W2I*WI
      W3I=W2R*WI+W2I*WR
  420 DO 530 I1=1,I1RNG,2
      KMIN=I1+IPAR*M
      IF(MMAX-NP1)430,430,440
  430 KMIN=I1
  440 KDIF=IPAR*MMAX
  450 KSTEP=4*KDIF
      IF(KSTEP-NTWO)460,460,530
  460 DO 520 K1=KMIN,NTOT,KSTEP
      K2=K1+KDIF
      K3=K2+KDIF
      K4=K3+KDIF
      IF(MMAX-NP1)470,470,480
  470 U1R=DATA(K1)+DATA(K2)
      U1I=DATA(K1+1)+DATA(K2+1)
      U2R=DATA(K3)+DATA(K4)
      U2I=DATA(K3+1)+DATA(K4+1)
      U3R=DATA(K1)-DATA(K2)
      U3I=DATA(K1+1)-DATA(K2+1)
      IF(ISIGN)471,472,472
  471 U4R=DATA(K3+1)-DATA(K4+1)
      U4I=DATA(K4)-DATA(K3)
      GOTO 510
  472 U4R=DATA(K4+1)-DATA(K3+1)
      U4I=DATA(K3)-DATA(K4)
      GOTO 510
  480 T2R=W2R*DATA(K2)-W2I*DATA(K2+1)
      T2I=W2R*DATA(K2+1)+W2I*DATA(K2)
      T3R=WR*DATA(K3)-WI*DATA(K3+1)
      T3I=WR*DATA(K3+1)+WI*DATA(K3)
      T4R=W3R*DATA(K4)-W3I*DATA(K4+1)
      T4I=W3R*DATA(K4+1)+W3I*DATA(K4)
      U1R=DATA(K1)+T2R
      U1I=DATA(K1+1)+T2I
      U2R=T3R+T4R
      U2I=T3I+T4I
      U3R=DATA(K1)-T2R
      U3I=DATA(K1+1)-T2I
      IF(ISIGN)490,500,500
```

```
490 U4R=T3I-T4I
    U4I=T4R-T3R
    GOTO 510
500 U4R=T4I-T3I
    U4I=T3R-T4R
510 DATA(K1)=U1R+U2R
    DATA(K1+1)=U1I+U2I
    DATA(K2)=U3R+U4R
    DATA(K2+1)=U3I+U4I
    DATA(K3)=U1R-U2R
    DATA(K3+1)=U1I-U2I
    DATA(K4)=U3R-U4R
520 DATA(K4+1)=U3I-U4I
    KDIF=KSTEP
    KMIN=4*(KMIN-I1)+I1
    GOTO 450
530 CONTINUE
    M=M+LMAX
    IF(M-MMAX)540,540,570
540 IF(ISIGN)550,560,560
550 TEMPR=WR
    WR=(WR+WI)*RTHLF
    WI=(WI-TEMPR)*RTHLF
    GOTO 410
560 TEMPR=WR
    WR=(WR-WI)*RTHLF
    WI=(TEMPR+WI)*RTHLF
    GOTO 410
570 CONTINUE
    IPAR=3-IPAR
    MMAX=MMAX+MMAX
    GOTO 360
600 IF(NON2P-1)700,700,601
601 IFP1=NTWO
    IF=INON2
610 IFP2=IFACT(IF)*IFP1
    THETA=-TWOPI/FLOAT(IFACT(IF))
    IF(ISIGN)612,611,611
611 THETA=-THETA
612 WSTPR=COS(THETA)
    WSTPI=SIN(THETA)
    DO 650 J1=1,IFP1,NP1
    THETM=-TWOPI*FLOAT(J1-1)/FLOAT(IFP2)
    IF(ISIGN)614,613,613
613 THETM=-THETM
614 WMINR=COS(THETM)
    WMINI=SIN(THETM)
    I1MAX=J1+I1RNG-2
    DO 650 I1=J1,I1MAX,2
    DO 650 I3=I1,NTOT,NP2
    I=1
    WR=WMINR
    WI=WMINI
    J2MAX=I3+IFP2-IFP1
    DO 640 J2=I3,J2MAX,IFP1
    TWOWR=WR+WR
    J3MAX=J2+NP2-IFP2
```

112

```
      DO 630 J3=J2,J3MAX,IFP2
      JMIN=J3-J2+I3
      J=JMIN+IFP2-IFP1
      SR=DATA(J)
      SI=DATA(J+1)
      OLDSR=0.0
      OLDSI=0.0
      J=J-IFP1
620   STMPR=SR
      STMPI=SI
      SR=TWOWR*SR-OLDSR+DATA(J)
      SI=TWOWR*SI-OLDSI+DATA(J+1)
      OLDSR=STMPR
      OLDSI=STMPI
      J=J-IFP1
      IF(J-JMIN)621,621,620
621   WORK(I)=WR*SR-WI*SI-OLDSR+DATA(J)
      WORK(I+1)=WI*SR+WR*SI-OLDSI+DATA(J+1)
630   I=I+2
      WTEMP=WR*WSTPI
      WR=WR*WSTPR-WI*WSTPI
640   WI=WI*WSTPR+WTEMP
      I=1
      DO 650 J2=I3,J2MAX,IFP1
      J3MAX=J2+NP2-IFP2
      DO 650 J3=J2,J3MAX,IFP2
      DATA(J3)=WORK(I)
      DATA(J3+1)=WORK(I+1)
      I=I+1
650   I=I+2
      IFP1=IFP2
      IF(IFP1-NP2)610,700,700
700   GOTO(900,800,900,701),ICASE
701   NHALF=N
      N=N+N
      THETA=-TWOPI/FLOAT(N)
      IF(ISIGN)703,702,702
702   THETA=-THETA
703   WSTPR=COS(THETA)
      WSTPI=SIN(THETA)
      WR=WSTPR
      WI=WSTPI
      IMIN=3
      JMIN=2*NHALF-1
      GOTO 725
710   J=JMIN
      DO 725 I=IMIN,NTOT,NP2
      SUMR=(DATA(I)+DATA(J))/2.0
      SUMI=(DATA(I+1)+DATA(J+1))/2.0
      DIFR=(DATA(I)-DATA(J))/2.0
      DIFI=(DATA(I+1)-DATA(J+1))/2.0
      TEMPR=WR*SUMI+WI*DIFR
      TEMPI=WI*SUMI-WR*DIFR
      DATA(I)=SUMR+TEMPR
      DATA(I+1)=DIFI+TEMPI
      DATA(J)=SUMR-TEMPR
      DATA(J+1)=-DIFI+TEMPI
```

```
720 J=J+NP2
    IMIN=IMIN+2
    JMIN=JMIN-2
    WTEMP=WR+WSTPI
    WR=WR*WSTPR-WI*WSTPI
    WI=WI*WSTPR+WTEMP
725 IF(IMIN-JMIN)710,730,740
730 IF(ISIGN)731,740,740
731 DO 735 I=IMIN,NTOT,NP2
735 DATA(I+1)=-DATA(I+1)
740 NP2=NP2+NP2
    NTOT=NTOT+NTOT
    J=NTOT+1
    IMAX=NTOT/2+1
745 IMIN=IMAX-2*NHALF
    I=IMIN
    GOTO 755
750 DATA(J)=DATA(I)
    DATA(J+1)=-DATA(I+1)
755 I=I+2
    J=J-2
    IF(I-IMAX)750,760,760
760 DATA(J)=DATA(IMIN)-DATA(IMIN+1)
    DATA(J+1)=0.C
    IF(I-J)770,780,780
765 DATA(J)=DATA(I)
    DATA(J+1)=DATA(I+1)
770 I=I-2
    J=J-2
    IF(I-IMIN)775,775,765
775 DATA(J)=DATA(IMIN)+DATA(IMIN+1)
    DATA(J+1)=0.0
    IMAX=IMIN
    GOTO 745
780 DATA(1)=DATA(1)+DATA(2)
    DATA(2)=0.0
    GOTO 900
800 IF(I1RNG-NP1)805,900,900
805 DO 860 I3=1,NTOT,NP2
    I2MAX=I3+NP2-NP1
    DO 860 I2=I3,I2MAX,NP1
    IMIN=I2+I1RNG
    IMAX=I2+NP1-2
    JMAX=2*I3+NP1-IMIN
    IF(I2-I3)820,820,810
810 JMAX=JMAX+NP2
820 IF(IDIM-2)850,850,830
830 J=JMAX+NP0
    DO 840 I=IMIN,IMAX,2
    DATA(I)=DATA(J)
    DATA(I+1)=-DATA(J+1)
840 J=J-2
850 J=JMAX
    DO 860 I=IMIN,IMAX,NP0
    DATA(I)=DATA(J)
    DATA(I+1)=-DATA(J+1)
860 J=J-NP0
```

```
900 NP0=NP1
910 NPREV=N
    NP1=NP2
920 RETURN
    END
```

LIST OF SYMBOLS

a	active media dimension
a_1	feedback mirror half dimension
$\overline{B}$	magnetic induction vector
c	speed of light in vacuum
$\overline{D}$	electric displacement vector
d	laser aperture output dimension
$\overline{E}$	electric field vector
F	resonator waist scale parameter
F'	scaled resonator focus distance
F''	fluorescence
F_{eq}	equivalent Fresnel number
f	parabola focal length
f_1	feedback mirror focal length
f_2	primary mirror focal length
g, g_1, g_2	resonator "g" parameters
g_1', g_2'	statistical weights
$g(\nu)$	normalized absorption lineshape
$\overline{H}$	magnetic field vector
H_m	Hermite polynomial of order m
H_ℓ	Hermite polynomial of order ℓ
I, I_o, I', I_o'	intensity
K	Huygens kernel
k	propagation number

117

L	resonator mirror separation
ℓ	active media gain length
M	resonator magnification
m	mesh point size
m_1	feedback mirror (unless otherwise stated)
m_2	primary mirror (unless otherwise stated)
N_T	tube Fresnel number
N_1	lower laser level population
N_2	upper laser level population
n	Anan'ev round trip number
n'	diffraction limited round trip number
p	Fourier spatial frequency component in x coordinate
q	Fourier spatial frequency component in y coordinate
R_1	feedback mirror radius of curvature
R_2	primary mirror radius of curvature
S	resonator geometric outcoupling
T_x	Fourier transform in x coordinate
$T_{x,y}$	inverse Fourier transform in x and y coordinates
t_{spont}	spontaneous emission lifetime
U_o	lowest loss eigenfunction
$U_n,\ U_m,\ U_{m\ell}$	resonator eigenfunction
W_o	beam waist of symmetric confocal resonator
W	beam waist of a stable resonator
2α	laser beam dimension
$\gamma_o,\ g_o$	small signal gain

γ	saturable gain
δ_{nm}	Kronecker delta
ϵ	electric permittivity
η	index of refraction
θ_n	round trip angular radiation distribution
λ_o	lowest loss eigenvalue
λ_m	complex eigenvalue
λ	wavelength of light
μ	magnetic permeability
ν	photon frequency
τ	time after threshold
ψ	complex amplitude
$\hat{\psi}$	transformed complex amplitude
ω	radial frequency

REFERENCES

1. Siegman, A. E., Proc. IEEE 53, 277(1965).

2. Zemskov, K. I., et al., Sov. J. Quant. Electron. 4, 474(1974).

3. Deka, B. K. and P. E. Dyer, Opt. Commun. 18, 462(1976).

4. Hargrove, R. S., R. Grove, and T. Kan, IEEE J. Quantum Electron. QE-15, 1228(1979).

5. Anan'ev, Y. A., Sov. J. Quant. Electron. 5, 615(1975).

6. Fox, A. G., and T. Li, Bell Syst. Tech. J. 40, 453(1961).

7. Prokhorov, A. M., Sov. Phys. JETP 7, 1140(1958).

8. Schawlow, A. L. and C. H. Townes, Phys. Rev. 29, 1940(1958).

9. Kogelnik, H. and T. Li, Appl. Opt. 5, 1550(1966).

10. Boyd, G. D. and J. P. Gordon, Bell Syst. Tech. J. 40, 489(1961).

11. Boyd, G. D. and H. Kogelnik, Bell Syst. Tech. J. 41, 1347(1962).

12. Siegman, A. E., Laser Focus, 42 (May,1971).

13. Anan'ev, Y. A., Sov. J. Quant. Electron. 1, 565(1972).

14. Krupke, W. F. and W. R. Sooy, IEEE J. Quantum Electron. QE-5, 575(1969).

15. Sigemna, A. E., Appl. Opt. 13, 353(1974).

16. Horwitz, P., J. Opt. Soc. Am. 63, 1528(1973).

17. Rensch, D. B. and A.N. Chester, Appl. Opt. 12, 997(1973).

18. Sanderson, R. L. and W. Streifer, Appl. Opt. 8, 2129(1969).

19. Rensch, D. B. and A. N. Chester, J. Opt. Soc. Am. 62, 718A(1972).

20. Moore, G. T. and R. J. McCarthy, J. Opt. Soc. Am. 67, 228(1977).

21. Horwitz, P., Appl. Opt. 15, 167(1976).

22. Sziklas, E. A. and A. E. Siegman, Proc. IEEE 62, 410(1974).

23. Siegman, A. E. and H. Y. Miller, Appl. Opt. 9, 2730(1970).

24. Siegman, A. E., An Introduction to Lasers and Masers, McGraw-Hill 1971.

25. Lax, M., W. Louisell, and W. B. McKnight, Phys. Rev. 11, 1365(1975).

26. Sutton, G. W., M. M. Weiner, and S. A. Mani, Appl. Opt. 15, 2228(1976).

27. Freiburg, R. J., P. P. Chenausky, and C. J. Buczek, IEEE J. Quantum Electron. QE-8, 882(1972).

28. Phillips, E. A., J. P. Reilly, and D. B. Northam, Appl. Opt. 15, 2159(1976).

29. Sziklas, E. A. and A. E. Siegman, Appl. Opt. 14, 1874(1975).

30. Weiner, M. M., IEEE J. Quantum Electron. QE-13, 803(1977).

31. Goldhar, J., W. R. Rapoport, and J. R. Murray, IEEE J. Quantum Electron. QE-16, 235(1980).

32. Deka, B. K. and P. E. Dyer, IEEE J. Quantum Electron. QE-14, 661(1978).

33. Bigio, I. and M. Slatkine, Opt. Lett. 7, 19(1982).

34. Nicols, D. B., K. H. Wrolstad, and J. D. McClure, J. Appl. Phys. 45, 5360(1974).

35. Cason, C., A. H. Werkheiser, W. Otto, and R. W. Jones, J. Appl. Phys. 48, 2531(1977).

36. Cason, C., G. J. Dezenberg, and R. J. Huff, Appl. Phys. Let. 23, 110(1973).

37. Scheps, R., R. O. Hunter, and J. R. Oldenettel, Rev. Sci. Instrum. 50, 1054(1979).

38. Chernin, D. P., et al., "Optics Technology Program for Advanced High Power Visible Lasers," Report No. MLR-892, Maxwell Laboratories, Inc., 30 April 1980.

39. Svelto, O., Principles of Lasers, Plenum Press, New York, 1978.

40. Wood, O. R., Proc. IEEE 62, 355(1974).

41. Patel, C.K.N., Phys. Rev. 136, A1187(1964).

42. Patel, C.K.N., P. K. Tien, and J. H. McFee, Appl. Phys. Lett. 7, 290(1965).

43. Yariv, A., Introduction to Optical Electronics, 2nd ed., Holt, Rinehart, Winston, New York, 1976.

44. Nighan, W. L., Phys. Rev. A A2, 1989(1970).

45. Kast, S. J. and C. M. Cason, J. Appl. Phys. 44, 1631(1973).

46. Bowden, C. M., J. F. Perkins, and R. A. Shatas, J. Vac. Sci. Technol. 10, 1000(1973).

47. Tillotsen, J. H. and J. Shannon, "Visible Laser Research Program," Report #MLR-783, Maxwell Laboratories, Inc., San Diego, CA, Feb 1978.

48. Fisher, C. H. and R. E. Center, J. Chem. Phys. $\underline{69}$, 2011(1978).

49. Jones, R. W., Phys. Lett. $\underline{93A}$, 472(1983).

50. Jones, R. W., "Transverse Mode Formation in Positive Branch Unstable Resonators," Paper given at the Annual Meeting of the Optical Society of America, Tucson, AR, 21 October 1982.

51. Jones, R. W. and J. F. Perkins, to be published in Applied Optics.

52. Asmus, J. F. and J. R. Oldenettel, private communication.

53. Jones, R. W., J. F. Perkins, and C. C. Shih, "Wave Optics Investigations of Transverse Mode Formation," Report TR-RH-82-4, US Army Missile Command, March 1982.

54. Siegman, A. E. and E. A. Sziklas, Appl. Opt. $\underline{14}$, 1874(1975).

55. Rigrod, W. W., J. Appl. Phys. $\underline{34}$, 2602(1963).

56. Rigrod, W. W., J. Appl. Phys. $\underline{36}$, 2487(1965).

57. Cooley, J. W. and J. W. Tukey, J. Math. Comput. $\underline{19}$, 297(1965).

58. Chan, C. H., Appl. Opt. $\underline{14}$, 2418(1975).

59. Perkins, J. F. and R. A. Shatas, Appl. Phys. $\underline{9}$, 343(1976).

60. Chen, L. W. and L. B. Felsen, IEEE J. Quantum Electron. $\underline{QE-9}$, 1102(1973).

61. Smith, M. J., Appl. Opt. $\underline{20}$, 1611(1981).

62. Lax, M., W. H. Louisell, and W. B. McKnight, J. Appl. Phys. $\underline{43}$, 3136(1972).

63. Perkins, J. F., private communication.

DISTRIBUTION

No. of
Copies

Lockheed Missile and Space Company
PO Box 504
ATTN: Mr. Roy Stewart   1
Sunnyvale, CA   94086

Lockheed Missile and Space Company
PO Box 1103, West Station
ATTN: Mr. Owne Hofer   1
Huntsville, AL   35807

McDonnell Douglas Astronautics Company
5301 Bolsa Avenue
ATTN: Dr. W. Boxich   1
Huntington Beach, CA   92647

General Electric Company
3198 Chestnut Street
ATTN: Mr. Bill East   1
Philadelphia, PA   19101

Bell Aerospace Textron
PC Box 1
ATTN: Dr. Wayne Solomon   1
Buffalo, NY   14240

Science Applications, Inc.
6600 Powers Ferry Road
Suite 220
ATTN: Mr. Harvey Ford   1
Atlanta, GA   30339

Science Applications, Inc.
Three San Pedro Park, Suite 212/206
2201 San Pedro Drive, NE
ATTN: Mr. Larry Pechham   1
Albuquerque, NM   87110

Navy High Energy Laser Project Office
Naval Sea Systems Command (PM22/PMS405)
ATTN: Mr. John P. Albertine   2
      LCDR Nanos
Washington, DC   20351

Westinghouse Electric Corporation
80 Holiday Office Center
ATTN: Charles Thompson   1
Huntsville, AL   35801

125

No. of
Copies

Braddock, Dunn & McDonald, Inc.
PO Box 9274
ATTN: Mr. Roger Hoppe   1
Albuquerque, NM 87119

Boeing Aerospace Company
PO Box 399
ATTN: Dr. Davis Nichols   1
Seattle, WA 98124

AVCO-Everett Research Laboratory
2385 Revere Beach Parkway
ATTN: Dr. George Sutton   1
      Dr. M. J. Smith   1
Everett, MA 02149

Cincinnati Electronics
2630 Glendale-Milford Road
ATTN: Mr. E. E. Cook   1
Cincinnati, OH 45241

Naval Research Laboratory
CODE 6540
ATTN: Dr. Stuart Searles   1
Washington D.C. 20375

Sperry Systems Management
1112 Church Street
ATTN: Mr. John Nickrehm   1
Huntsville, AL 35801

Director
US Army Ballistic Research Laboratory
ATTN: Mr. John McNeilly   1
Aberdeen Proving Ground, MD 21005

Director
Defense Advance Research Projects Agency/STO
1400 Wilson Boulevard
ATTN: Dr. Allan Pike   1
Arlington, VA 22209

Aerospace Corporation
PO Box 95085
ATTN: Mr. W. Warren   1
El Segundo, CA 90045

No. of
Copies

United Technologies Research Center
Optics and Applied Technology
ATTN: Dr. Frank Ebright   1
PO Box 2691
West Palm Beach, FL   33402

Commander
Air Force Weapons Laboratory
ATTN: AFWL/ARAO, COL James Mayo   1
       AFWL/ARAO, Dr. Diane Martin   1
Kirtland AFB, NM   87117

Maxwell Laboratories
8835 Balboa Avenue
ATTN: Dr. John F. Asmus   1
       Mr. Jerry R. Oldenettel   1
San Diego, CA   92123

Director
Defense Advanced Research Projects Agency
ATTN: LTC Rettig P. Beneditc, Jr.   1
1400 Wilson Blvd
Arlington, VA   22209

Pratt & Whitney Aircraft
PO Box 2691
ATTN: Mr. D. Witt   1
West Palm Beach, FL   33402

Rockwell International
6633 Canoga Ave
ATTN: Mr. John Wrubel   1
Canoga Park, CA   91304

Hughes Aircraft
Centenela and Teale Streets
ATTN: Mr. Bernard Skehan   1
Culver City, CA   90230

Charles Stark Draper Laboratory
555 Technology Square
ATTN: Mr. Juri Valge   1
Cambridge, MA   02139

W. J. Schafer Associates, Inc.
Clinton Building, Suite 408
2109 Clinton Avenue, West
ATTN: Dr. Jack Albers   1
Huntsville, AL   35805

No. of
Copies

Perkin-Elmer Corporation
Main Avenue, Mail Station 231
ATTN: Mr. Norbert Schnog   1
Norwalk, CT   06856

General Dynamics
Pomona Division
PO Box 2507
ATTN: Mr. F. Bannie Kuffer   1
Pomona, CA   91766

General Research Corporation
307 Wynn Dr.   1
ATTN: Dr. Karl Wormbrod
Huntsville, AL   35807

TRW Inc.
Defense and Space Systems Group
One Space Park   1
Redondo Beach, CA   90278

DRSMI-R   1
DRSMI-LP, Mr. Voigt   1
DRSMI-RPR   15
DRSMI-RPT   1
DRSMI-RH, Mr. Jennings   1
DRSMI-RHA   1
DRSMI-RHB   1
DRSMI-RHC   1
DRSMI-RHS, Dr. Roberts   1
DRSMI-RHS, Dr. Honeycutt   1
DRSMI-RHS, Dr. Jones   15
DRSMI-Q, Mr. Hutcheson   1
DRSMI-RL, Mr. Parham   1

US Army Materiel Systems Analysis Activity
ATTN: DRXSY-MP   1
Aberdeen Proving Ground, MD   21005